PONTIFICIA UNIVERSIDAD CATOLICA DE CHILE
ESCUELA DE INGENIERIA

PART II: SELF-CENTERING FRICTIONAL DAMPER

BENJAMÍN WESTENENK ORREGO

Thesis submitted to the Office of Research and Graduate Studies in partial fulfillment of the requirements for the Degree of Master of Science in Engineering

Advisor:
JUAN CARLOS DE LA LLERA MARTIN

Santiago de Chile, (December, 2011)

PONTIFICIA UNIVERSIDAD CATOLICA DE CHILE
ESCUELA DE INGENIERIA

PART II: SELF-CENTERING FRICTIONAL DAMPER

BENJAMÍN WESTENENK ORREGO

Members of the Committee:

JUAN CARLOS DE LA LLERA M.

MATÍAS HUBE G.

EDUARDO IZQUIERDO V.

LUCIANO CHIANG S.

Thesis submitted to the Office of Research and Graduate Studies in partial fulfillment of the requirements for the Degree of Master of Science in Engineering

Santiago de Chile, (December, 2011)

To my father Cornelio and mother Loreto. Thanks for the support through all these years. I love you both.

ACKNOWLEDGMENTS

This research has been supported by the Chilean *Fondo de Fomento al Desarrollo Científico y Tecnológico*, FONDEF, through Grant #D07I1006. Special thanks go to Eduardo Izquierdo, André Coté and Marcelo Münzenmayer, their helpful support is gratefully appreciated. I would like to thank professor Juan Carlos de la Llera for his constant support and guidance through all these years. Without his motivation and drive I would surely not be the same professional and person I am today.

TABLE OF CONTENTS

Page

LIST OF TABLES

Page

LIST OF FIGURES

Page

RESUMEN

Esta investigación propone y estudia un nuevo dispositivo de disipación de energía, el Amortiguador Friccional Auto-Centrante (SCFD por sus siglas en ingles). Este dispositivo está destinado para uso general en aplicaciones sísmicas y en particular para mejorar el rendimiento de los edificios altos y estructuras especiales sometidas a terremotos. Su característica auto-centrante y la posibilidad de obtener comportamientos de histéresis diferentes (similar al amortiguador EDR) lo hace un dispositivo de sumo interés para el diseño sísmico. Se propone un modelo matemático inicial para entender el comportamiento del SCFD y para caracterizar las variables importantes involucradas en el proceso de diseño. Por otra parte, se estudiaron diferentes configuraciones posibles del dispositivo que resultarían en el mismo comportamiento. La configuración final usada dependerá de la aplicación final y de la capacidad necesaria para cada SCFD específico. Por otro lado, se llevó a cabo una variación de las variables importantes para analizar sus efectos sobre el comportamiento histerético. Se calcularon las condiciones que deben cumplirse para obtener un comportamiento auto-centrante. Además, se realizaron pruebas de laboratorio para obtener coeficientes de fricción, rigideces de resortes de compresión y curvas tensión-deformación para probetas de goma. Estas pruebas se utilizaron para diseñar adecuadamente un prototipo preliminar del amortiguador. Finalmente, para probar las ecuaciones iniciales, un dispositivo a gran escala de 12tonf se diseñó, fabricó y probó en laboratorio. Los resultados teóricos y experimentales para el SCFD a real escala mostraron una concordancia excelente, lo cual confirmó el comportamiento simple y predecible del dispositivo.

Palabras Claves: Disipador friccional, Disipador auto-centrante, Dispositivos de disipación de energía, Respuesta sísmica, Edificios de gran altura.

ABSTRACT

This research proposes and studies a new energy dissipating device, the Self-Centering Frictional Damper (SCFD). This device is intended for general use in seismic applications and specifically to improve the performance of high-rise buildings and special structures subjected to earthquakes. Its self-centering characteristic and the wide range of possible hysteretic behaviors (similar to the EDR damper) makes it a device of great interest for seismic design. An initial mathematical model is proposed in order to understand the behavior of the SCFD and to characterize important variables involved in the design process. Moreover, different possible configurations of the damper which results in the same behavior were studied. The ultimately used configuration will depend in the final application and capacity required in each specific SCFD. On the other hand, a variation of important variables was performed to analyze their effects on the hysteretic behavior. The conditions that must be met to get a self-centering behavior were also computed. Furthermore, laboratory tests were performed to obtain friction coefficients, stiffness of compression springs and rubber stress-strain curves. These tests were used to appropriately design a preliminary SCFD prototype. Finally, to test the initial equations, a 12tonf large-scale damper was designed, manufactured and tested in laboratory. Theoretical and experimental results for the real-scale SCFD showed excellent agreement, which confirmed the simple predictable behavior of the device.

Keywords: Frictional damper, Self-centering damper, Energy dissipating devices, Seismic response, High-rise buildings.

1 INTRODUCTION

Earthquake engineering has been a major field of study around the world and especially for countries with risk of large earthquakes. The February 27 Maule earthquake in Chile (M_w=8.8) and the March 11 Miyagi earthquake in Japan (M_w=9.0) caused severe damage to infrastructure and lifelines, showing the devastating effect on society and emphasizing the importance of good practices in structural engineering. Technologies such as base isolation systems, energy dissipation devices and active control systems has proven to work and provide the structures the safety needed to successfully withstand an earthquake. In particular, energy dissipating devices are mechanical dampers which give the structures significant energy absorption characteristics under cyclic deformation. These dampers are normally connected between two points of a structure in order to transform the kinetic energy of the relative movement of the points into heat, dissipating energy and helping reduce the stresses in the structural elements. This research proposes a new and innovative energy dissipating device, the Self-Centering Frictional Damper (SCFD).

For structural applications different dampers have been used, such as: devices with viscous fluids, metallic systems and frictional dampers (Aiken, Nims, Whittaker & Kelly, 1993). Viscous devices dissipate energy by the circulation of the viscous fluid through a reduced section. Metallic dampers achieve energy dissipation by the plastic deformation of specially designed sections. Furthermore, frictional devices dissipate energy through the friction induced in the relative motion between surfaces.

The Sumitomo device, the Pall damper, the SBC connection system and the Energy Dissipating Restraint (EDR) (Aiken, 1996) are some of the existing frictional dampers. Excluding the EDR damper (Inaudi, Nims & Kelly, 1993; Nims, Richter & Bachmann,

1993) most frictional devices produce an elastoplastic hysteretic curve with residual deformation at the moment of unloading. Some advantages for using these devices are: (i) they have great energy dissipation capacities; (ii) their response is not affected by the amplitude, frequency or number of cycles of the input; (iii) the initial friction force can be controlled by loading the friction surfaces; (iv) are not affected by fatigue; (v) behave properly at different temperatures; (vi) are simple in theory and fabrication.

There is still a need for new, simple, and low-cost energy dissipating devices capable of taking heavy loads with a compact external shape and with no residual deformation. The SCFD intends to be an alternative energy dissipating device with the previously mentioned characteristics. The proposed damper is a mechanical device that uses friction surfaces and elastic elements to produce a self-centering behavior. Some advantages of this particular device are: (i) the equations that rules the behavior are very simple, (ii) is a low-cost device, (iii) has no residual deformation, (iv) can be modified in different configurations depending on the requirements, (v) can produce various hysteretic behaviors such as a flag-shaped or a triangular one.

The specific goals of this research are: (i) introduce and explain the SCFD and its possible variations; (ii) present the equations that rules the behavior of the device; (ii) provide a parameter variation for a successful preliminary design; (iii) accomplish reliable data based in experimental results for the friction coefficient and the behavior of rubber and compression springs; (iv) design, manufacture and test a large-scale SCFD.

To accomplish these goals, an initial mathematical model was proposed using simple equilibrium equations. In order to prove the theory, laboratory tests were done to individual internal elements of the device. Finally, a 12tonf SCFD was designed, manufactured and tested to prove the ultimate behavior of the device.

First of all, a description of the SCFD is presented followed by the assembly process and the possible configurations the device could have. Chapter 5 deals with the variation of important variables involved in the design and the conditions the device must comply in order to have a self-centering behavior. Chapters 6, 7 and 8 are devoted to experimental results in order to analyze friction coefficients, rubber behavior and stiffness of

compression springs. Chapter 9 presents the results for the 12tonf large-scale damper built. Finally, Chapter 10 refers to the main conclusions of this research and the suggested directions for further investigation. The information presented herein resulted in one article sent to an international journal (Westenenk & de la Llera, 2011).

2 THE SELF-CENTERING FRICTIONAL DAMPER

The Self-Centering Frictional Damper (SCFD) is an energy dissipating device based on friction surfaces, elastic elements and a particular geometry. Shown in Figure 2-1 are an external isometric view and a schematic cross section of the proposed device.

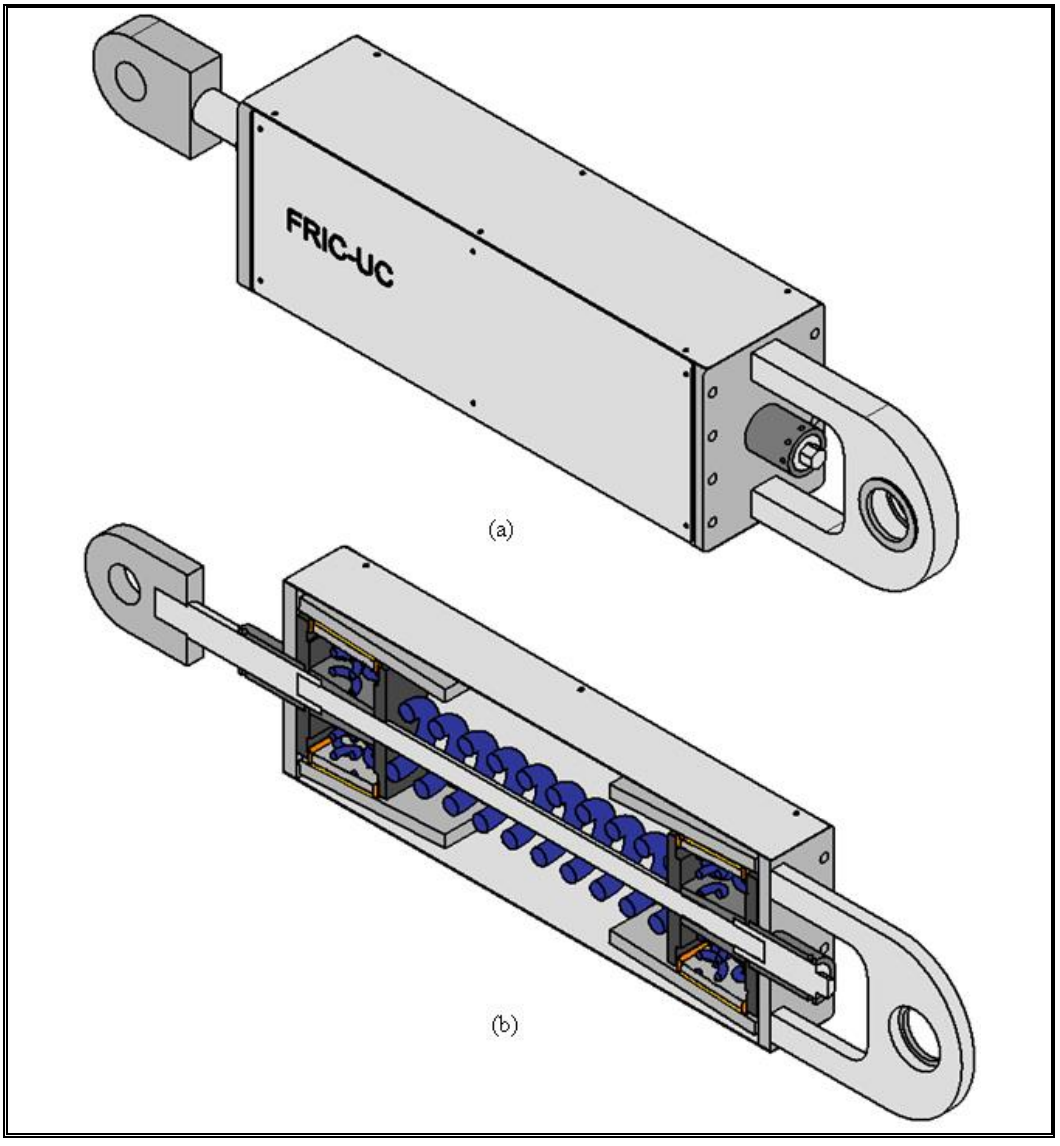

Figure 2-1: (a) External isometric view of the proposed device. (b) Schematic cross section

The device consists of a steel shaft, slanted steel walls, internal friction wedges, springs, pre-loading devices and end caps. The internal friction wedges consists in a sliding friction material, springs, a steel wedge, bronze stops and internal walls. Figure 2-2a shows a schematic cross section of the device and Figure 2-2b shows a schematic cross section of an internal friction wedge.

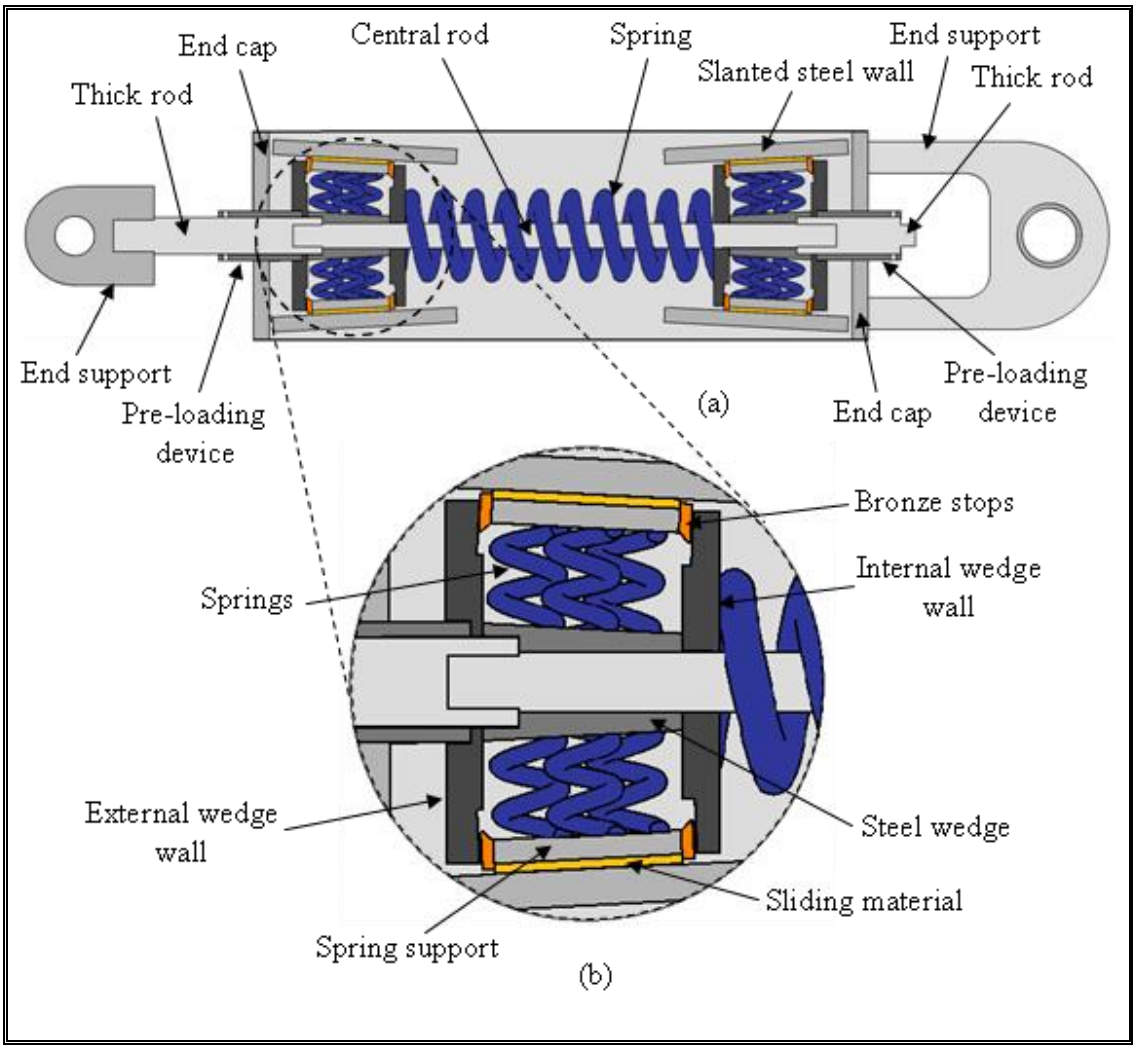

Figure 2-2: (a) Schematic cross section of the device. (b) Internal friction wedge

For a full understanding of the device, two three-dimensional pictures are shown in Figure 2-3.

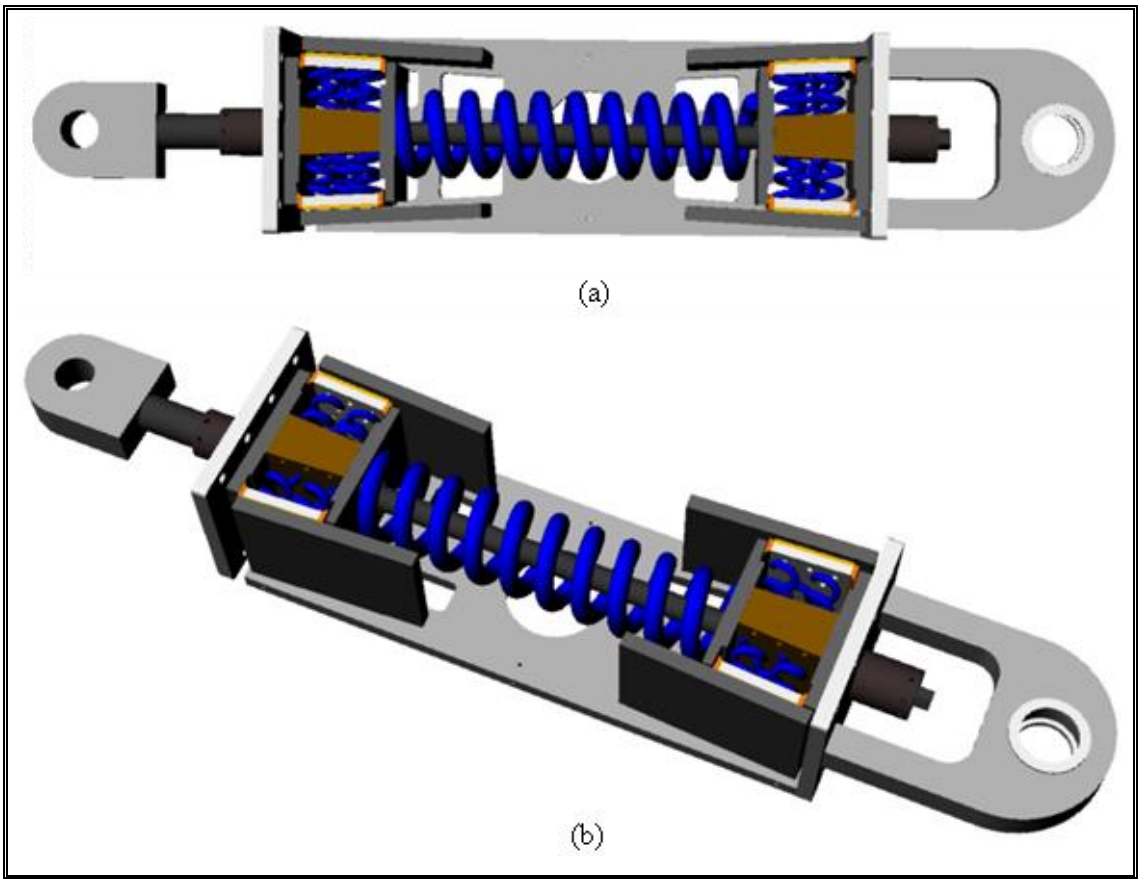

Figure 2-3: Three-dimensional pictures of the SCFD

The resistance of the device comes from the frictional forces between the sliding material and the slanted steel walls. These frictional forces depend on the friction coefficient and the normal force in the sliding material. The contact force between the friction surfaces increases linearly with the deformation of the device. Note that the big central spring, the angle of the inclined walls and the springs inside the internal friction wedges contributes to this normal force. The deformation of the device is defined as the relative motion of the central shaft with the external geometry. Note that the springs in this device can be replaced by any elastic element, such as: compression springs, rubber bearings or Belleville disc springs. From now on the central spring will be called longitudinal spring and the springs from the internal friction wedge will be called transverse springs.

This device can be pre-stressed in its undeformed configuration. Figure 2-4a shows the device at rest without any pre-deformation. The pre-loading device pushes the internal friction wedges to their pre-loaded configuration, shown in Figure 2-4b. As the device is loaded, the thick rod pushes the active internal friction wedge until it starts moving. The force necessary to move an internal friction wedge is defined by:

$$F_0 = K_R\Delta_0 + K_G\Delta_{0G}n_s\left(\sin(\alpha)+\mu\cos(\alpha)\right) \tag{2.1}$$

Where F_0 is the force necessary for the wedge to start moving, K_R is the stiffness of the longitudinal spring, Δ_0 is the pre-deformation of the longitudinal spring, K_G is the stiffness of the transversal springs, Δ_{0G} is the pre-deformation of the transversal springs, n_s is the number of sliding walls per wedge, α is the angle of the slanted steel walls and μ is the friction coefficient between the sliding material and steel. If $\beta_1 = n_s\left(\sin(\alpha)+\mu\cos(\alpha)\right)$, equation (2.1) can be written as:

$$F_0 = K_R\Delta_0 + K_G\Delta_{0G}\beta_1 \tag{2.2}$$

As the loading increases the internal friction wedge continues moving in the direction of the central shaft (Figure 2-4c). The force needed to move the device Δ is given by:

$$F_{load} = K_R\Delta_0 + K_G\Delta_{0G}\beta_1 + \left(K_R + \beta_1 K_G\sin(\alpha)\right)\Delta \tag{2.3}$$

Where F_{load} is the force necessary for the wedge to continue the movement and Δ is the deformation of the device. If the stiffness of the process of loading is defined as $K_l = K_R + \beta_1 K_G\sin(\alpha)$, equation (2.3) can be written as:

$$F_{load} = F_0 + K_l\Delta \tag{2.4}$$

At the moment of unloading, the forces of friction change direction and the force needed to have the device deformed Δ is given by:

$$F_{unload} = K_R\Delta_0 + K_G\Delta_{0G}\beta_2 + \left(K_R + \beta_2 K_G\sin(\alpha)\right)\Delta \tag{2.5}$$

Where F_{unload} is the force of the device at the moment of unloading, Δ is the deformation of the device and $\beta_2 = n_s(\sin(\alpha) - \mu\cos(\alpha))$. If the stiffness of the process of unloading is defined as $K_u = K_R + \beta_2 K_G \sin(\alpha)$, equation (2.5) can be written as:

$$F_{unload} = K_R\Delta_0 + K_G\Delta_{0G}\beta_2 + K_u\Delta \tag{2.6}$$

As the load changes its direction there is a loss of force given by:

$$\Delta F = F_{load} - F_{unload} = (\beta_1 - \beta_2)K_G(\Delta_{0G} + \Delta\sin(\alpha)) \tag{2.7}$$

Where ΔF is the loss of force due to unloading and Δ is the deformation of the device at the moment of unloading.

When the device returns to its pre-loaded configuration (internal friction wedges as Figure 2-4b) the force in the device is given by:

$$F_u = K_R\Delta_0 + K_G\Delta_{0G}\beta_2 \tag{2.8}$$

Where F_u is the force of the device at the moment when deformation is zero.

As the loading switches direction (Figure 2-4d) the same process occurs as described earlier. Note that if the angle, the stiffness, or the pre-load of the transverse springs are changed, a different behavior can be achieved for each direction.

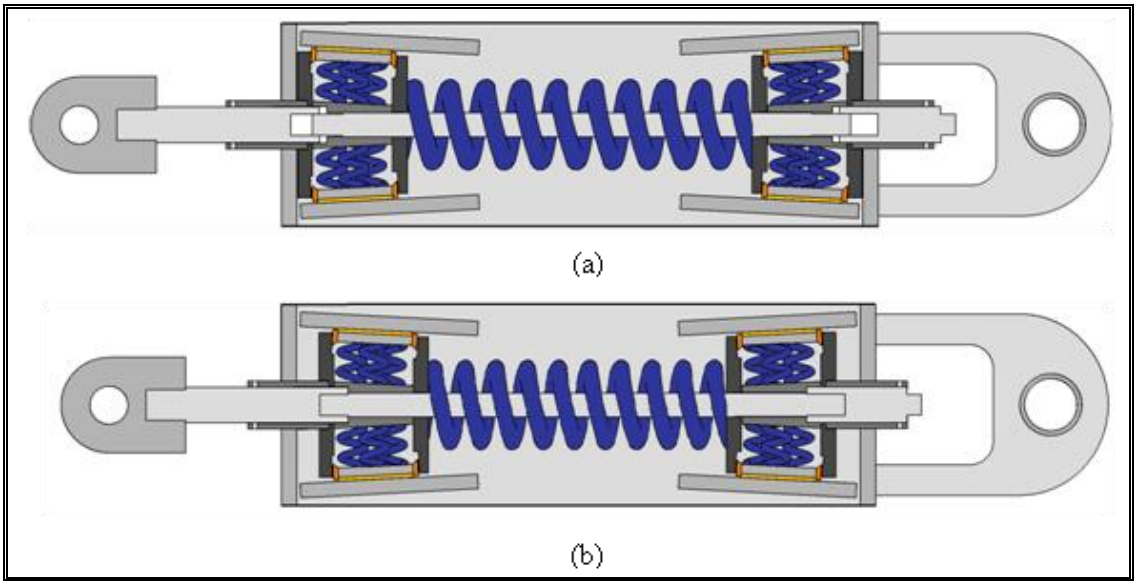

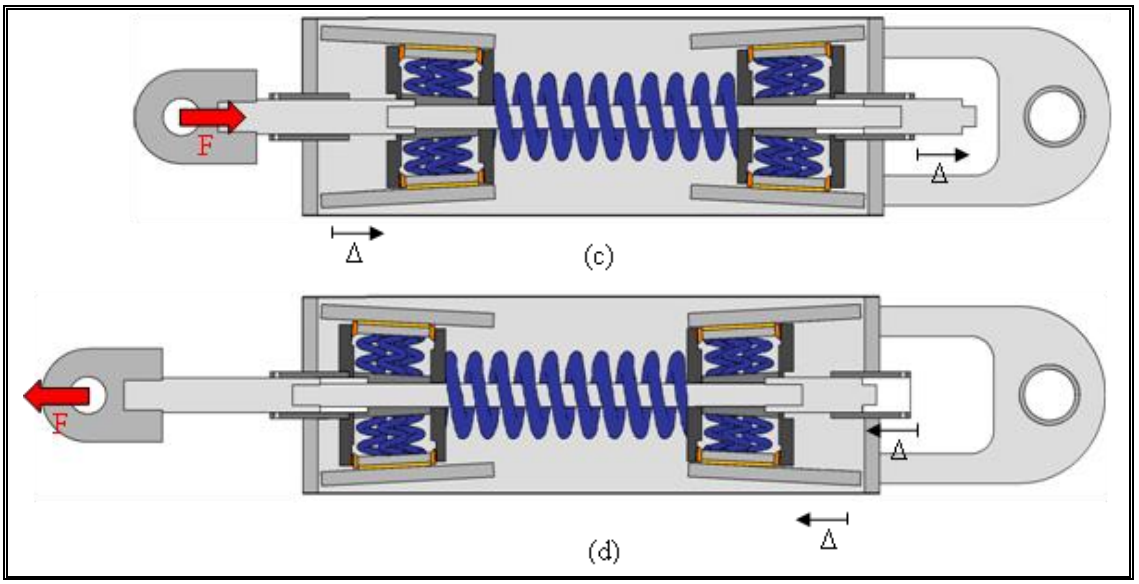

Figure 2-4: (a) Device without pre-load. (b) Pre-loaded configuration. (c) Device loaded in one direction. (d) Device loaded in the other direction

The performance of this device provides a very useful hysteretic behavior. Figure 2-5 shows the flag-shaped hysteretic loops achieved by the SCFD under cyclic loading. This hysteretic behavior has been studied previously (Inaudi et al, 1993; Christopoulos, 2004), since it has numerous advantages.

Note that other hysteretic behavior can be achieved varying the original parameters. If the pre-deformation of the transverse springs is zero the hysteretic loop is a triangular one with an offset at the origin (Figure 2-6). If the pre-deformation of the transverse springs is zero and the pre-deformation of the longitudinal spring is zero the hysteretic loop is a triangular one (Figure 2-7). The final hysteretic behavior is achieved by removing the central longitudinal spring and using an inclination of zero degrees in the slanted walls. Note that an additional mechanical device has to be added so that the wedges return to their undeformed position. The hysteretic behavior is the same as a Coulomb friction damper (Figure 2-8).

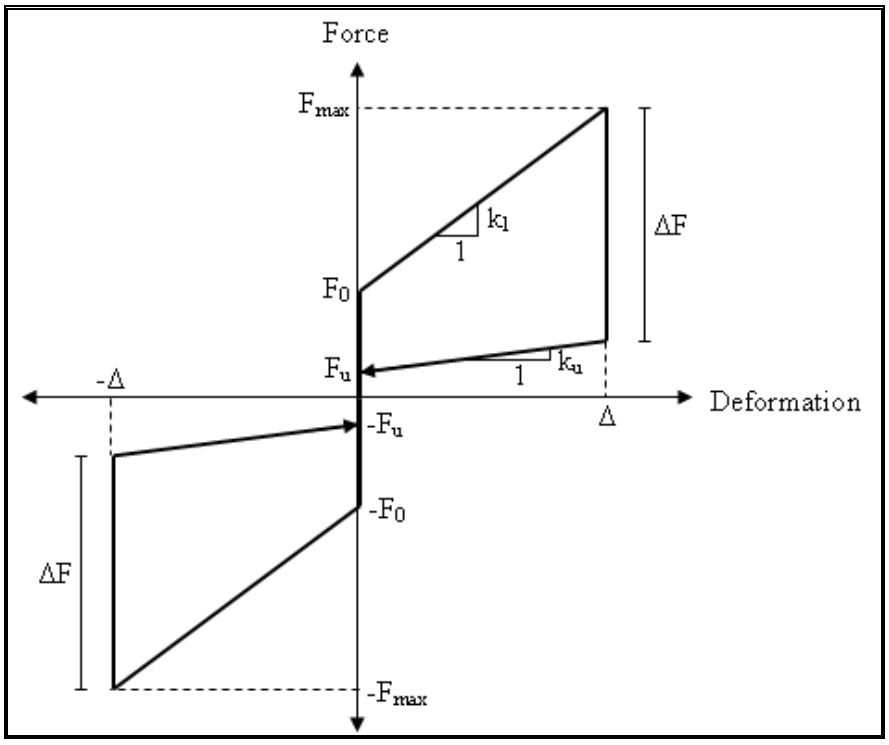

Figure 2-5: Flag-shaped hysteretic behavior of the SCFD

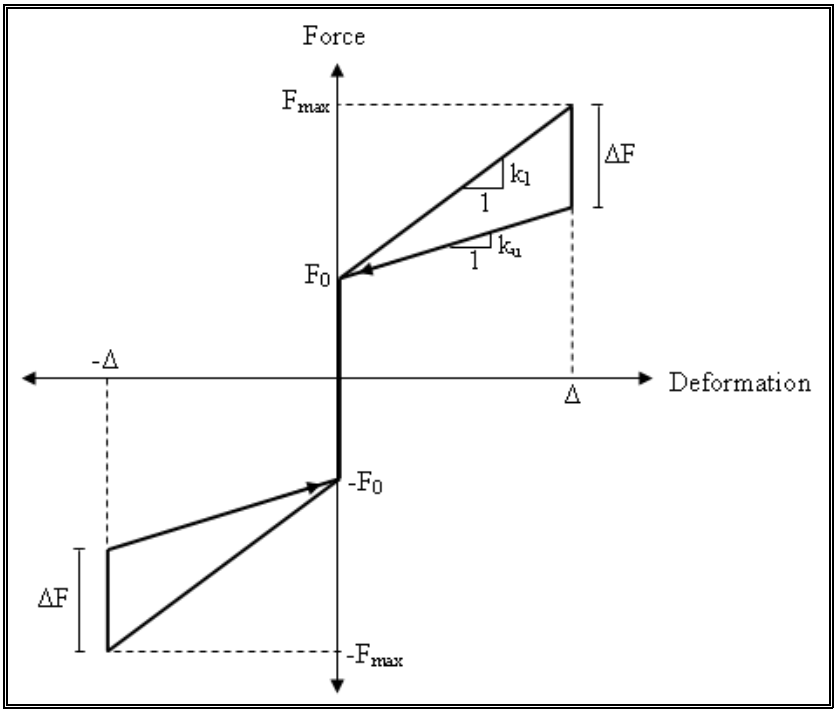

Figure 2-6: Triangular hysteretic behavior of the SCFD with an offset

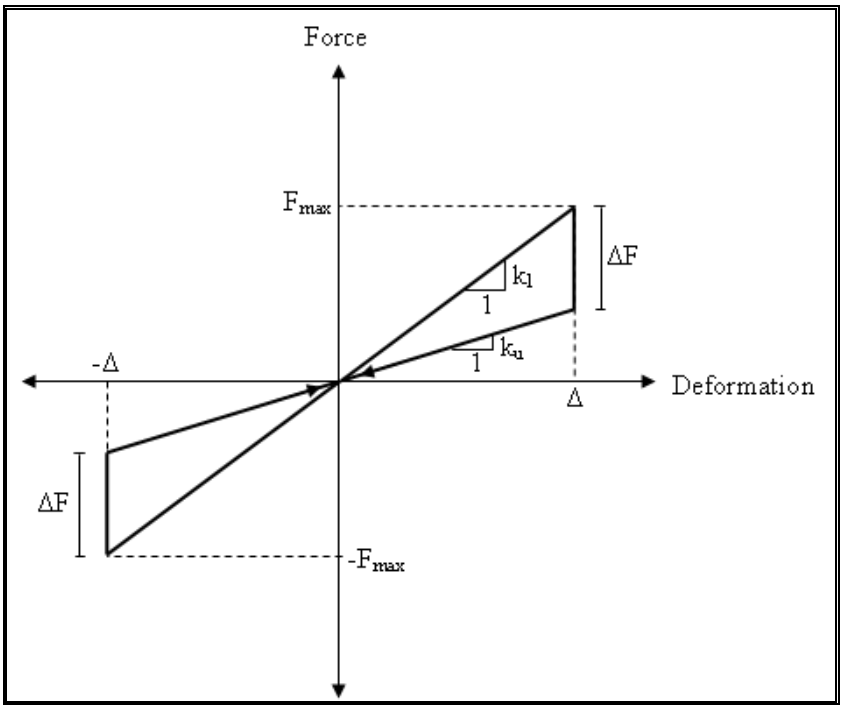

Figure 2-7: Triangular hysteretic behavior of the SCFD

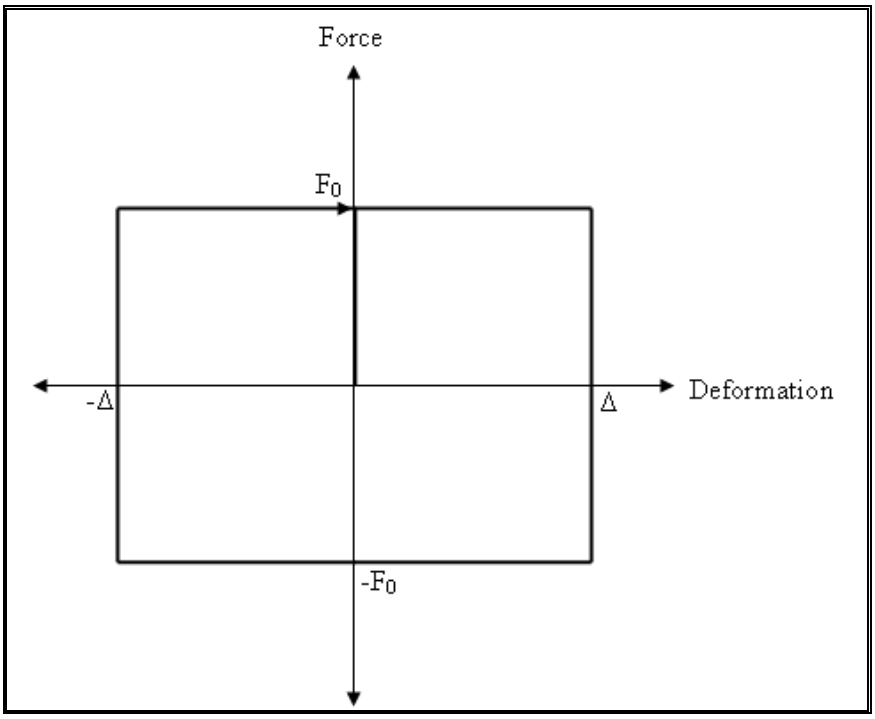

Figure 2-8: Square hysteretic behavior of the SCFD

The behavior of the SCFD is summarized in Figure 2-9 where four important points are defined in the hysteretic cycle. Table 2-1 summarizes these important points, showing the forces and deformations achieved in every instant.

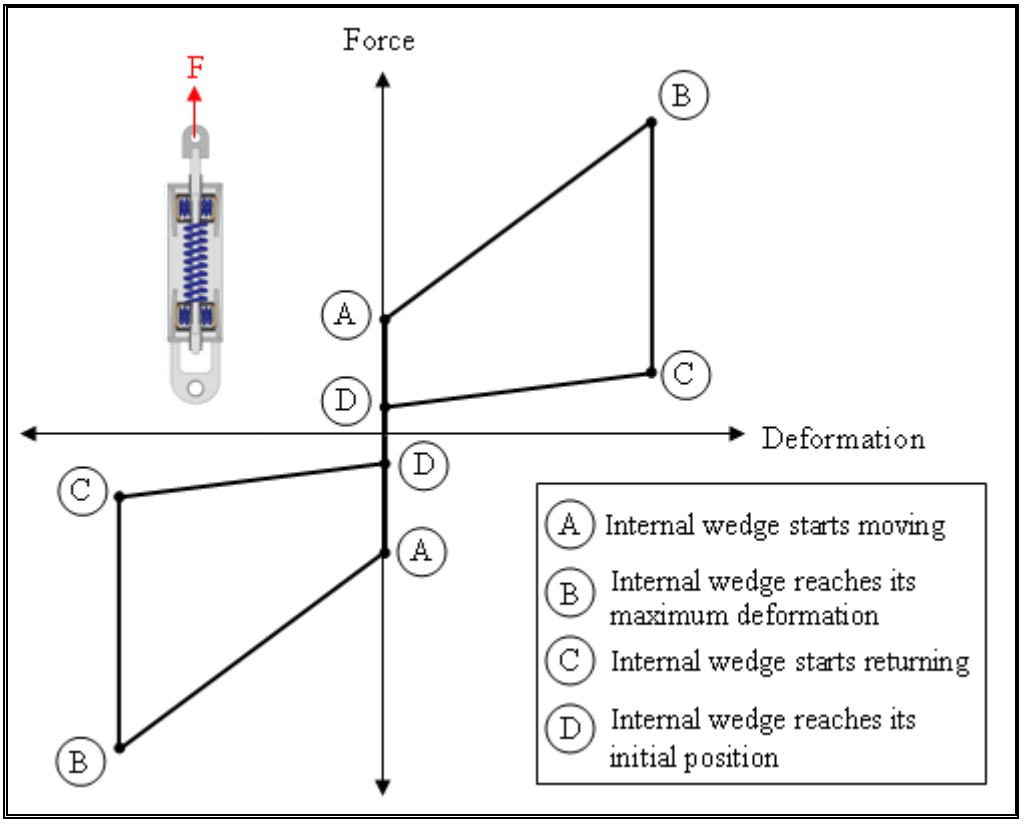

Figure 2-9: Hysteretic behavior of the SCFD

Table 2-1: Summary of important points in the hysteretic behavior

Point	Force	Deformation
A	$K_R\Delta_0 + K_G\Delta_{0G}\beta_1$	0
B	$K_R\Delta_0 + K_G\Delta_{0G}\beta_1 + (K_R + \beta_1 K_G \sin(\alpha))\Delta$	Δ
C	$K_R\Delta_0 + K_G\Delta_{0G}\beta_2 + (K_R + \beta_2 K_G \sin(\alpha))\Delta$	Δ
D	$K_R\Delta_0 + K_G\Delta_{0G}\beta_2$	0

3 DEVICE ASSEMBLY

To fully understand the SCFD, a complete step by step assembly of the different pieces is explained in order to achieve the final device. Photographs of the actual produced parts are also added.

Shown in Figure 3-1 is the central body of the device, which consists in two external walls and four slanted steel walls. This provides the backbone of the SCFD, where all the other pieces will be inserted. Note that holes were made in the two exterior walls so that the full operation of the device can be seen from the outside.

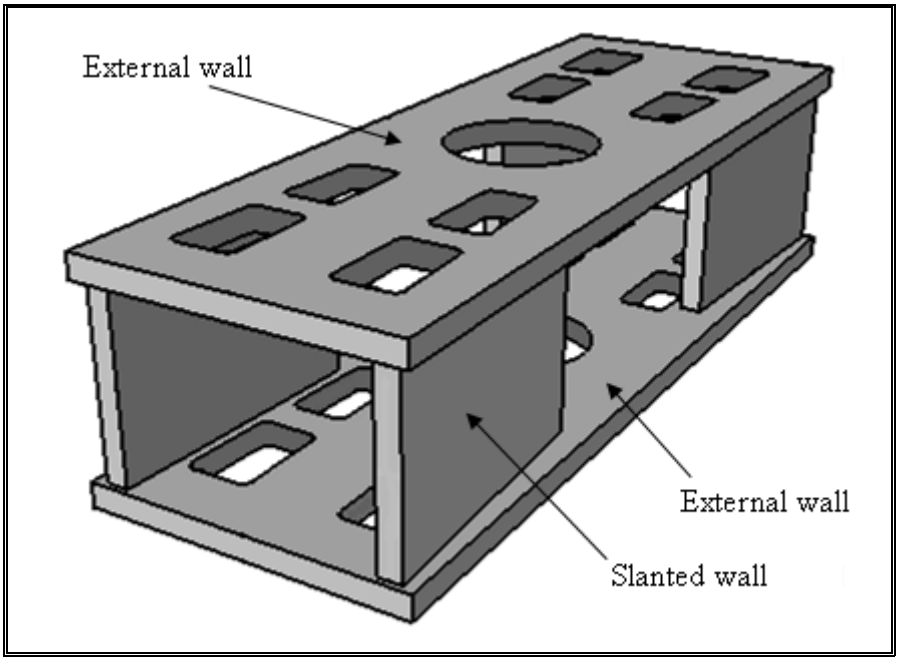

Figure 3-1: Central body of the SCFD

On the other hand, the internal friction wedges are the ones which provide the resistance of the SCFD. It consists of one steel wedge, the transverse springs, two supports, four bronze stops, the sliding material and an inner and outer wall. Figure 3-2 shows a schematic assembly of one internal friction wedge. Note that the bronze stops are bolted to the spring supports so that there is only axial deformation in the transverse springs.

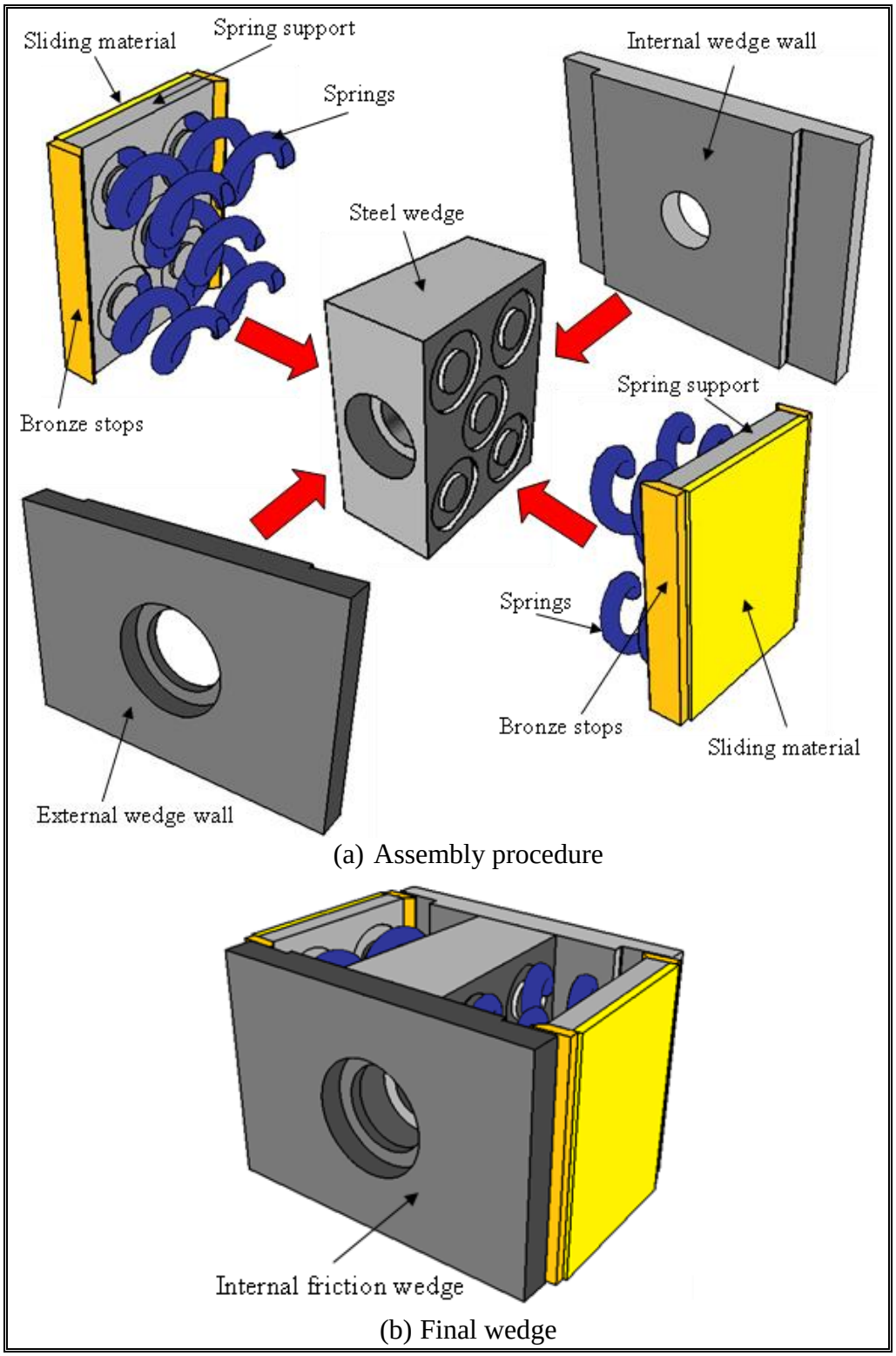

Figure 3-2: Schematic assembly of one internal friction wedge

Shown in Figure 3-3 are actual photos of the assembly process for an internal friction wedge.

Figure 3-3: Assembly of one internal friction wedge

The next step consists in inserting the friction wedges in the central body of the device. At one end of the central body an internal friction wedge is inserted while at the other end the longitudinal spring is inserted followed by the remaining friction wedge. This step of the assembly process is shown in Figure 3-4.

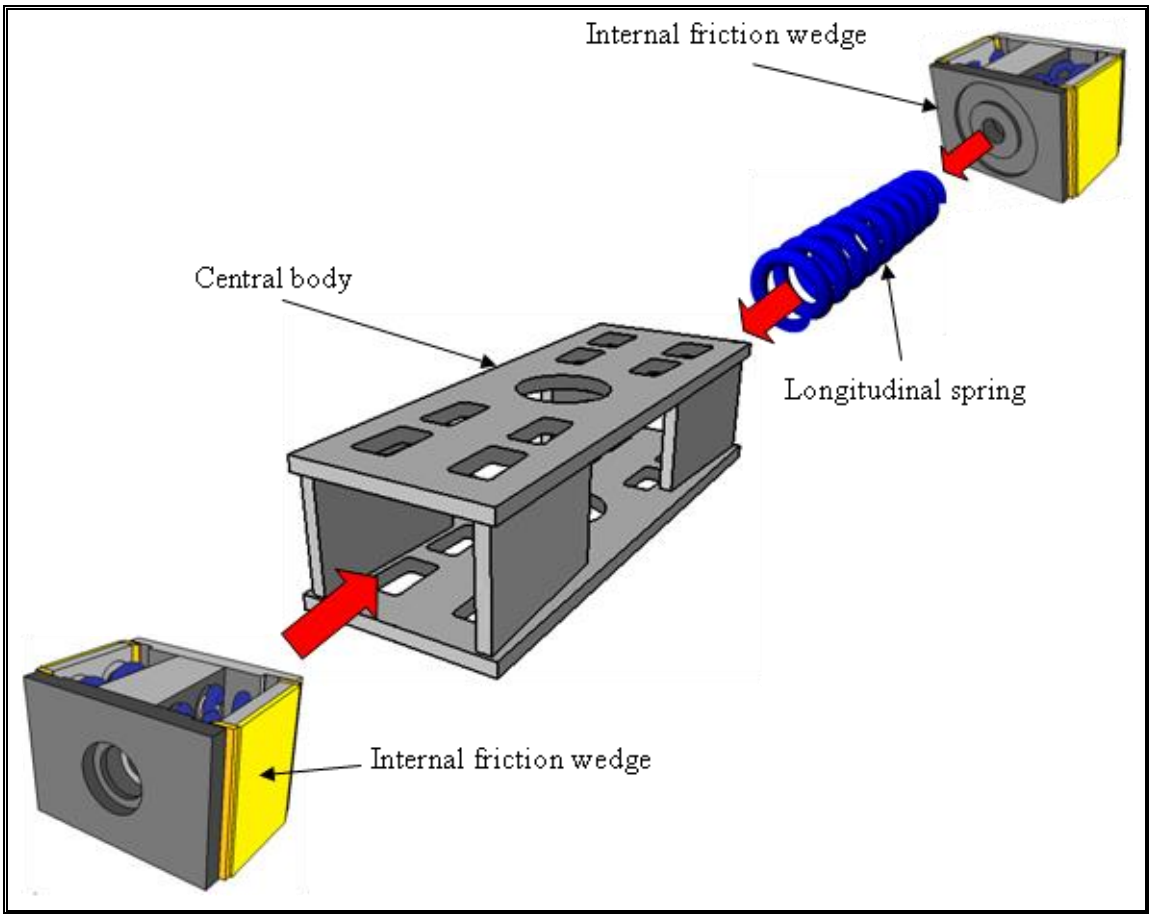

Figure 3-4: Assembly of central body, longitudinal spring and internal friction wedges

Once that step is completed, the end caps are inserted in both ends of the device. Note that an end support is welded to one of the end caps. The pre-load devices consist in two steel cylinders which are threaded inside both end caps following the previous step. Figure 3-5 shows the assembly of the end caps, an end support and both pre-loading devices. Shown in Figure 3-6 are actual photos of the two previous mentioned steps.

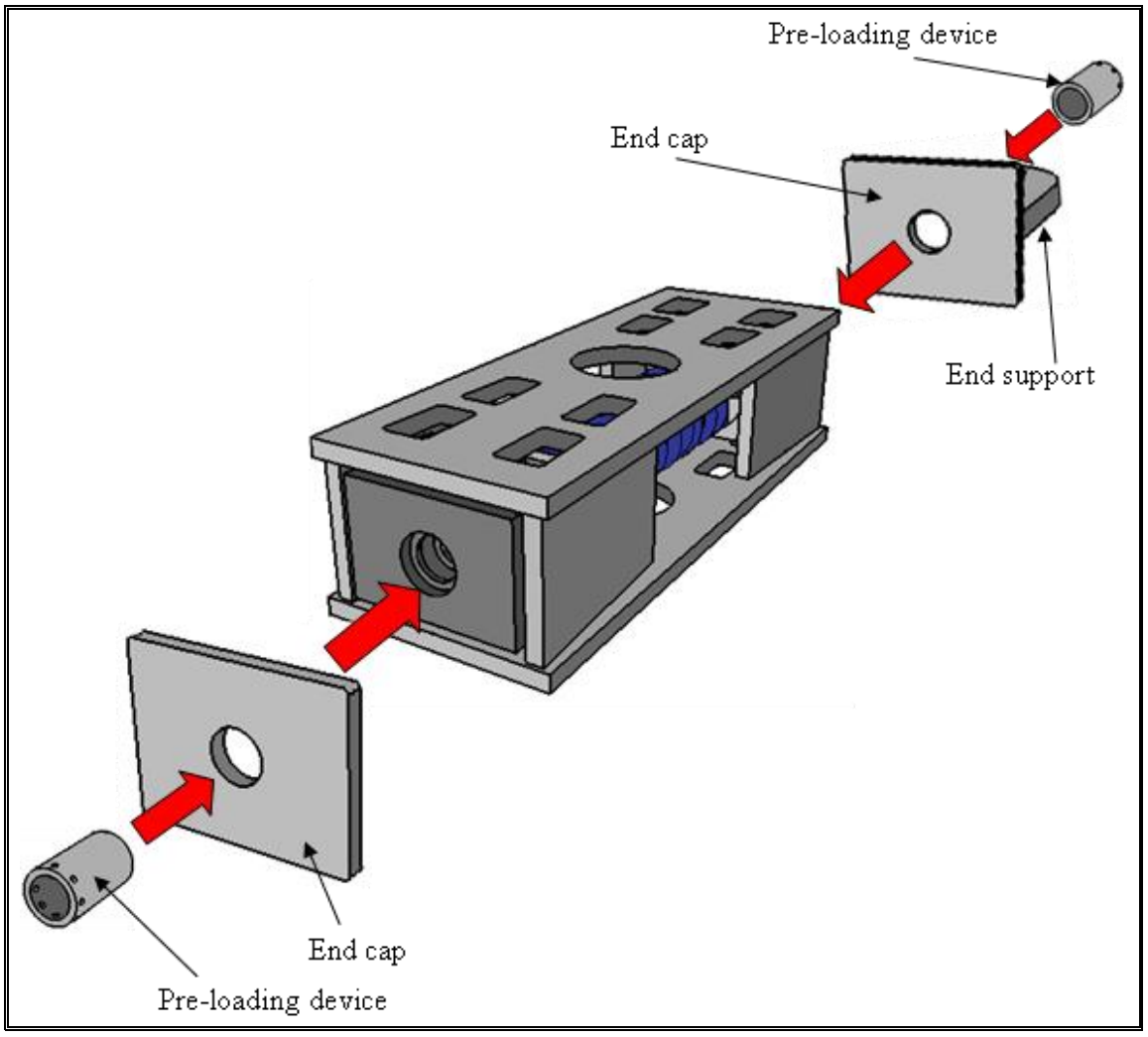

Figure 3-5: Assembly of end caps, an end support and both pre-loading devices

(a) (b)

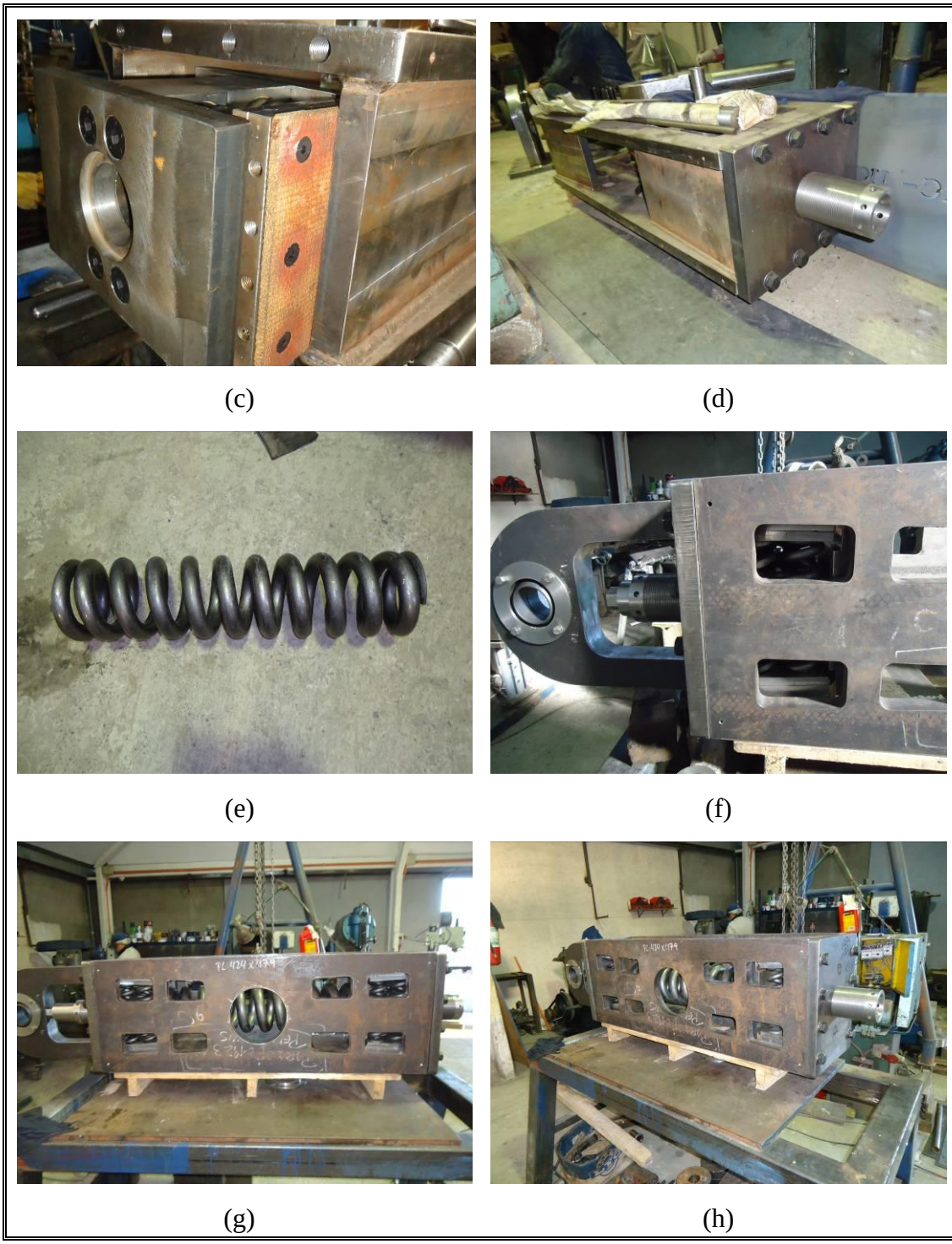

(c) (d)

(e) (f)

(g) (h)

Figure 3-6: Assembly of the SCFD

The last step to allow the operation of the device is to assemble the central shaft. The central rod, the thick rod and the remaining end support is inserted at one end while the second thick rod is assembled through the other end. Note that the central rod, both of the thick rods and the end support are threaded together. Figure 3-7 shows this schematic assembly.

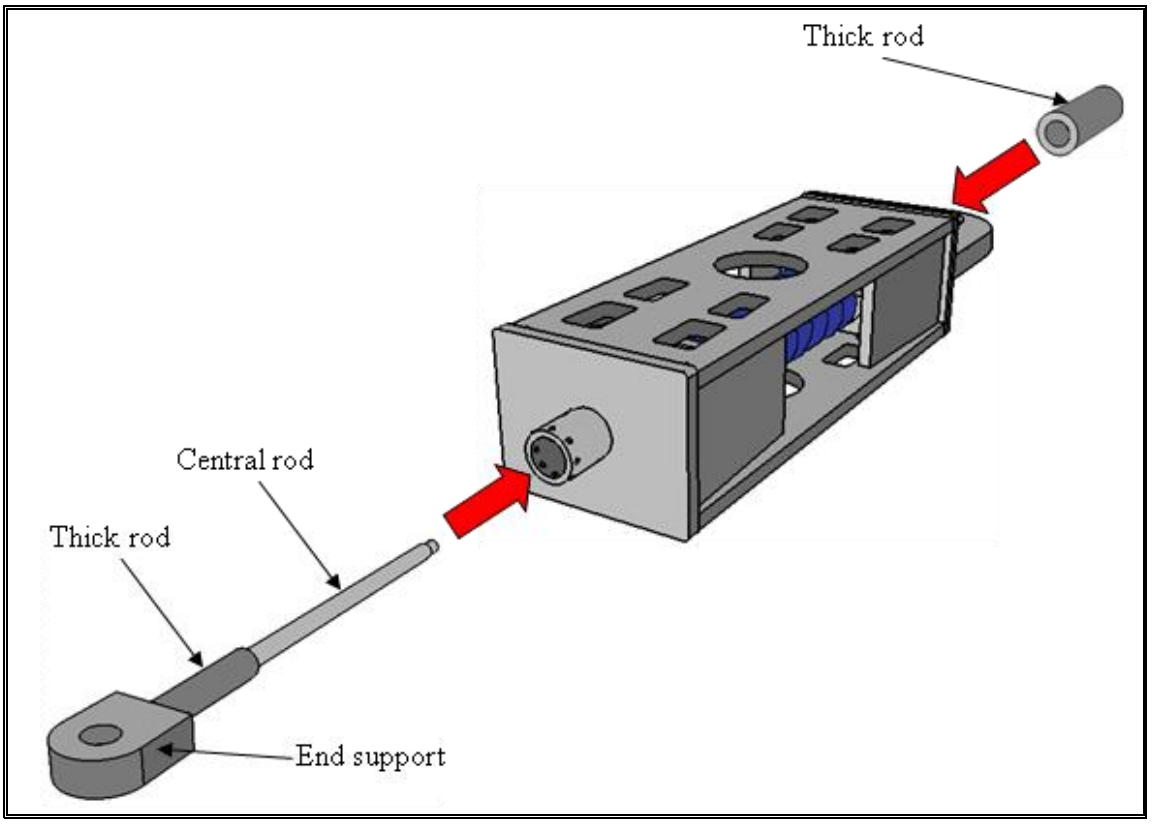

Figure 3-7: Assembly of the central rod, the thick rods and the remaining end support

To isolate the device from the exterior four covers are attached in each wall. Figure 3-8a shows this assembly and Figure 3-8b shows the final device assembled. In order to deliver a commercially interesting device, the exterior can be painted and modified. Figure 3-9 shows the final SCFD painted, finished and ready to operate.

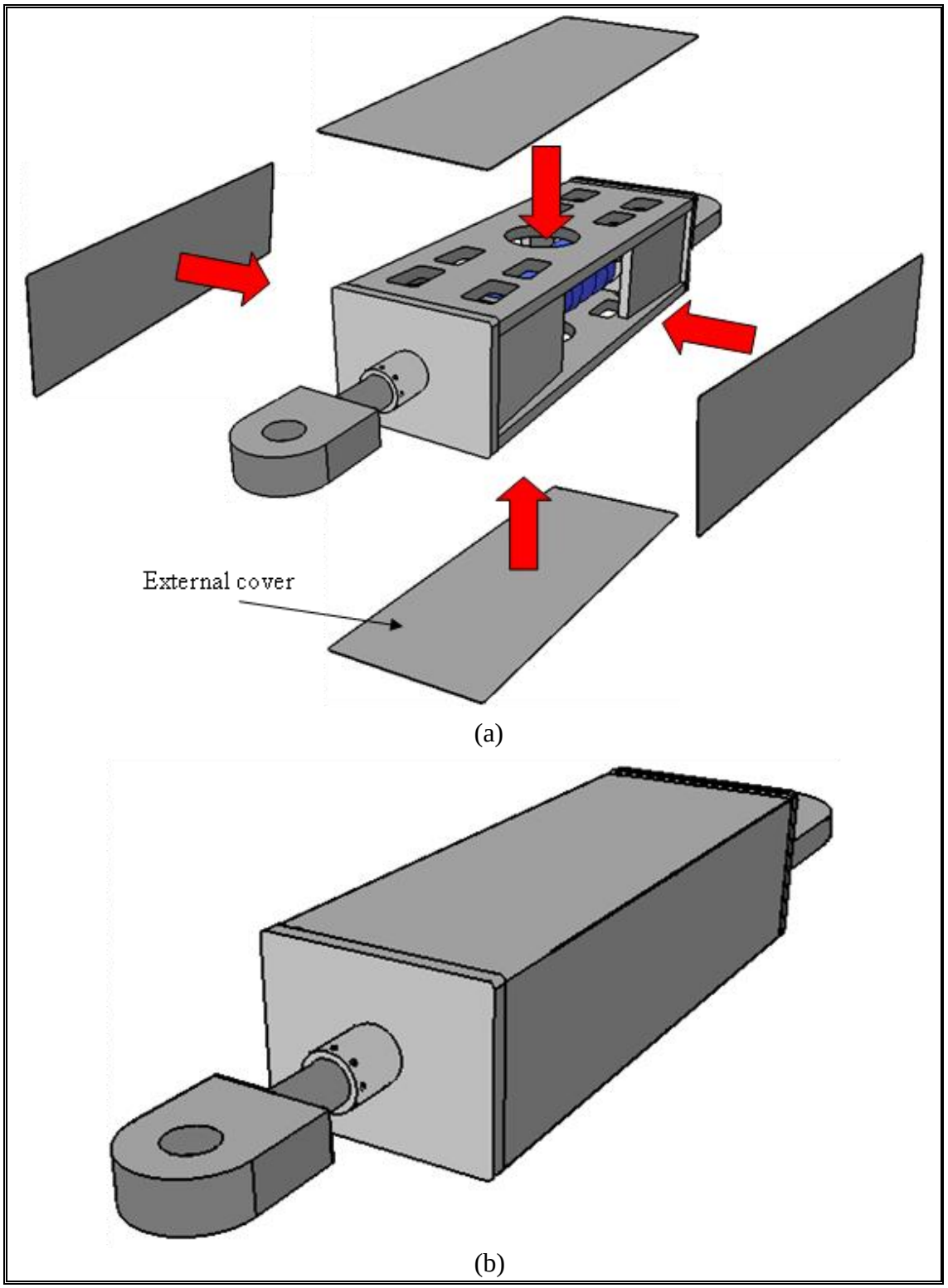

Figure 3-8: (a) Schematic assembly of the external covers. (b) Final device assembled

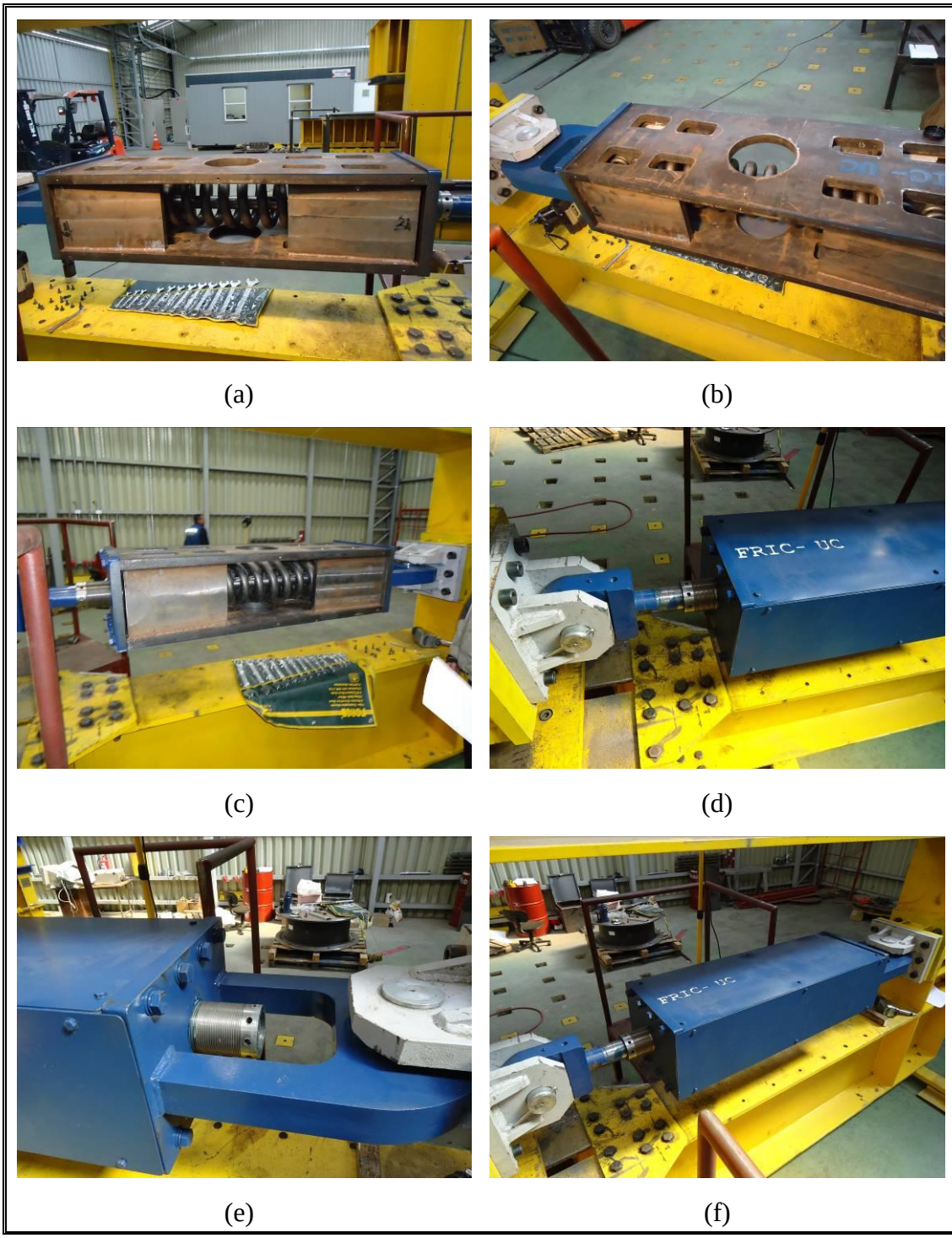

Figure 3-9: Final device ready to operate

4 POSSIBLE CONFIGURATIONS

There are several ways to get the same behavior with different configurations of the SCFD. Figure 4-1 shows a different setup of the device which would result in the same behavior mentioned in chapter 2 of this research. The proposed configuration consists mainly in using two different longitudinal springs and changing the direction of the slope in the slanted walls.

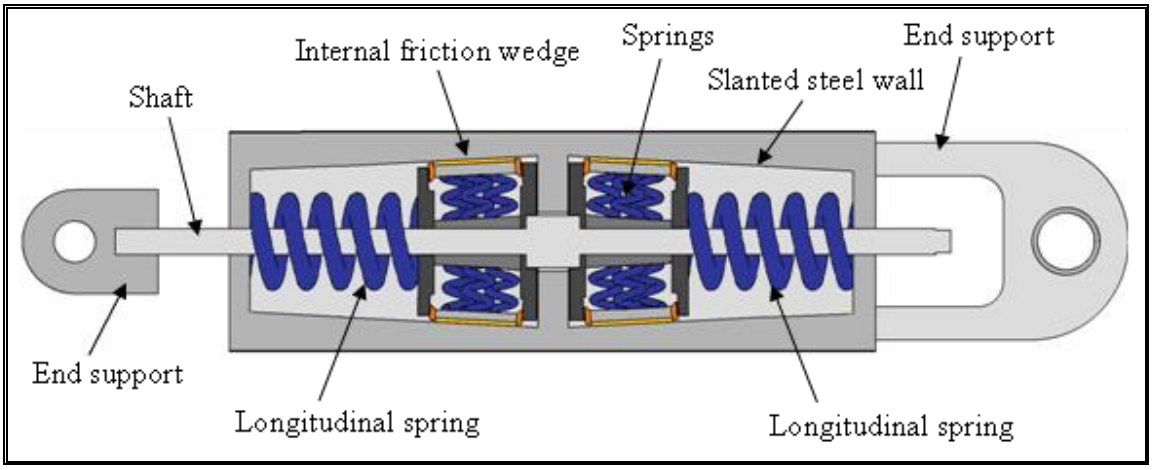

Figure 4-1: Possible configuration number 2

Note that this configuration provides the possibility of designing the device with two longitudinal springs with different stiffness. This would account in a dissimilar behavior in compression and in tension.

Figure 4-2 shows another possible configuration. This setup consists in rearranging the geometry of the device and in using the outer steel walls as the transverse springs. The internal friction wedges has been removed and the external geometry of the device acts as the proposed wedge. Note that in this figure the longitudinal spring is made of a rubber bearing. As in every proposed configuration, both springs (longitudinal and transverse springs) can be replaced by any elastic element. Compression springs are

suggested for normal behavior, rubber bearings when there is tension behavior and Belleville disc springs when big stiffness are required.

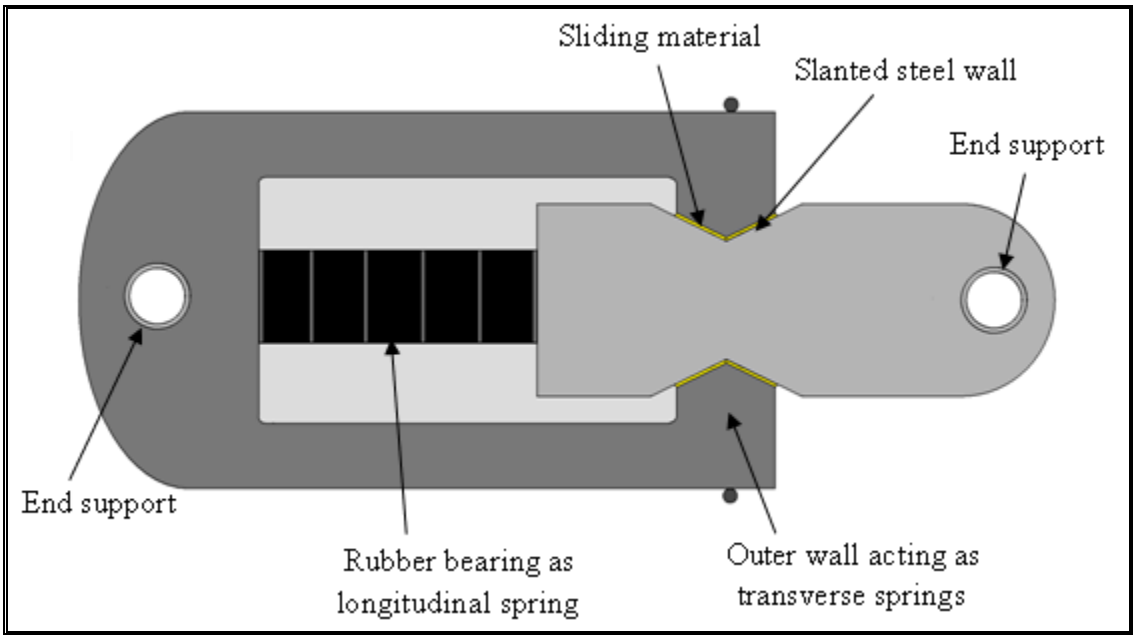

Figure 4-2: Possible configuration number 3

Figure 4-3 shows a similar configuration than the one shown in Figure 4-2. Instead of having the outer walls as transverse springs, the inner walls acts as these elastic elements. Note that there is also more space for inserting a bigger longitudinal spring in this configuration.

In the two previous configurations shown there is also the possibility of having the inner and outer walls fixed and placing transverse compression springs between the slanted steel walls and the sliding material, making the device similar to the original setup.

Note than in every proposed configuration the external shape of the device and the number of slanted walls per friction wedge, n_s, are variable and depends on the designer. The possibilities are endless, and just as an example Figure 4-4 shows a schematic SCFD with 4 slanted steel walls per wedge and with a cylindrical external geometry. Figure 4-4a shows an external isometric view while Figures 4-4b and 4-4c shows two schematic cross sections of the device.

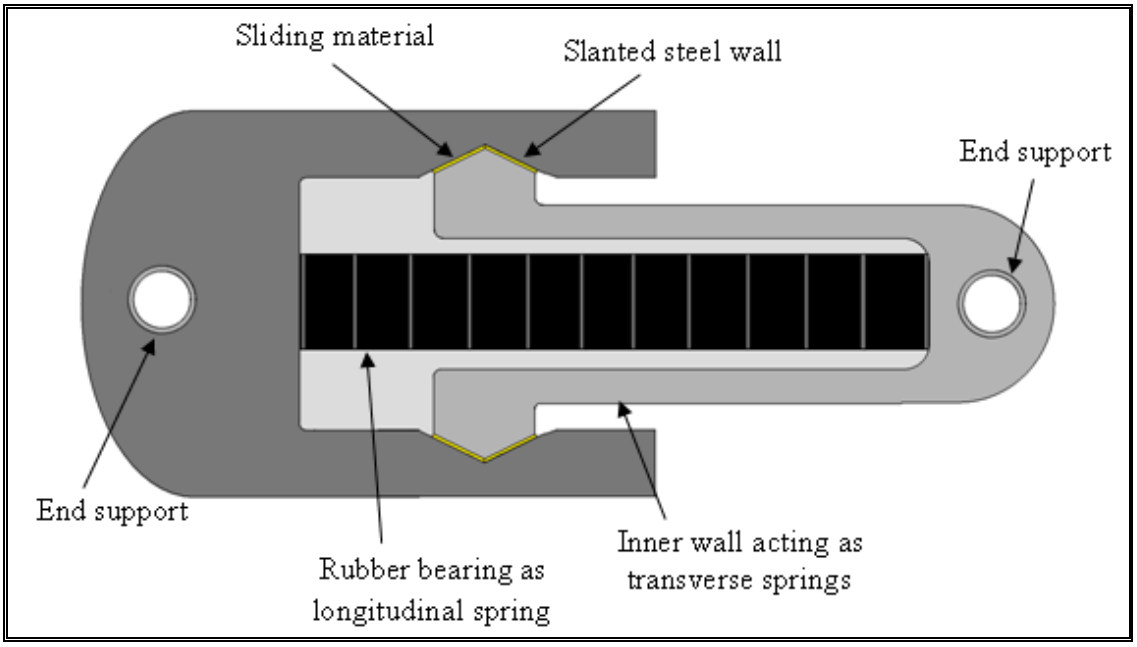

Figure 4-3: Possible configuration number 4

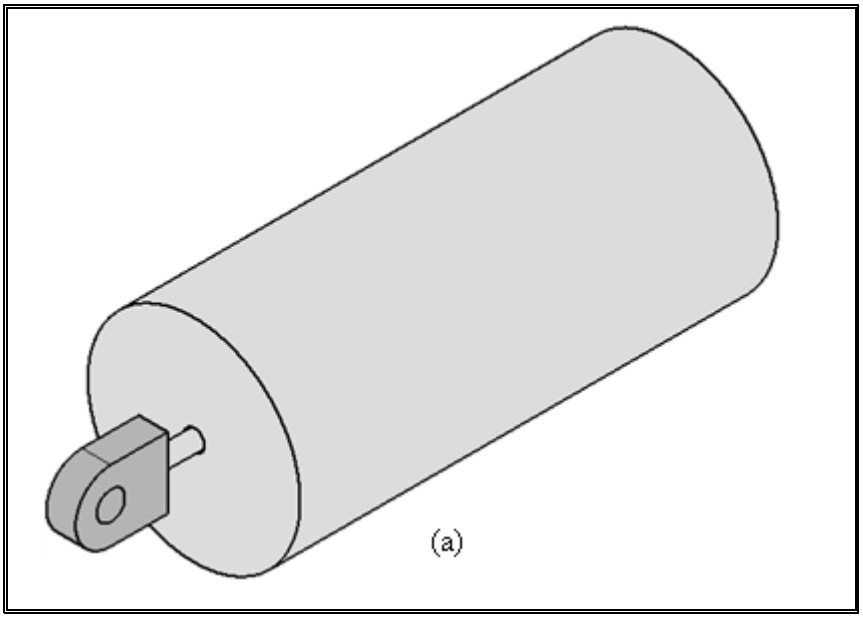

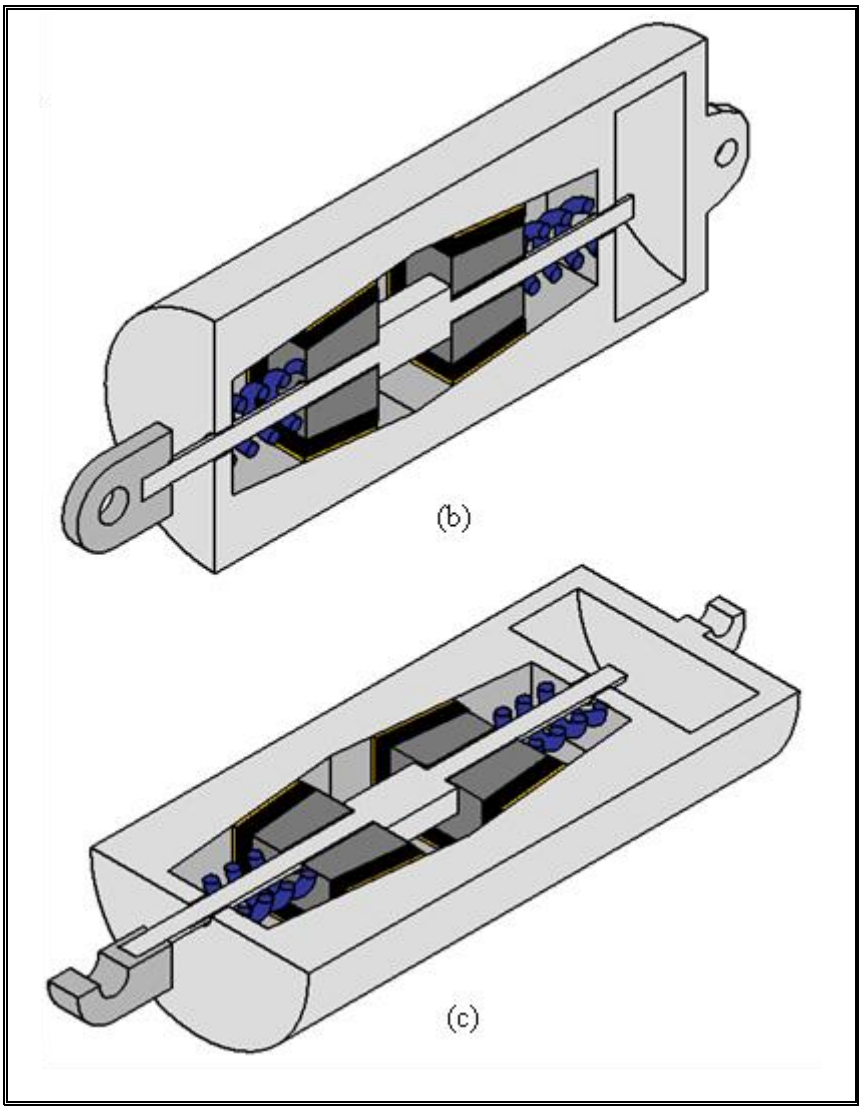

Figure 4-4: Example of a different configuration in the device

5 VARIATION OF PARAMETERS

The previous sections try to characterize the geometry and the behavior of the device. This section instead provides information on the variation of the parameters involved in the SCFD.

5.1 Hysteretic Behavior

It is interesting to analyze how the force-deformation curves will change if any of the original parameters of the device are modified. Starting with an original configuration, each of these parameters will be changed keeping the others constant, in order to visualize the importance of every one of them in the hysteretic behavior.

Figure 5-1 shows the variation of the angle of the slanted walls of the device (α) and its impact on the force-deformation curve.

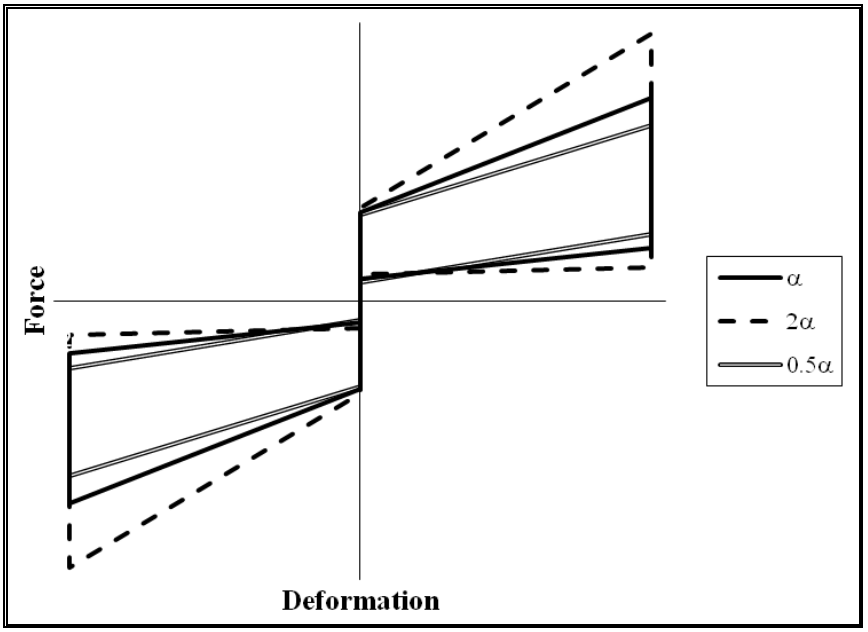

Figure 5-1: Hysteretic behavior changing the value of α

As the angle α rises, the stiffness of the loading process (K_l) increases significantly, resulting in a device with higher capacity. Note that the force when the deformation of the device is zero (F_0 and F_u) are practically unchanged by a variation of α. As in the design process is easy to change the value of α, this parameter becomes very important in the capacity of the final device.

Figure 5-2 shows the variation of the friction coefficient (μ) and its impact on the hysteretic behavior.

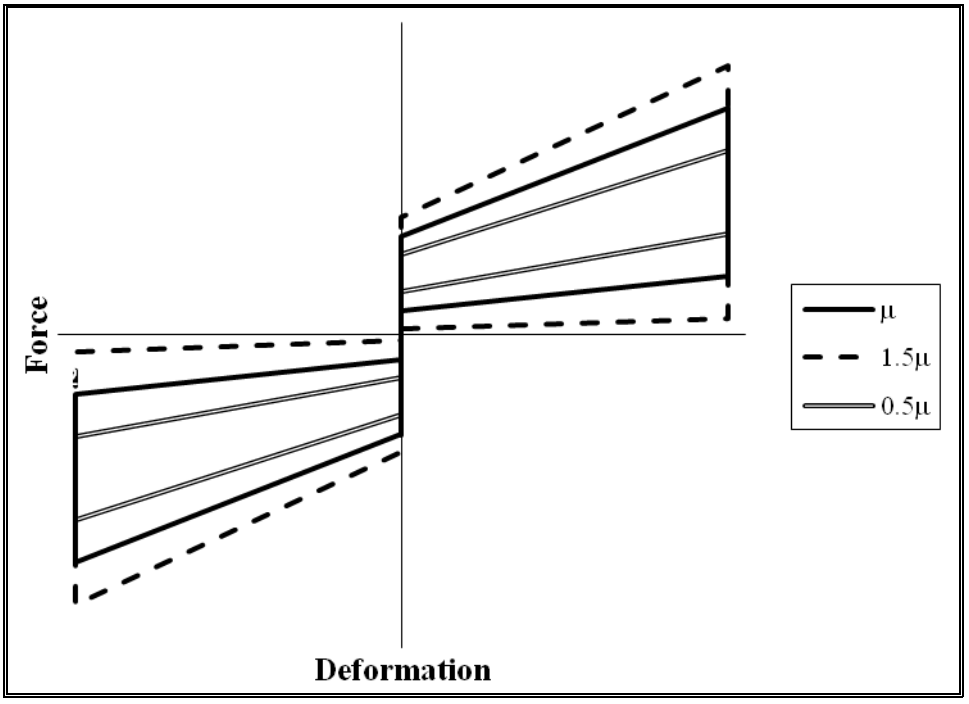

Figure 5-2: Hysteretic behavior changing the value of μ

As expected, the behavior of the device is strongly dependant of the friction coefficient used. As μ decreases, the hysteretic curve becomes more and more slender, dissipating significant less energy. Small changes in the friction coefficient would result in a totally different behavior of the device, hence the importance of this parameter in the design process.

Figure 5-3a shows the variation of the stiffness of the longitudinal spring (K_R) while Figure 5-3b shows the variation of the stiffness of the transverse springs (K_G) and their impact on the behavior of the SCFD.

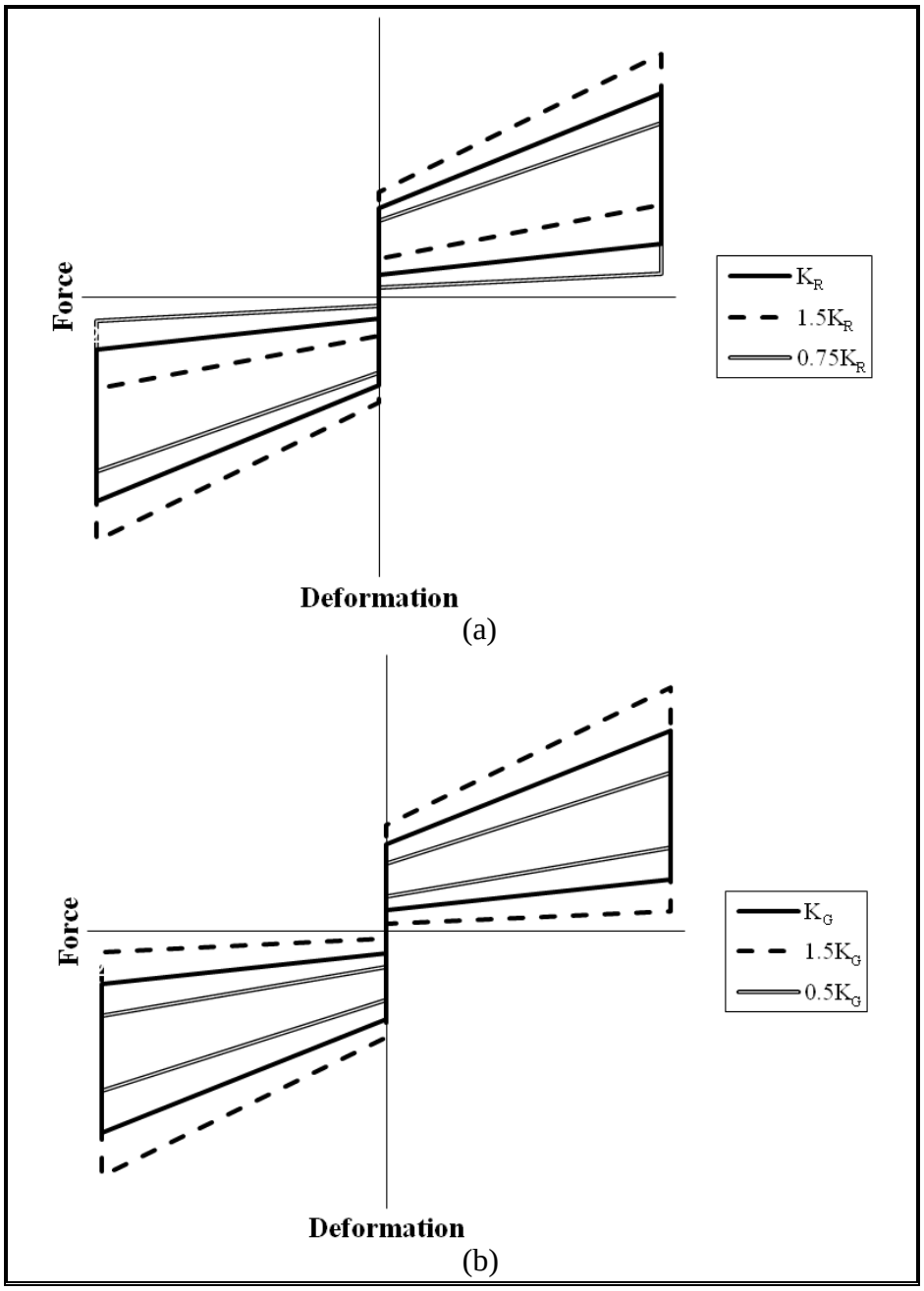

Figure 5-3: (a) Hysteretic behavior changing the value of K_R, (b) hysteretic behavior changing the value of K_G

As the stiffness of the longitudinal spring increases, the stiffness of the loading and unloading process (K_l and K_u) slightly increases. Note that the effect of varying K_R results in changing the position of the "flag behavior". Increasing K_R would imply a much higher "flag" than with lower K_R values. On the other hand, varying K_G would result in a similar behavior than varying the friction coefficient μ. As K_G decreases, the force-deformation curve becomes more and more slender. Since this parameter can be chosen and has less variation than the friction coefficient, K_G is not a variable as important as μ in the design process.

Figure 5-4a shows the variation of the pre-deformation of the longitudinal spring (Δ_0) while Figure 5-4b shows the variation of the pre-deformation of the transverse springs (Δ_{0G}) and their impact on the force-deformation curve.

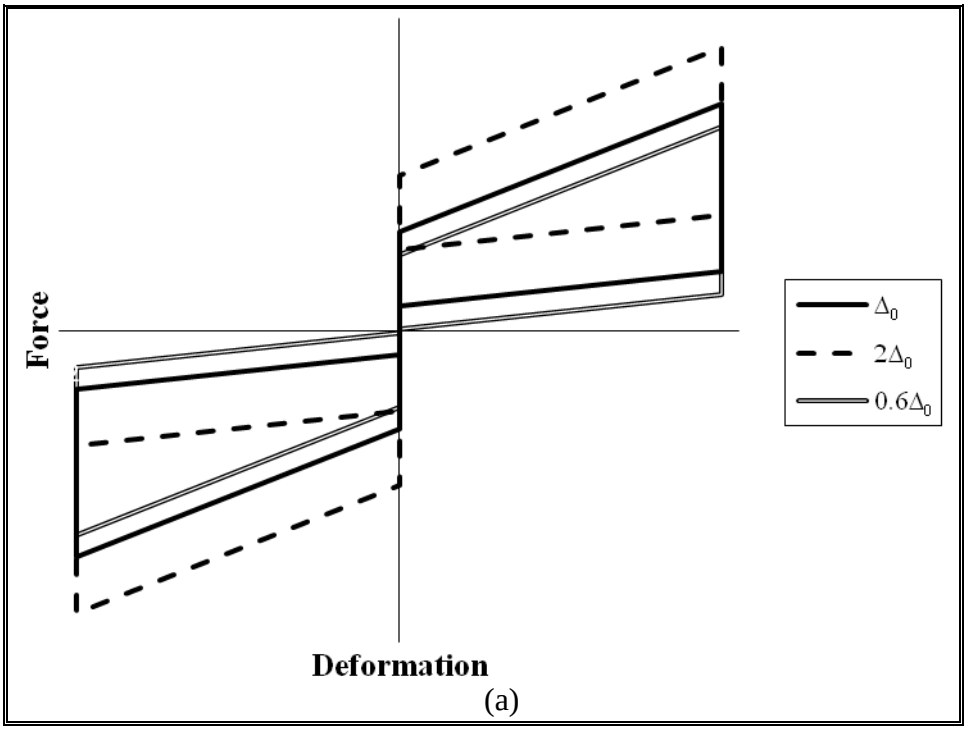

(a)

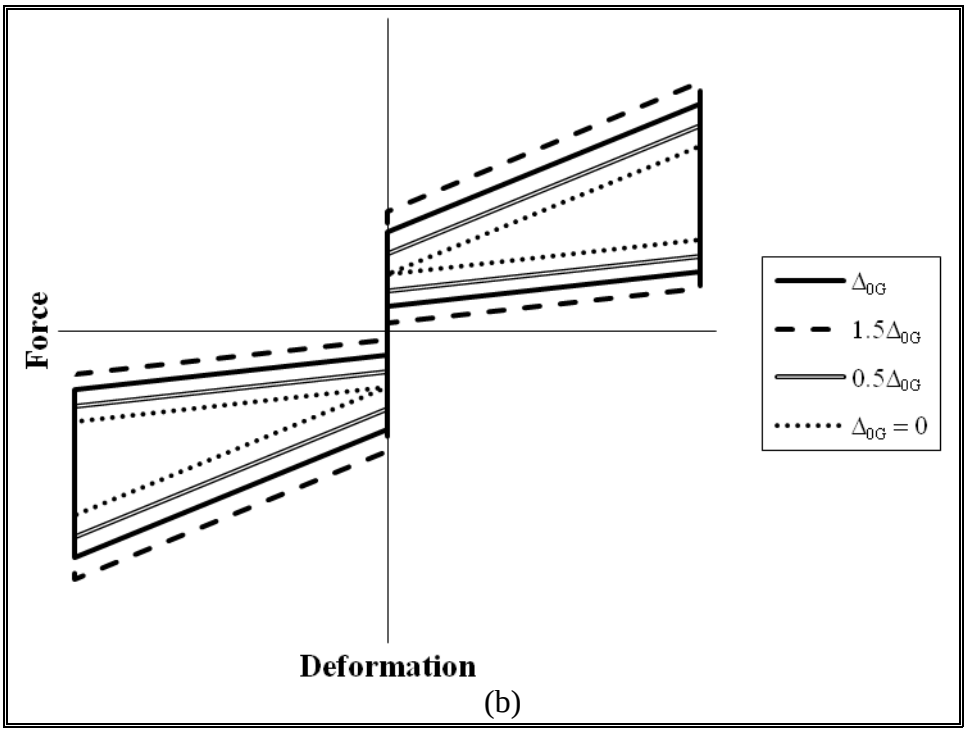

(b)

Figure 5-4: (a) Hysteretic behavior changing the value of Δ_0, (b) hysteretic behavior changing the value of Δ_{0G}

Varying Δ_0 would result in changing the position of the flag. Increasing its value would imply a much higher flag. Note that this parameter does not change the energy dissipated per cycle, as the area between the curves remains constant. On the other hand, when the pre-deformation of the transverse springs Δ_{0G} decreases, the loading curve and the unloading curve approach each other. This happens until Δ_{0G} is zero, where the flag-shaped behavior changes to a triangular one.

Finally, Figure 5-5 shows the variation of the number of sliding walls per friction wedge (n_s) and its impact on the hysteretic behavior. When n_s decrease, the hysteretic behavior becomes more and more slender. This parameter depends on the final internal shape chosen for the device. Usual values for n_s are 2 and 4, using the latter value for devices with higher capacities.

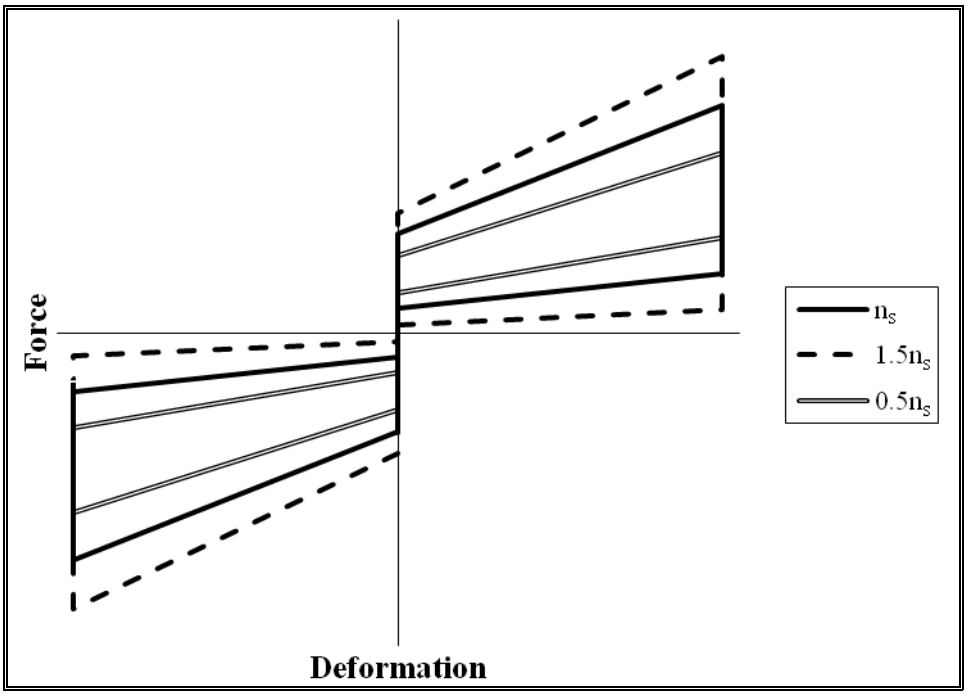

Figure 5-5: Hysteretic behavior changing the value of n_s

5.2 Important Variables

As the friction coefficient (μ) and the angle of the slanted walls (α) are two of the most important variables in the behavior of the SCFD, a separate analysis is necessary. The two variables are correlated in the factors β_1 and β_2, where: $\beta_1 = n_s(\sin(\alpha) + \mu\cos(\alpha))$ and $\beta_2 = n_s(\sin(\alpha) - \mu\cos(\alpha))$, with n_s being the number of sliding walls per friction wedge. These parameters are very important in the hysteretic behavior since they appear in most of the equations shown in Chapter 2 of this thesis. Figure 5-6 shows β_1 for different values of α and μ.

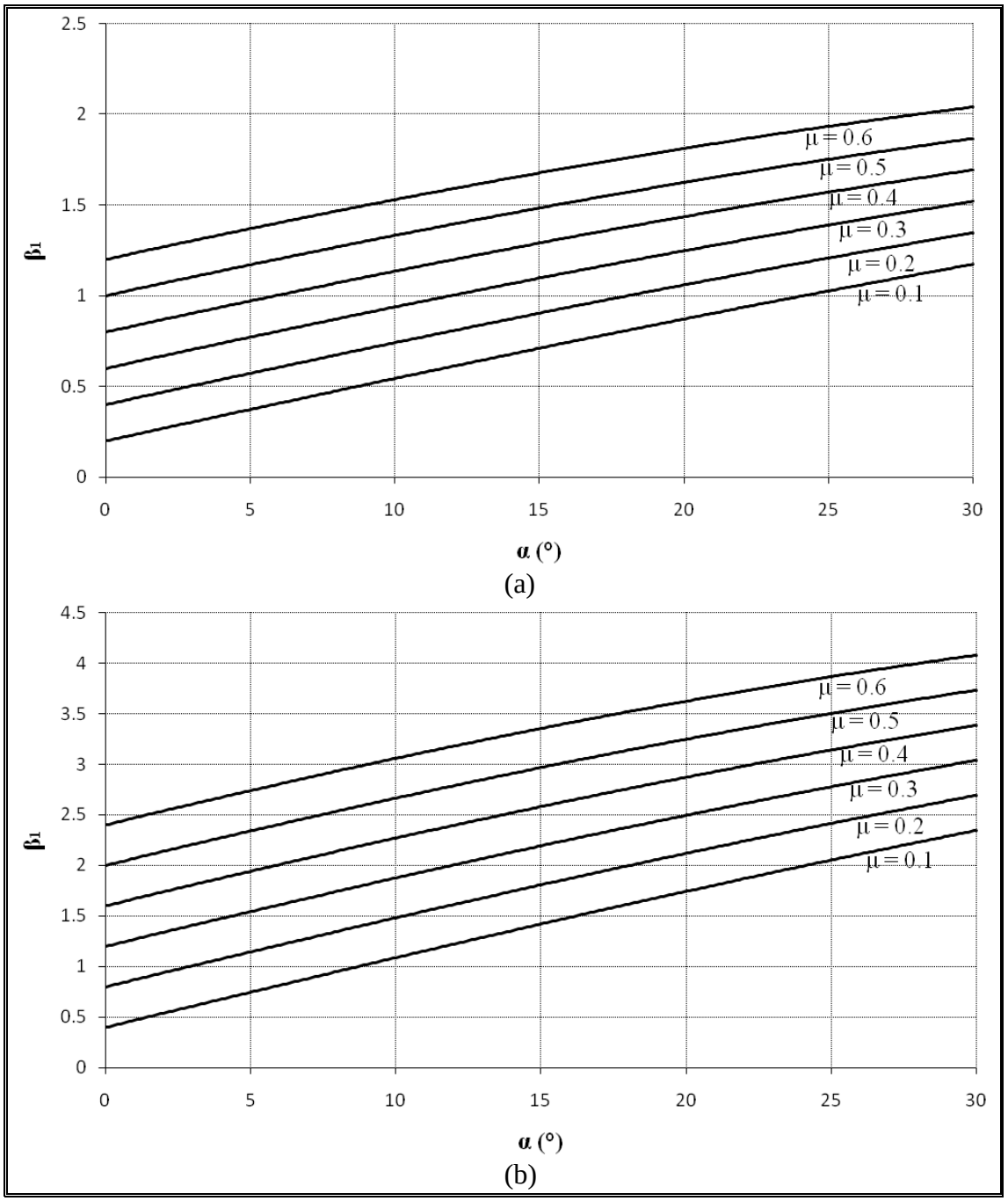

Figure 5-6: (a) β_1 for different values of α and μ with n_s=2, (b) β_1 for different values of α and μ with n_s=4

As expected, when the friction coefficient and the angle of the slanted walls increases, factor β_1 reaches a higher value. When using a certain angle α, the

designer can increase β_1 by using a sliding material with a higher μ. β_1 is important as it increases the stiffness of the loading process of the device (K_l).

Furthermore, Figure 5-7 shows β_2 for different values of α and μ.

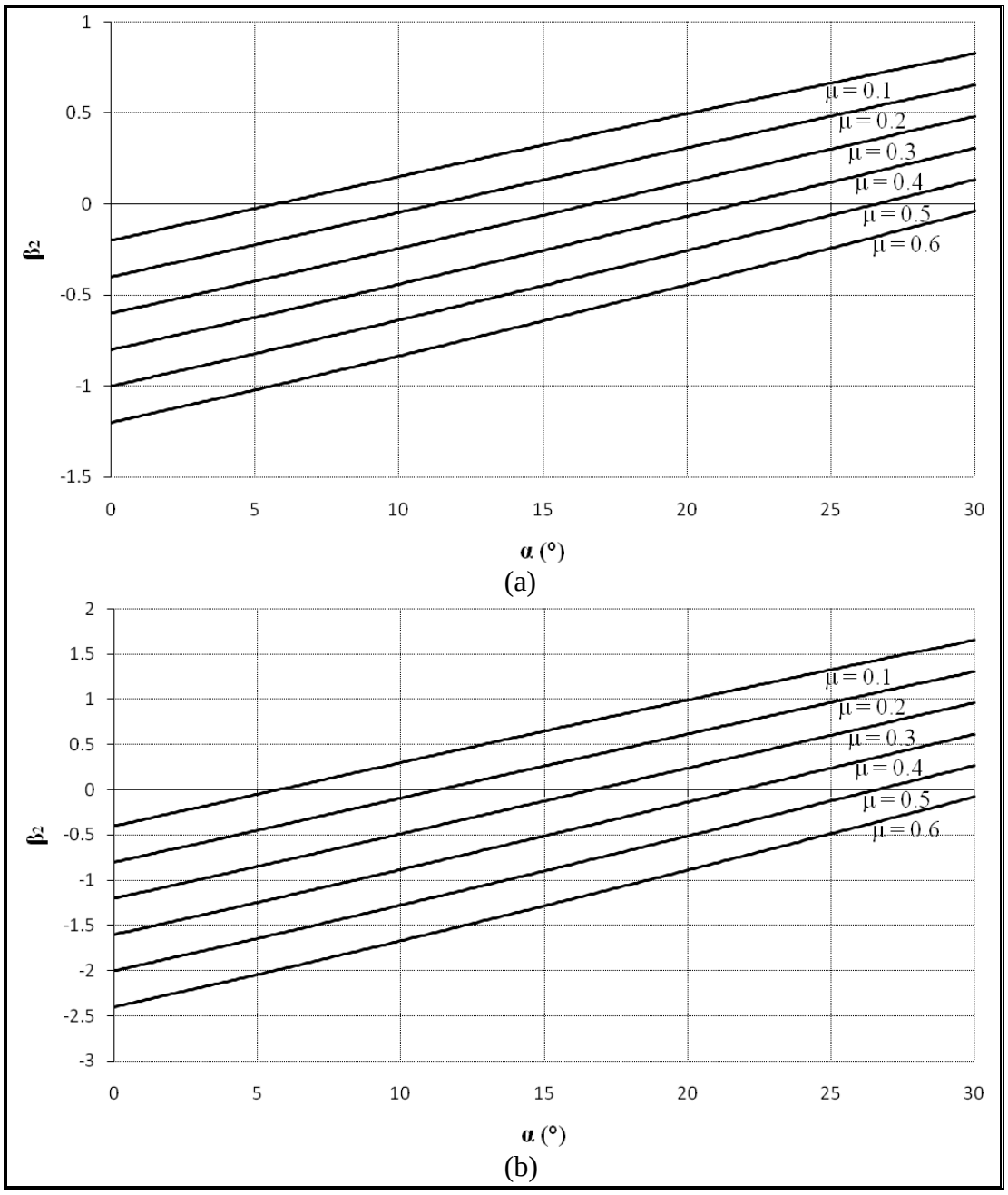

Figure 5-7: (a) β_2 for different values of α and μ with n_s=2, (b) β_2 for different values of α and μ with n_s=4

In this case, when the friction coefficient increases and the angle of the slanted walls decreases, factor β_2 reaches a lower value. When using a certain angle α, the designer can increase β_2 by using a sliding material with a lower μ. β_2 is important as it increases the stiffness of the unloading process of the device (K_u).

Moreover, it is interesting how the angle α and the friction coefficient μ changes the stiffness of the loading and unloading process of the device. This analysis will be made for given values of longitudinal and transverse stiffness (K_R and K_G). The stiffness used will match the values of the built prototype (K_R=0.60tonf/cm and K_G=9.8tonf/cm).

Figure 5-8 shows the variation of the stiffness of the loading process (K_l) for different values of α and μ. As the angle α increases, the friction coefficient becomes more important in the value of the stiffness K_l. An increase in μ would result in a much higher stiffness of the loading process. Note that K_l starts at α=0° with the value of K_R and increases as the angle rises.

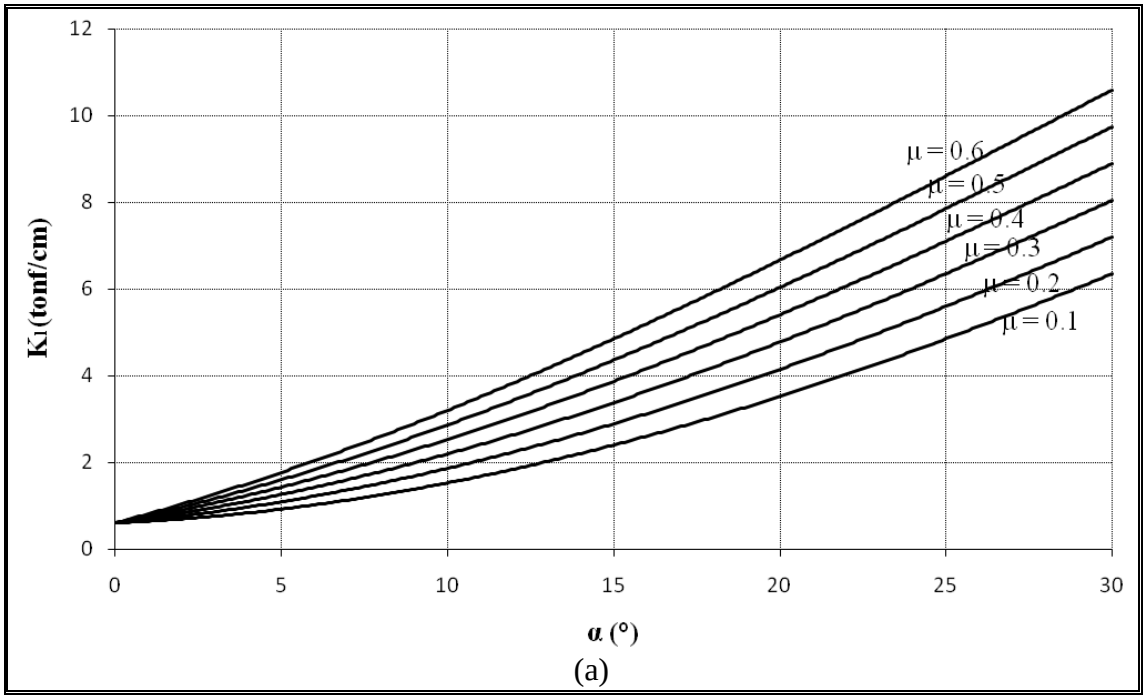

(a)

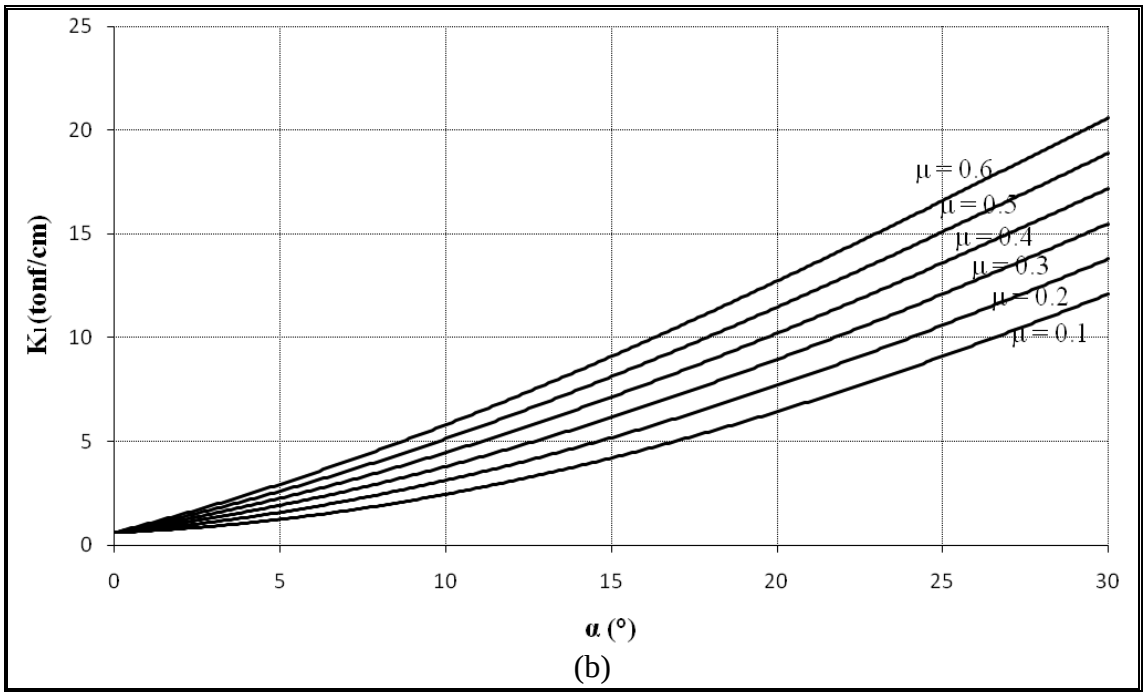

(b)

Figure 5-8: (a) K_l varying α and μ with n_s=2, K_R=0.6 tonf/cm and K_G=9.8 tonf/cm, (b) K_l varying α and μ with n_s=4, K_R=0.6 tonf/cm and K_G=9.8 tonf/cm

On the other hand, Figure 5-9 shows the variation of the stiffness of the unloading process (K_u) for different values of α and μ.

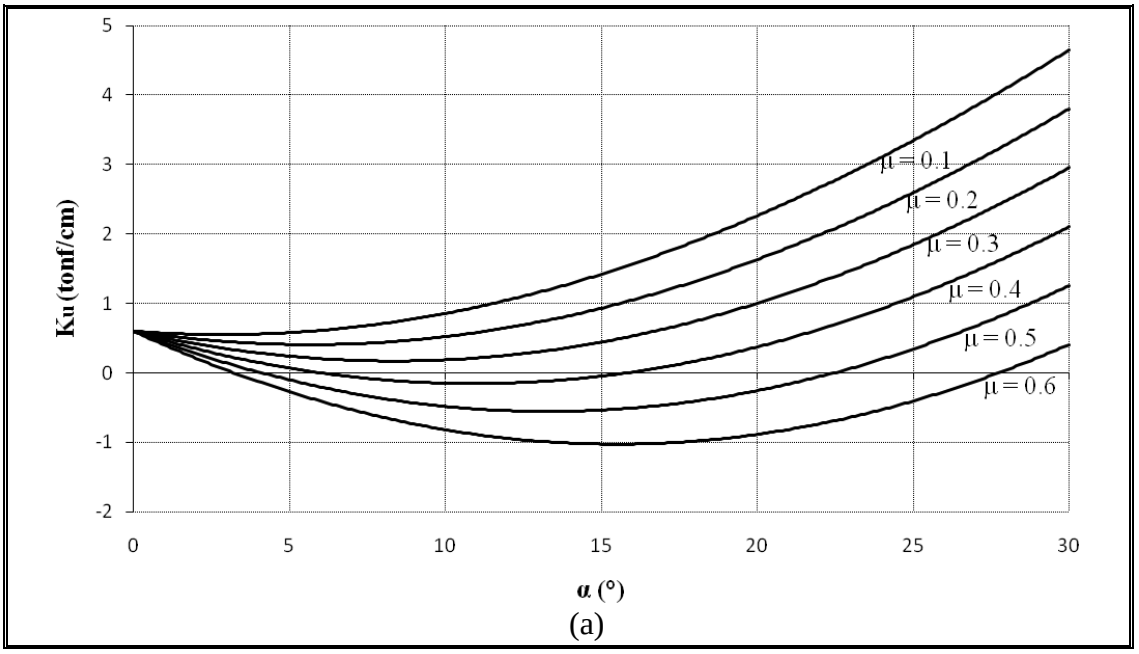

(a)

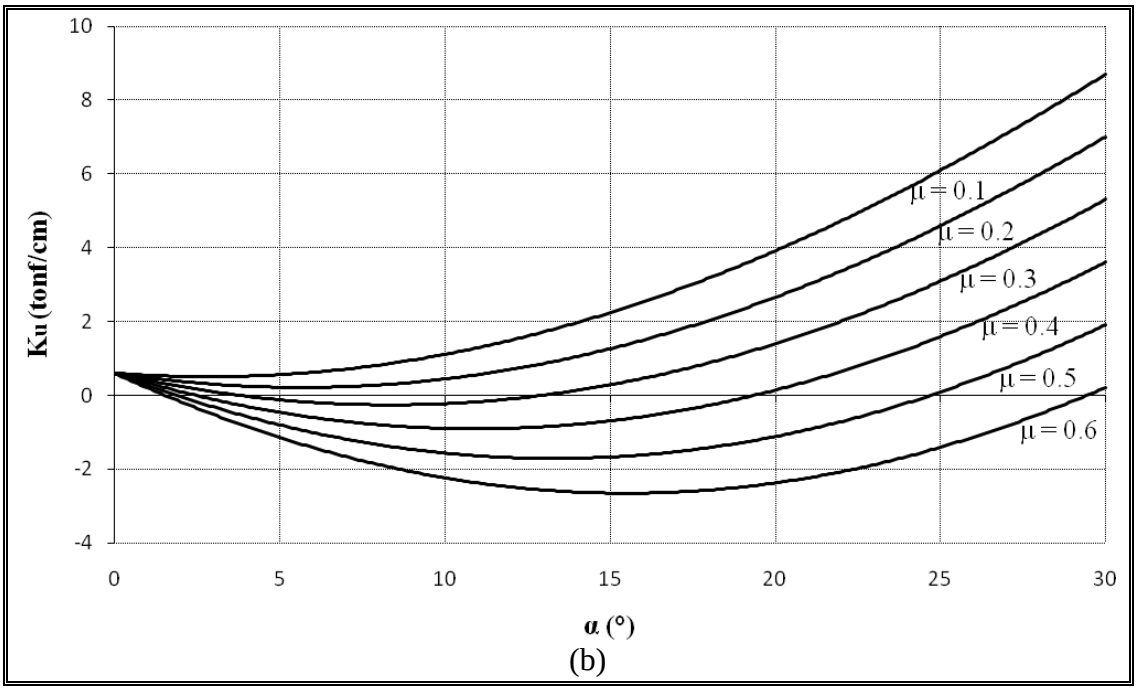

(b)

Figure 5-9: (a) K_u for different values of α and μ with n_s=2, K_R=0.6 tonf/cm and K_G=9.8 tonf/cm, (b) K_u for different values of α and μ with n_s=4, K_R=0.6 tonf/cm and K_G=9.8 tonf/cm

The stiffness of the unloading process, has a parabolic shape for big values of μ. K_u starts at α=0° with the value of K_R, just as K_l. For n_s=2 note that when μ≥0.4 there are some values of α that makes K_u negative. This happens for n_s=4 when μ≥0.3. If K_u is negative, the internal friction wedge would jam at the moment of unloading and the self-centering behavior of the device would be lost.

Furthermore, the design of the device is controlled by the capability of energy dissipation. Dissipated energy per cycle is defined as the area of the hysteretic loop. Figure 5-10 shows the variation of the dissipated energy for different values of α and μ. As the angle α increases, the friction coefficient becomes more important in the quantity of dissipated energy. An increase in μ would result in a device with a much higher energy dissipating capabilities.

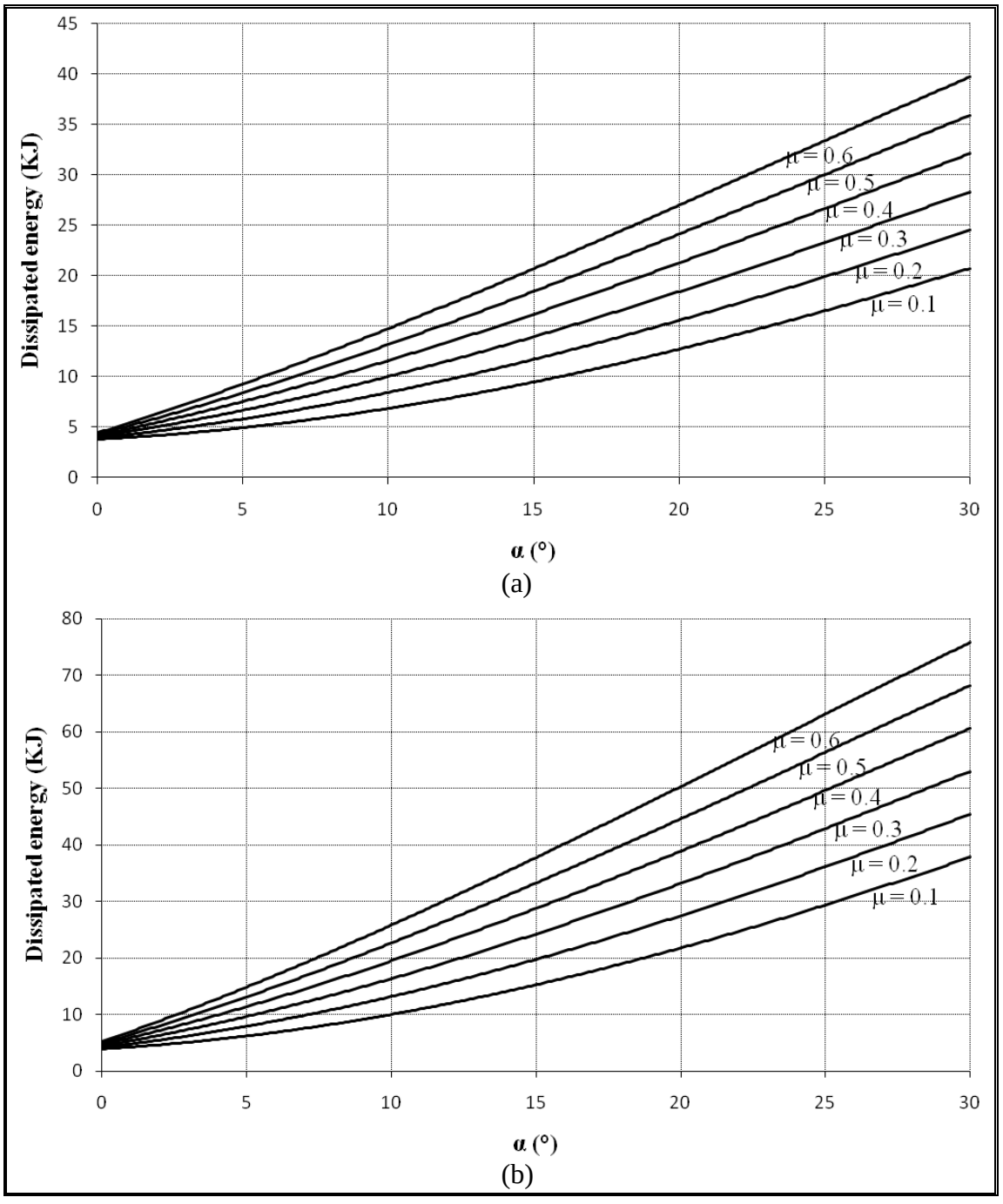

Figure 5-10: (a) Dissipated energy for different values of α and μ with n_s=2, K_R=0.6 tonf/cm and K_G=9.8 tonf/cm, (b) Dissipated energy for different values of α and μ with n_s=4, K_R=0.6 tonf/cm and K_G=9.8 tonf/cm

5.3 Self-Centering Behavior

In order to be a self-centering device, the internal friction wedge must return to its original position once the load is reversed. There are two conditions that must be satisfied: (i) the stiffness of the process of unloading (K_u) has to be positive and (ii) the force when the device returns to its pre-loaded configuration (F_u) has to be bigger or equal than zero. These conditions are presented in equations (5.1) and (5.2) respectively.

$$K_R + \beta_2 K_G \sin(\alpha) > 0 \tag{5.1}$$

$$K_R \Delta_0 + K_G \Delta_{0G} \beta_2 \geq 0 \tag{5.2}$$

Where K_R is the stiffness of the longitudinal spring, K_G is the stiffness of the transverse springs, α is the angle of the slanted walls, Δ_0 is the pre-deformation of the longitudinal spring, Δ_{0G} is the pre-deformation of the transverse springs and $\beta_2 = n_s(\sin(\alpha) - \mu\cos(\alpha))$, with n_s being the number of sliding walls per friction wedge and μ being the friction coefficient between steel and the sliding material. Equations (5.1) and (5.2) can be rewritten as:

$$\beta_2 > \frac{-K_R}{K_G \sin(\alpha)} \tag{5.3}$$

$$\beta_2 \geq \frac{-K_R \Delta_0}{K_G \Delta_{0G}} \tag{5.4}$$

If $\gamma_1 = \frac{-K_R}{K_G \sin(\alpha)}$ and $\gamma_2 = \frac{-K_R \Delta_0}{K_G \Delta_{0G}}$, the conditions that must be satisfied in order to have a self-centering behavior can be written as:

$$\beta_2 > \gamma_1 \tag{5.5}$$

$$\beta_2 \geq \gamma_2 \tag{5.6}$$

Equation (5.5) controls the design when $\frac{1}{\sin(\alpha)} < \frac{\Delta_0}{\Delta_{0G}}$ and equation (5.6) controls when $\frac{\Delta_0}{\Delta_{0G}} < \frac{1}{\sin(\alpha)}$. Figure 5-11 shows the variation of the factor γ_1 for different values of α and different K_R/K_G ratios.

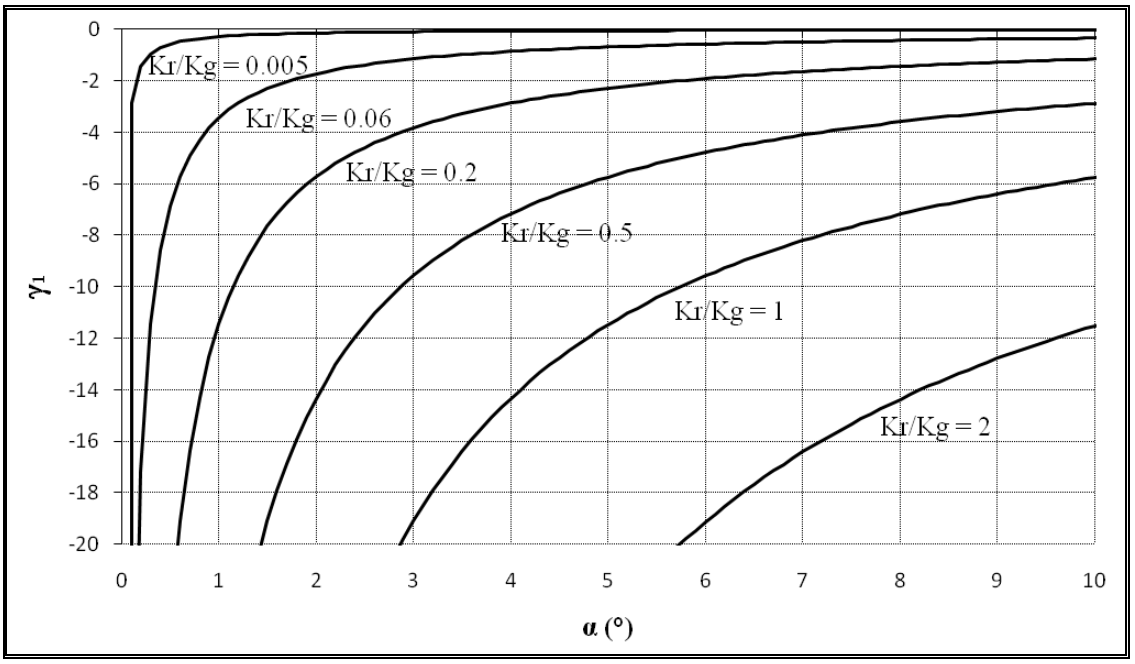

Figure 5-11: Variation of factor γ_1

For small values of the ratio K_R/K_G the designer must be careful to satisfy equation (5.5) as γ_1 increases its value. As β_2 is negative for small values of α and big values of μ, caution must be taken in these cases. Therefore, equation (5.5) must be checked specially when using small values of K_R/K_G with a small angle α and a big friction coefficient μ. Figure 5-12 shows γ_1 and β_2 in the same graph. For this double Y-axis chart, γ_1 is plotted with a solid black line at its left axis and β_2 is plotted as hollow lines at its right axis. Figure 5-12a shows the case when the

number of sliding walls per friction wedge is two (n_s=2), while Figure 5-12b shows the case when the number of sliding walls per friction wedge is four (n_s=4).

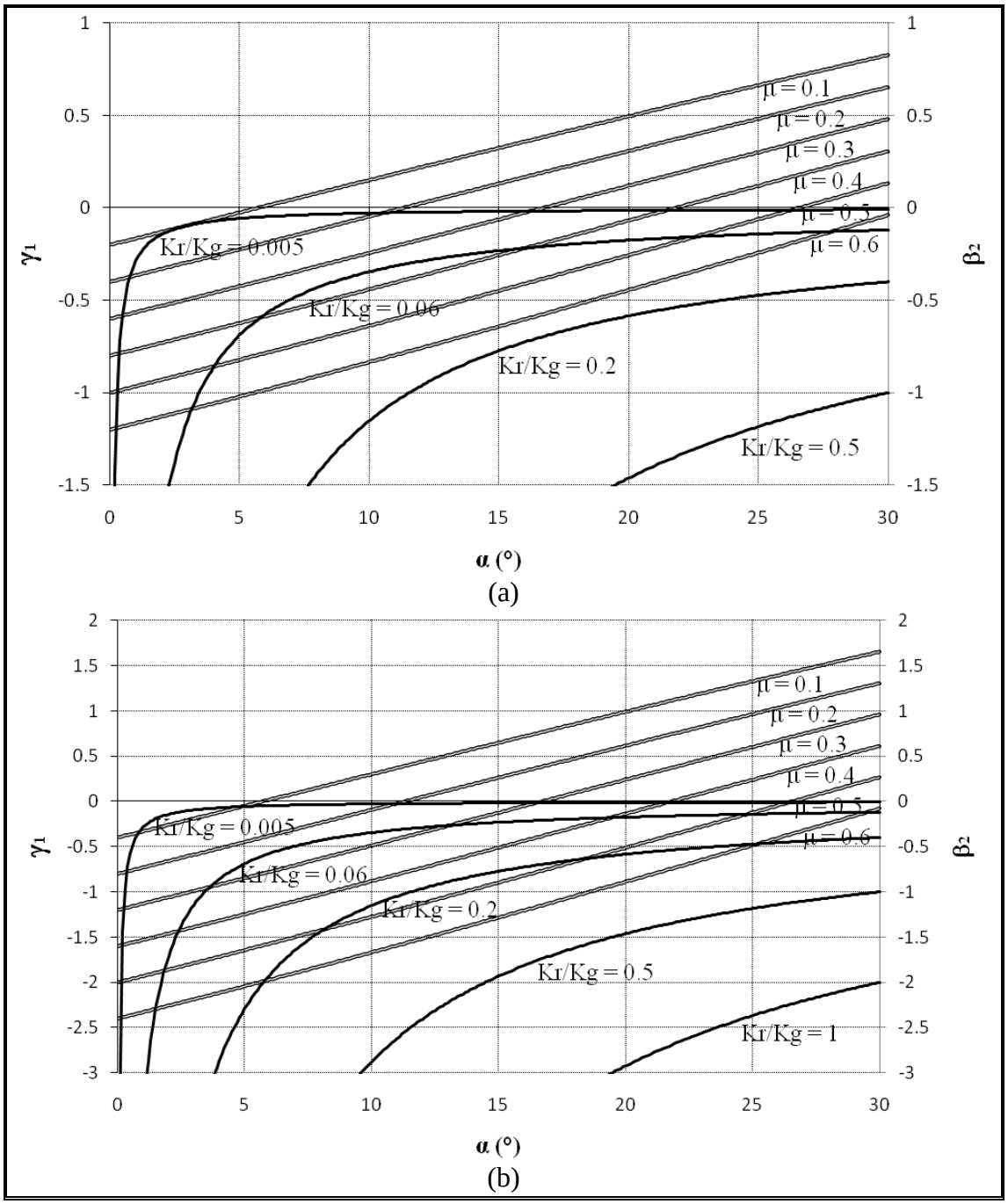

Figure 5-12: (a) γ_1 and β_2 for different values of K_R/K_G, α and μ with n_s=2, (b) γ_1 and β_2 for different values of K_R/K_G, α and μ with n_s=4

When n_s=2, ratios K_R/K_G bigger than 0.2 with μ<0.6 will always satisfy equation (5.5). On the other hand, when n_s=4 this will happen for ratios K_R/K_G bigger than 0.4 and μ<0.6. The designer has to be careful when using small ratios of K_R/K_G, a big friction coefficient and a small angle α, as γ_1 increases and the self-centering behavior of the device may be at the limit of non-compliance.

Figure 5-13 shows the variation of the factor γ_2 for different values of Δ_0/Δ_{0G} ratios and different K_R/K_G ratios.

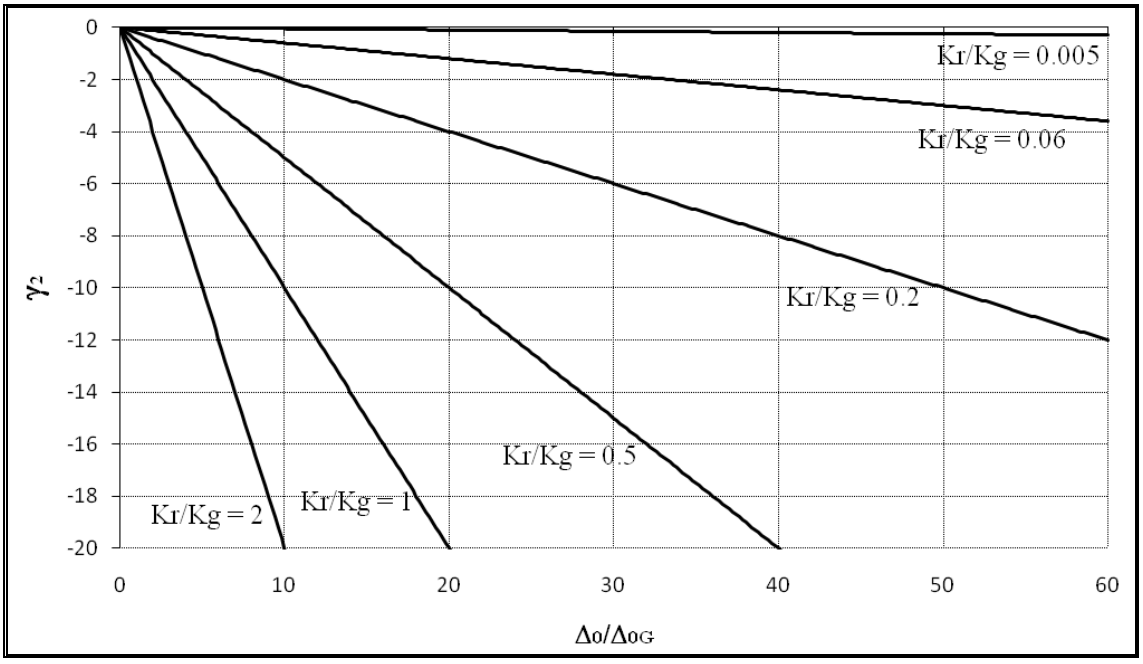

Figure 5-13: Variation of factor γ_2

As with γ_1, for small values of the ratio K_R/K_G the designer must be careful to satisfy equation (5.6). A smaller ratio Δ_0/Δ_{0G} will make equation (5.6) harder to comply as γ_2 increases its value. Since β_2 is negative for small values of α and big values of μ, caution must be taken in these cases. When using small values of K_R/K_G, Δ_0/Δ_{0G}, angle α and a big friction coefficient μ, special attention to equations (5.5) and (5.6) is required so the self-centering behavior of the device is maintained.

6 FRICTION EXPERIMENTS

Presented in this section are the friction experiments and the results for four different materials. The used mechanism, the friction coefficients obtained and their respective analysis are discussed in this chapter.

6.1 Details of the Experiment

The experiment consists in a sliding rod, one fixed support, an external cap, the test material, two steel plates and four compression springs. Figure 6-1 shows the different parts of the device.

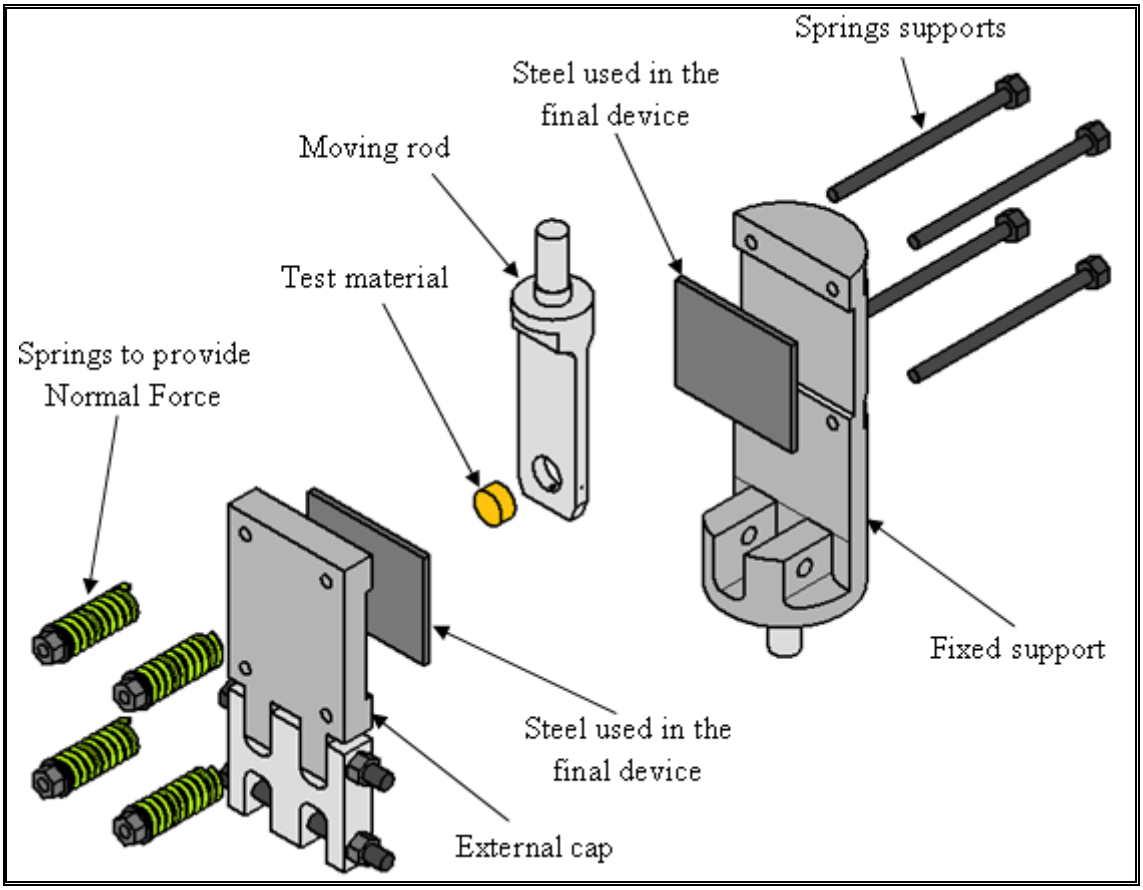

Figure 6-1: Different parts of the friction experiment

As the moving rod provides the support for the test material, the compression springs gives the normal force necessary to test different conditions. There are three types of springs with different stiffness, in order to cover a range of normal forces. Figure 6-2 shows the final assembled device. Note that this experiment is similar to the Sandwich friction experiment commonly done in geophysics to measure the friction between rocks (Xing & Makinouchi, 2002).

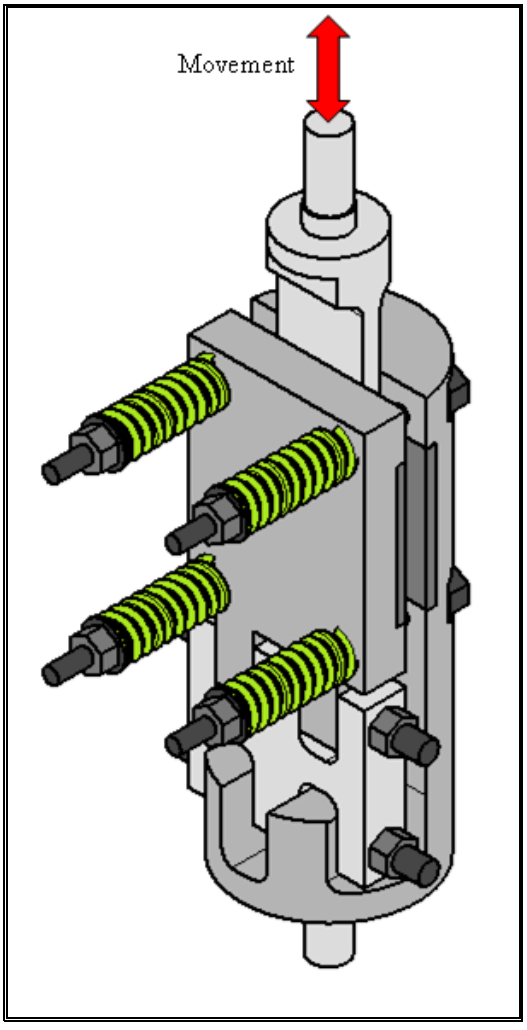

Figure 6-2: Assembled device for friction experiments

A schematic section cut is shown in Figure 6-3. Note that there are two sliding surfaces given by the steel plates used in the final device. Once an experiment is

completed, the steel plates are removed and polished in order to avoid affecting the next experiment.

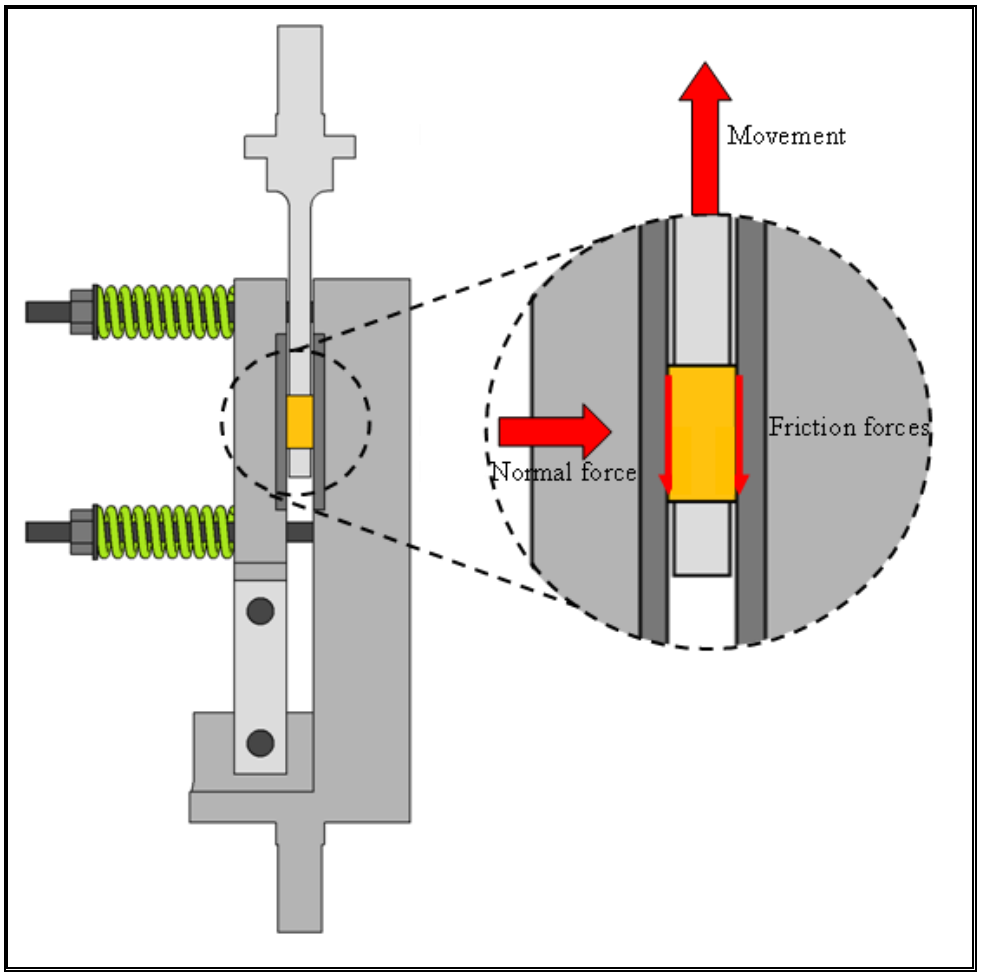

Figure 6-3: Schematic section cut for the proposed mechanism

Figure 6-4 shows actual photographs of the device and the friction experiments performed.

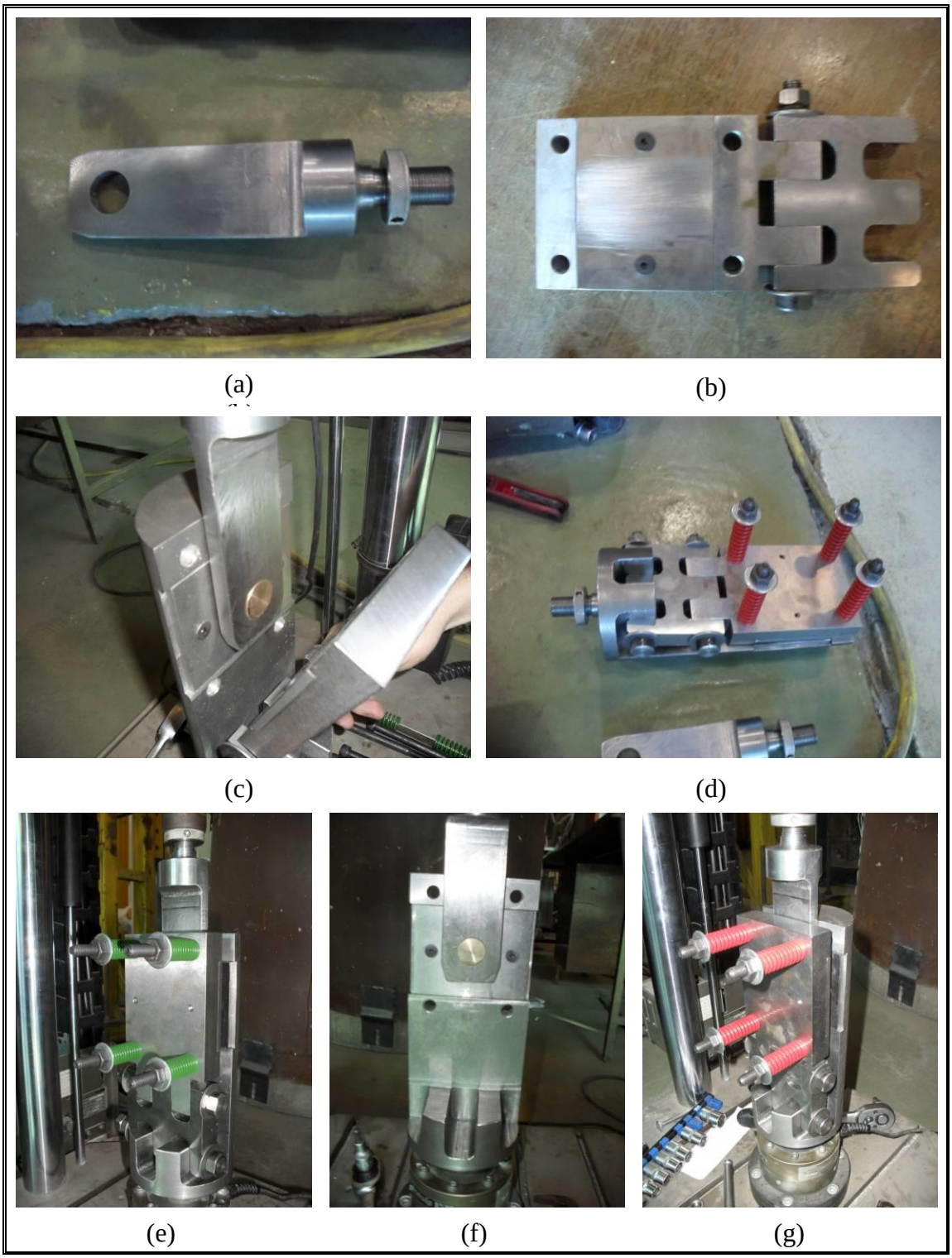

Figure 6-4: Actual photographs of the friction experiments

6.2 Results

The tested specimens were two types of bronze and two types of brake material. The first bronze (BR01) is a high leaded tin bronze with an approximate chemical composition of 83% Cu, 7% Pb, 6.5% Sn, 3% Zn and 0.5% Ni. The second bronze tested (BR02) also consists in a high leaded tin bronze but with an approximate chemical composition of 80% Cu, 10% Pb and 10% Sn. Test material number 3 (BM01) is a typical brake lining composed of a relatively soft but tough and heat resistant material with a high coefficient of friction. Finally, test material number 4 (BM02) is a woven brake lining. The carcass consists of brass wire inserted yarns containing a mixture of organic and inorganic fibers. This type of material is used in high duty applications like industrial brakes or mining equipments were high friction is required. Figure 6-5 shows the test materials used in the friction experiments.

(a) BR01

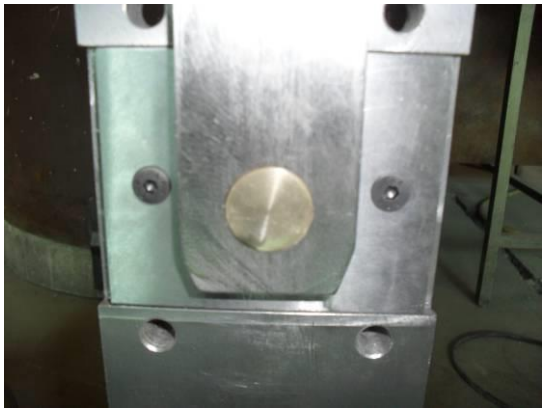

(b) BR02

(c) BM01 (d) BM02

Figure 6-5: Test materials for friction experiments

As the friction coefficients vary considerably for different pressures and sliding velocities (Savaskan & Bican, 2010), various tests were performed. All experiments were tested with a sawtooth wave with amplitude 10mm varying the frequencies and normal forces. Shown in Figure 6-6 are the results for test material number 1 (BR01). Note that σ is the compressive stress in each experiment.

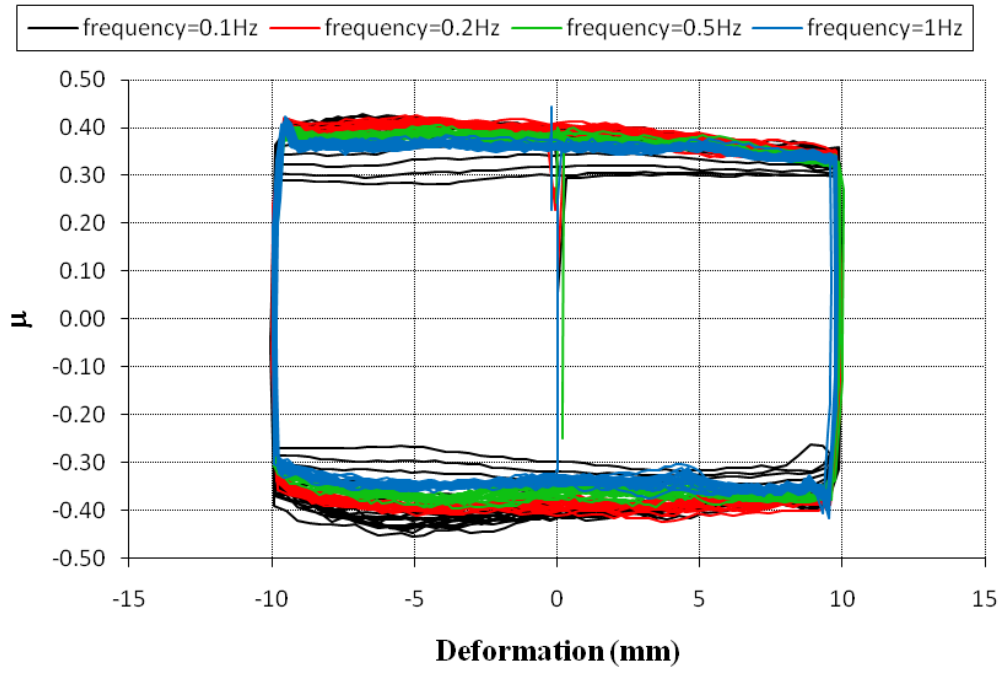

(a)

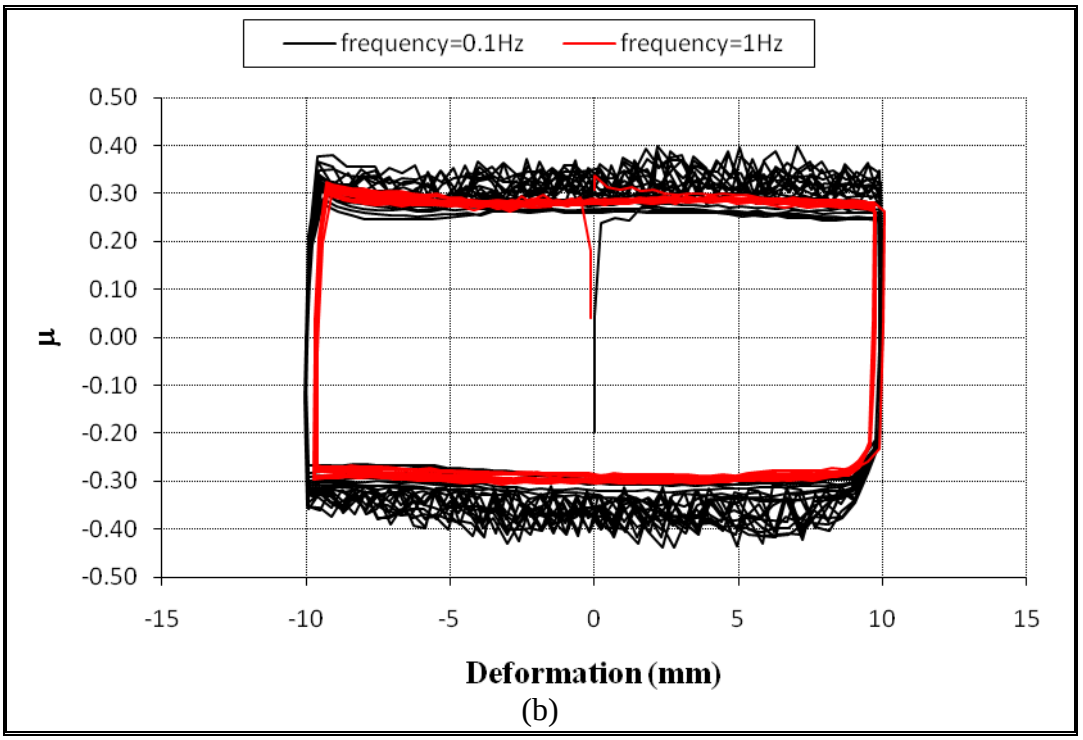

(b)

Figure 6-6: Friction coefficient for test material BR01 against steel, with: (a) σ=7kgf/cm^2, (b) σ=30kgf/cm^2

For design purposes, the friction coefficient of material BR01 can be estimated in an approximate value of μ=0.34. Note that when the normal force rises, the friction coefficient decreases. On the other hand, when the frequencies are increased the friction coefficient decreases.

Figure 6-7 shows the results for test material BR02. In this case, an approximate value of μ=0.26 can be estimated for design purposes. Like test material BR01, when the normal forces and the frequencies increases, the friction coefficient decreases. Note that friction coefficients for bronze are in the range of common values (Singh, Cai & Bellon, 2007; Zoltan, Karoly, Laszlo & Klaus, 1999).

Shown in Figure 6-8 are the results for test material BM01. As expected, the friction coefficient for this material is higher than the other two materials tested. An approximate value for design has been estimated in μ=0.47. Note that when the normal force and the frequency increase, the friction coefficient also increases.

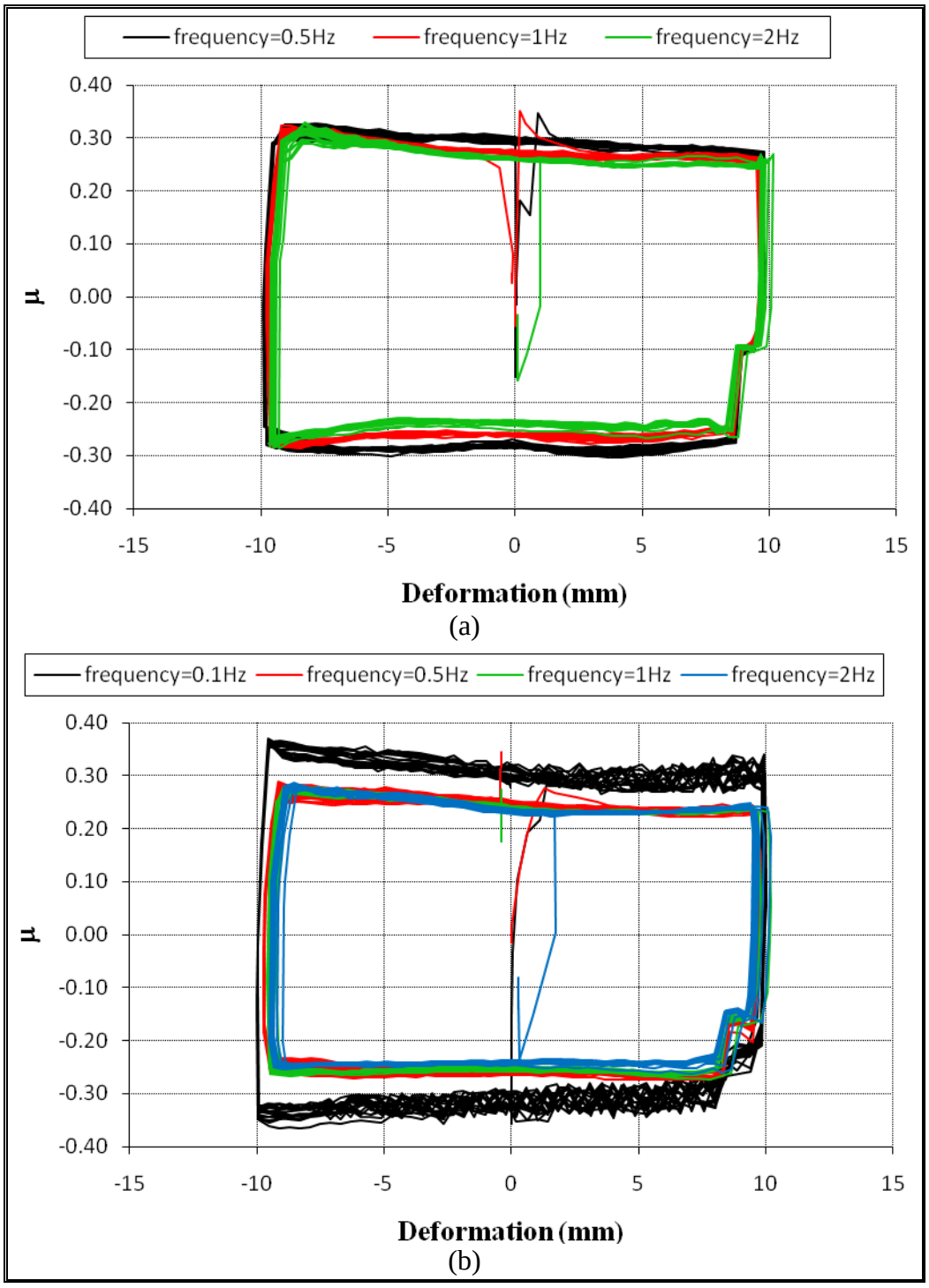

Figure 6-7: Friction coefficient for test material BR02 against steel, with: (a) σ=15kgf/cm^2, (b) σ=30kgf/cm^2

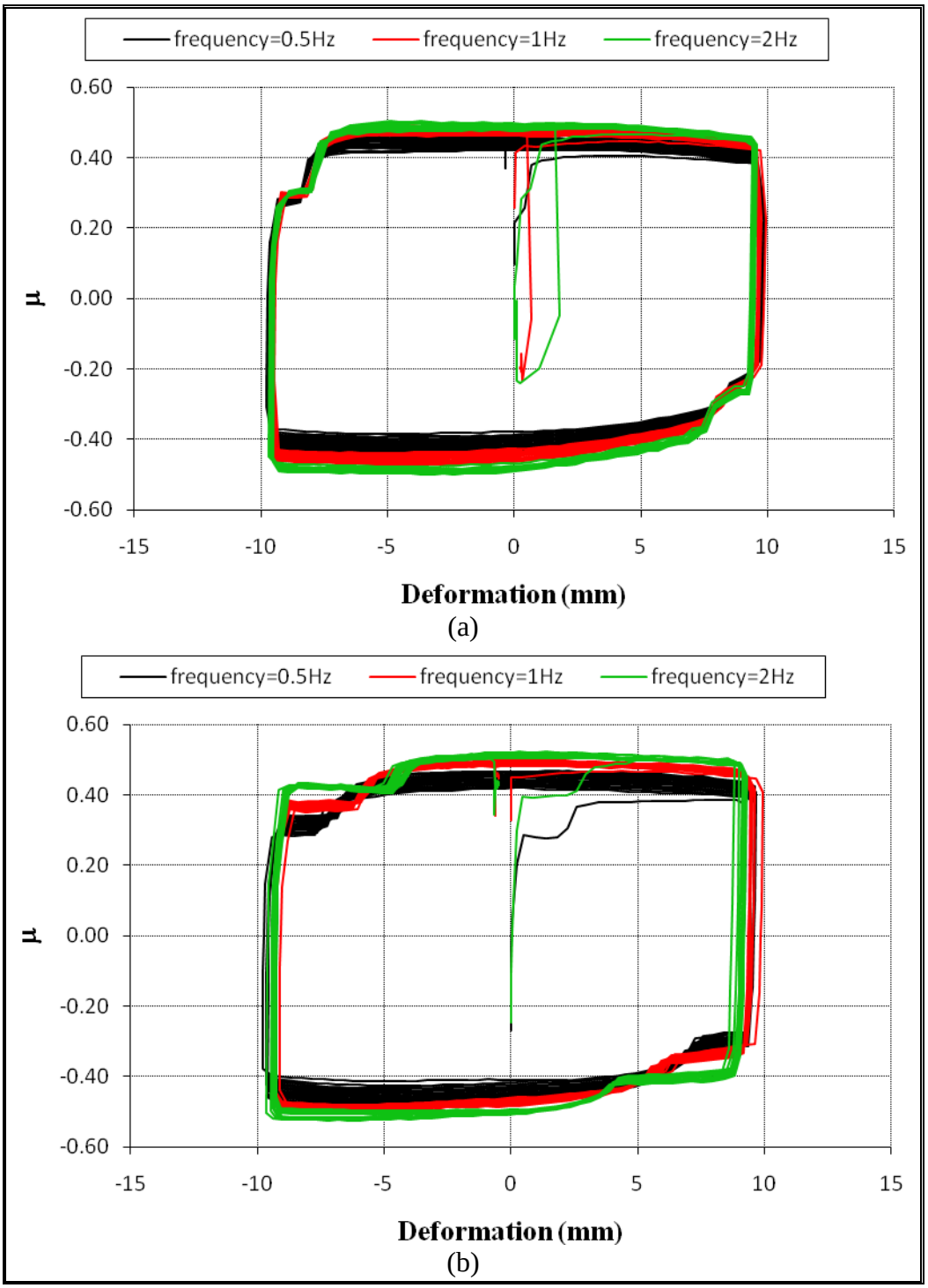

Figure 6-8: Friction coefficient for test material BM01 against steel, with: (a) σ=15kgf/cm^2, (b) σ=30kgf/cm^2

Finally, Figure 6-9 shows the results for test material BM02. In this case the highest friction coefficient is recorded, with an approximate value of μ=0.53 for design purposes. As with material BM01, when the normal force and the frequency increase, the friction coefficient also increases. Note that when using high normal forces, the friction coefficient is far more stable than in other cases, having small changes for different frequencies.

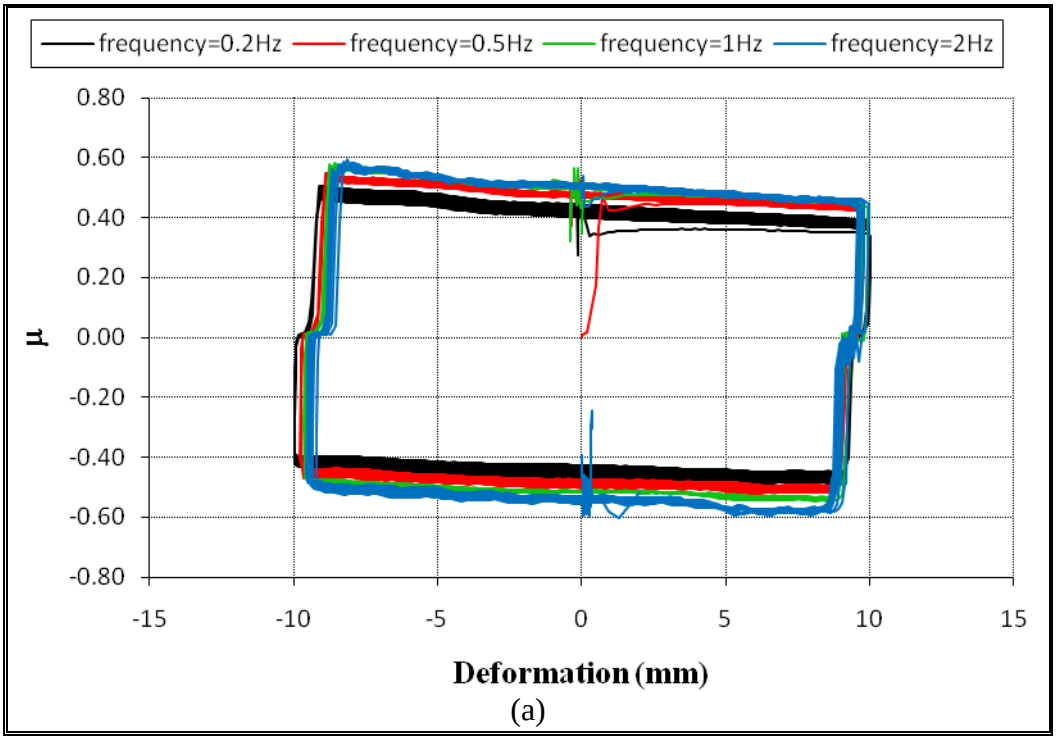

(a)

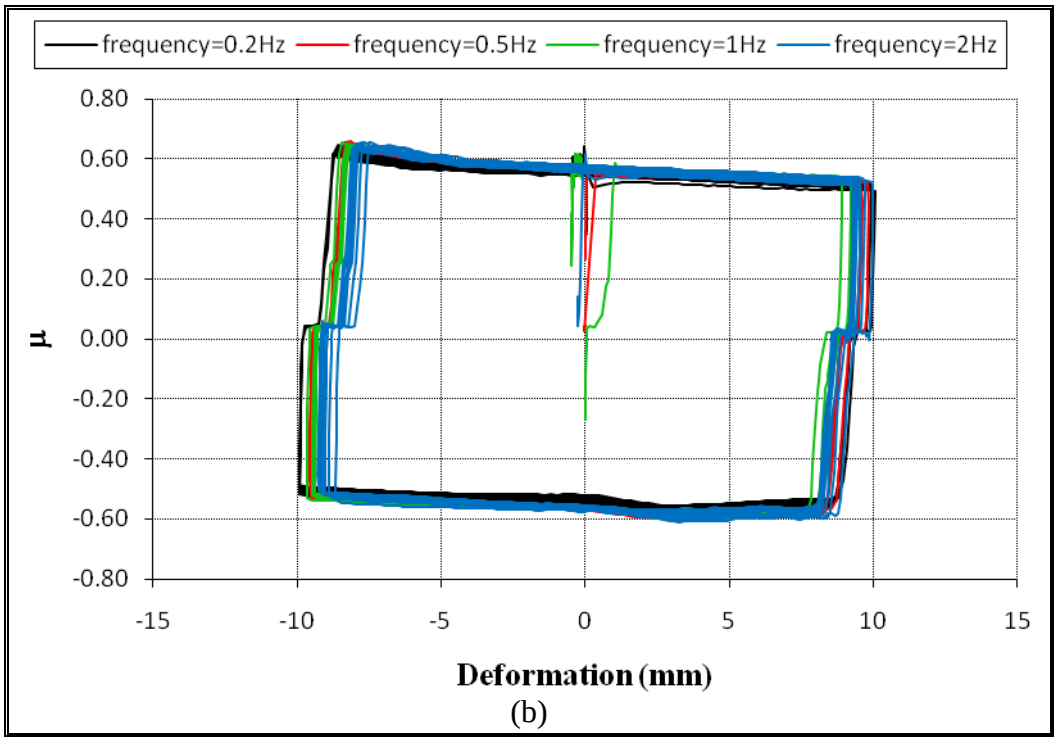

(b)

Figure 6-9: Friction coefficient for test material BM02 against steel, with: (a) σ=15kgf/cm^2, (b) σ=30kgf/cm^2

6.3 Results Analysis

In order to choose the final sliding material the prototype will use, a more thorough analysis of the results are necessary. Figure 6-10 shows the variation of the friction coefficient (μ) for different sliding velocities and compressive stresses (σ) for every tested material.

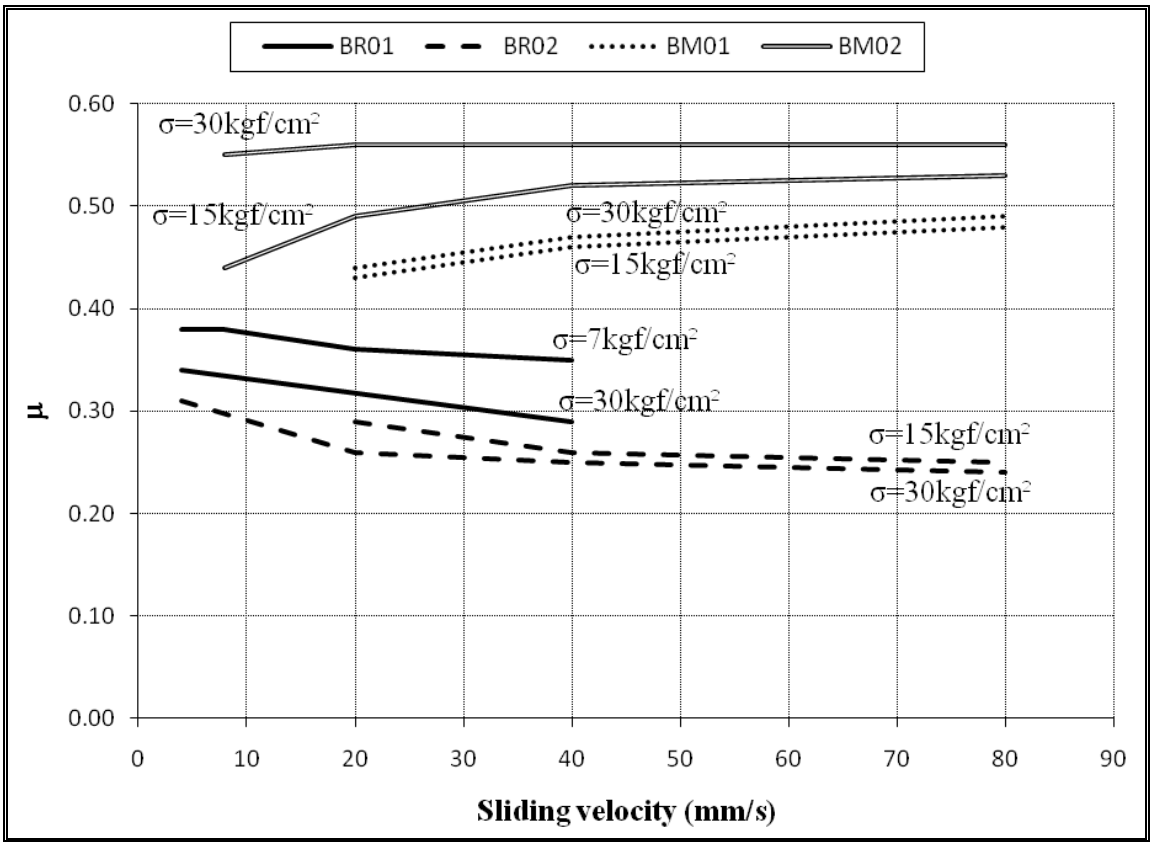

Figure 6-10: Friction coefficient for different sliding velocities and compressive stresses

As expected, both brake materials (BM01 and BM02) have bigger friction coefficients than the bronze materials (BR01 and BR02). Note that in materials BR01 and BR02 the friction coefficient decreases for bigger compressive stresses and bigger sliding velocities, while for BM01 and BM02 the friction coefficient increases in these conditions. Material BM02 will be used in the final prototype since more energy is dissipated and a high compressive stress will result in an almost constant μ, independent of the sliding velocity. Note that all friction coefficients are in the range of consistent literature values (Rabinowicz, 1995).

7 RUBBER EXPERIMENTS

Although the final designed prototype has no rubber elements, it is important to understand how this device would behave for a possible design using these elements. To achieve this, four different rubber composites were tested in a simple compression test. After choosing a rubber composite, two different configurations and shapes of this material were tested in laboratory. This section compares the experimental results with what should be obtained with the equations available in the literature. Finite element models are made to estimate the results in a more accurate way.

7.1 Original Experiments

Four cylinder shaped rubber test tubes were made, each corresponding to a different composite. The tested composites were: rubber 513, 812, L60 and LHDS. Note that composites 513 and 812 are typically used for seismic isolators and composites L60 and LHDS are used for applications requiring wear and high impact resistance. Figure 7-1 shows pictures of the actual test tubes.

(a)

(b)

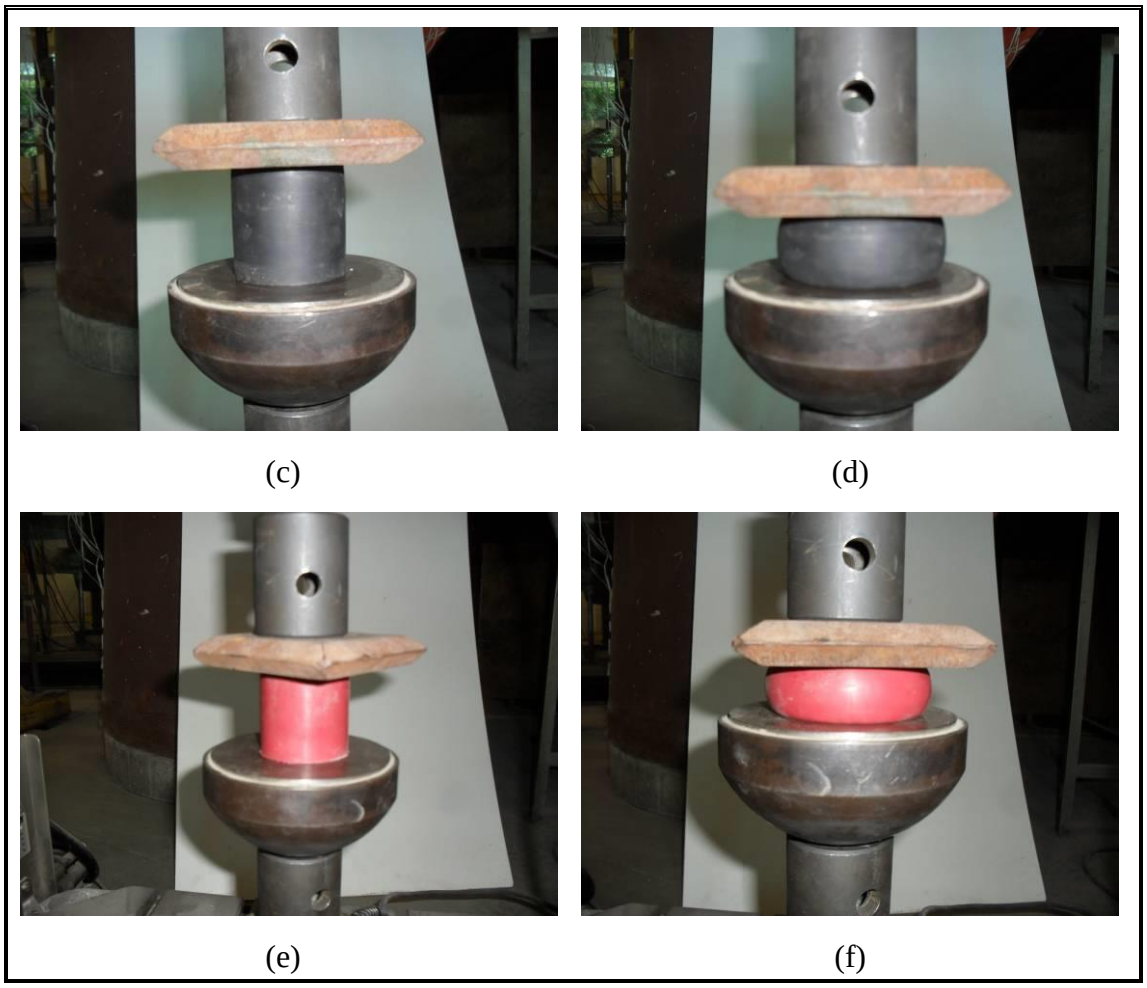

(c) (d)

(e) (f)

Figure 7-1: Pictures of the original rubber experiments

Each rubber composite was tested in simple compression for a sine wave input varying the amplitude and the frequency of the experiment. Figure 7-2 shows the resulting stress-strain (σ-ε) curves for each rubber composite.

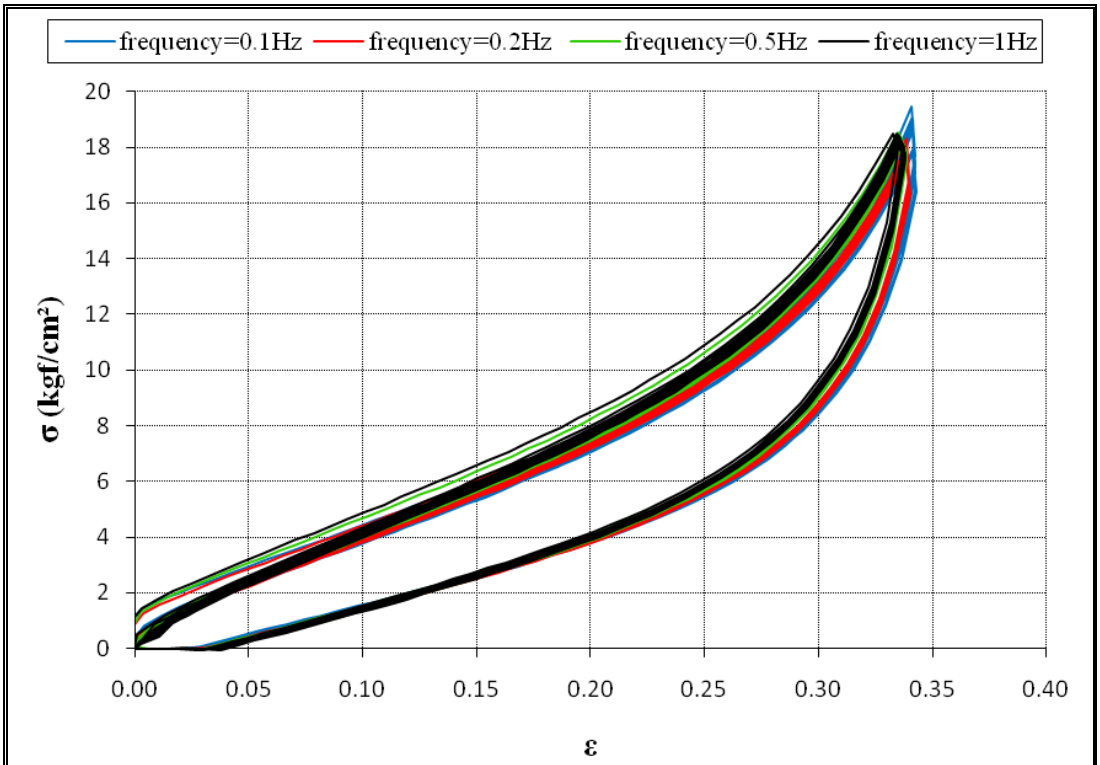

(a) Rubber 513

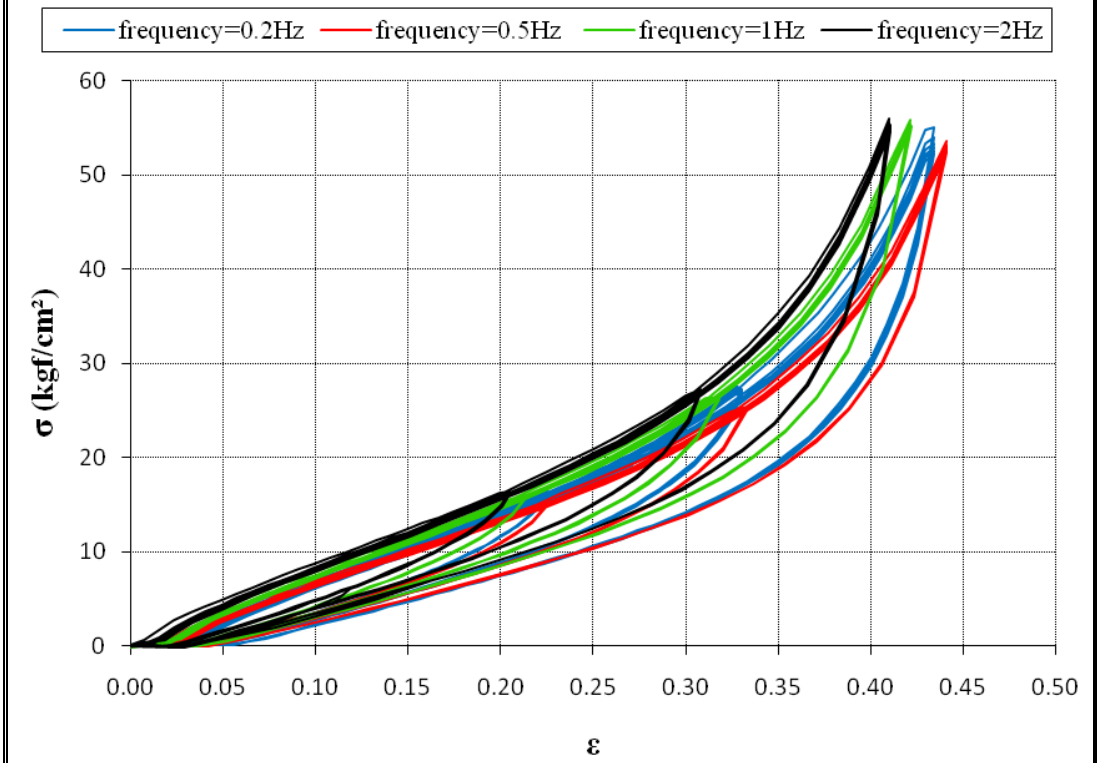

(b) Rubber 812

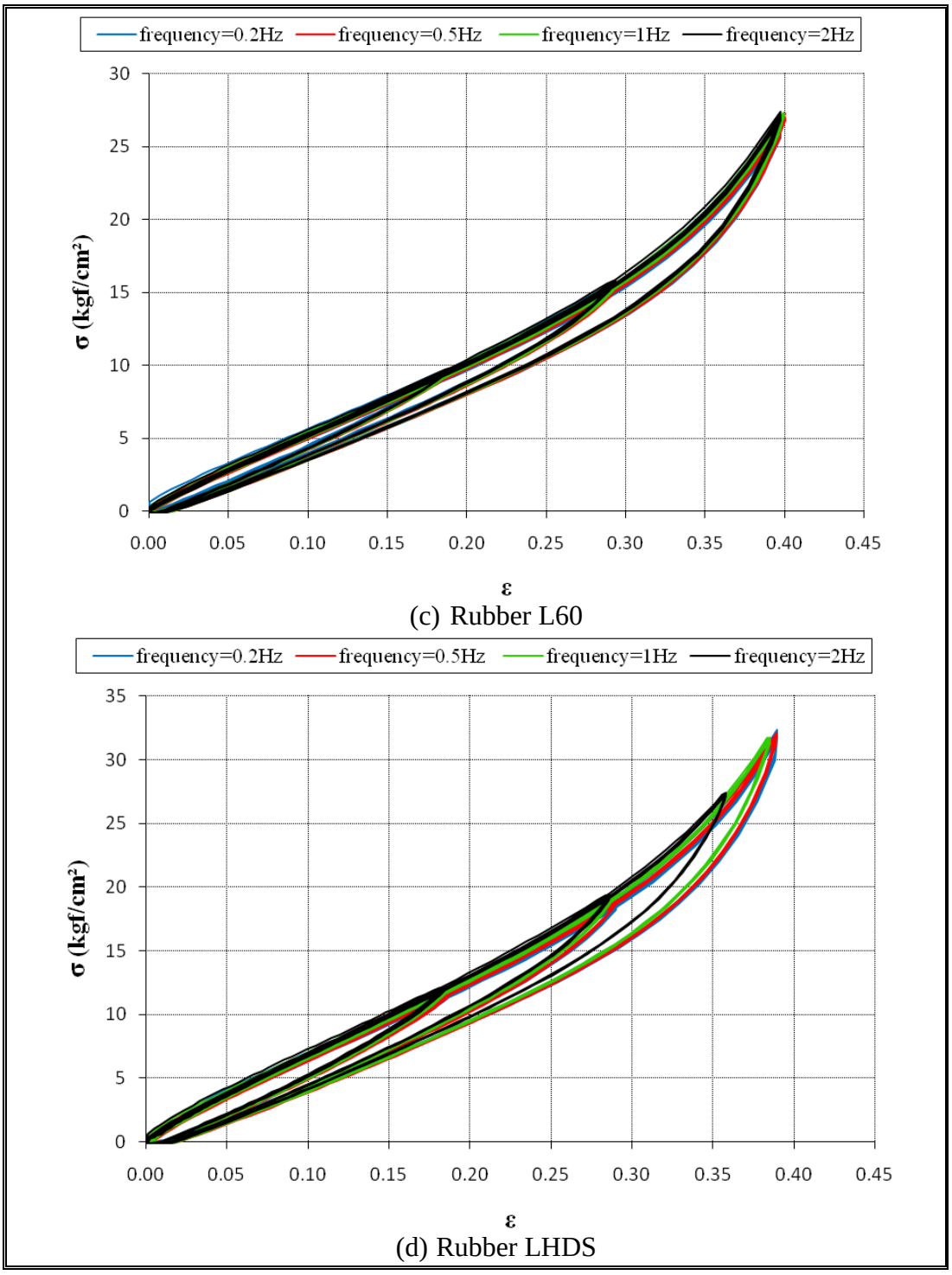

(c) Rubber L60

(d) Rubber LHDS

Figure 7-2: Stress-strain curves for rubber composite: (a) 513, (b) 812, (c) L60, (d) LHDS

Rubbers L60 and LHDS has a more elastic behavior than composites 513 and 812, where nonlinear behavior dominates. Although composite 812 have the highest stiffness, its behavior varies significantly for different frequencies. Since composite LHDS has a higher stiffness than L60, this type of rubber is recommended for eventual devices.

7.2 Theory and Experiments for Different Configurations

Having chosen composite LHDS for possible rubber springs, is necessary to predict what happens for different shapes and configurations of rubber. A simple approximation, using available equations in the literature (Naeim & Kelly, 1999), is presented and compared with the actual experimental results.

First of all, an initial constant value of the instantaneous compression modulus of the rubber-steel composite (E_C) is estimated from the original experiments of rubber LHDS (Figure 7-2d). The values for the shear modulus and Young modulus of composite LHDS are obtained using equations (7.1) and (7.2).

$$G = \frac{E_c}{6S^2} \tag{7.1}$$

$$E = 2G(1+\nu) \tag{7.2}$$

Where G is the shear modulus of rubber LHDS, E_c is the instantaneous compression modulus of the rubber-steel composite estimated from the original experiments, S is the shape factor, E is the Young modulus and ν is the Poisson ratio for rubber (a value of ν = 0.4997 is used). The shape factor S is defined by equation (7.3) and for a cylindrical shape can be written as equation (7.4).

$$S = \frac{loaded\ area}{force - free\ area} \tag{7.3}$$

$$S = \frac{R}{2t} \tag{7.4}$$

Where S is the shape factor, R is the radius of the cylinder and t is the thickness of the rubber.

Two different shapes of the rubber springs will be analyzed: a tubular one and a rectangular one with a steel plate in the middle. For the tubular shape, the shape factor S and the instantaneous compression modulus of the rubber-steel composite E_C are calculated with equations (7.5) and (7.6).

$$S = \frac{b-a}{2t} \tag{7.5}$$

$$E_C = \frac{3G}{2t^2}\left\{b^2 + a^2 - \left[\frac{b^2 - a^2}{\ln\left(\frac{b}{a}\right)}\right]\right\} \tag{7.6}$$

Where S is the shape factor, E_c is the instantaneous compression modulus of the rubber-steel composite, a is the inner radius of the tube, b is the outer radius of the tube and t is the thickness of the rubber. On the other hand, for the rectangular shape equations (7.5) and (7.6) can be written as:

$$S = \frac{ab}{2t(a+b)} \tag{7.5}$$

$$E_C = 6.73GS^2 \tag{7.6}$$

Where S is the shape factor, E_c is the instantaneous compression modulus of the rubber-steel composite, a is the larger edge of the rectangle, b is the smaller edge of the rectangle and t is the thickness of the rubber.

With the value of E_C estimated for each shape, the stiffness in the rubber springs can be calculated with equation (7.7).

$$K = \frac{E_C A}{H_R} \tag{7.7}$$

Where K is the axial stiffness of the rubber spring, E_c is the instantaneous compression modulus of the rubber-steel composite, A is the cross-sectional area of the rubber bearing and H_R is the total thickness of rubber in the spring.

Equations shown above are used to predict the force-deformation curve for a tubular and a rectangular shape of a rubber bearing. In order to prove the theory, two different shapes of rubber springs were tested in laboratory. Figure 7-3 shows pictures of the springs tested and the simple compression experiments performed.

(a) Tubular shape

(b) Tubular shape

(c) Rectangular shape

(d) Rectangular shape

Figure 7-3: Pictures of the rubber springs tested in laboratory

Each rubber spring was tested in simple compression for a sine wave input. Figure 7-4 shows the resulting force-deformation curves for each rubber spring. Note that for the rectangular spring only a portion of the force-deformation curve is shown, because loading was divided in parts so that the capacity of the experimental mechanism was not exceeded.

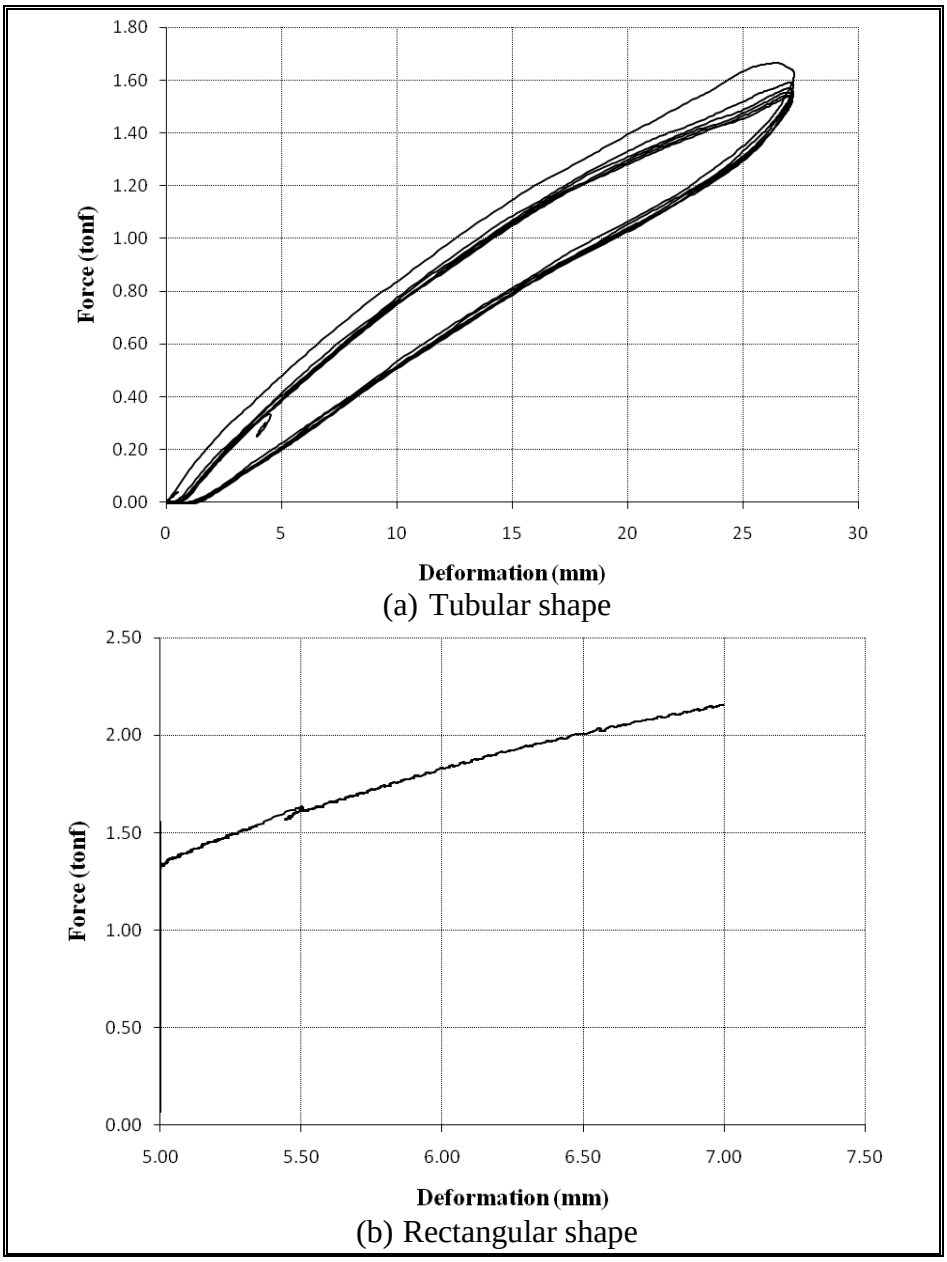

Figure 7-4: Force-deformation curves for rubber springs: (a) tubular, (b) rectangular

In order to prove the theory, the loading portions of the experimental values shown above are fitted using a polynomial curve. Figure 7-5 shows the theoretical and the experimental force-deformation curves obtained for every shape of rubber.

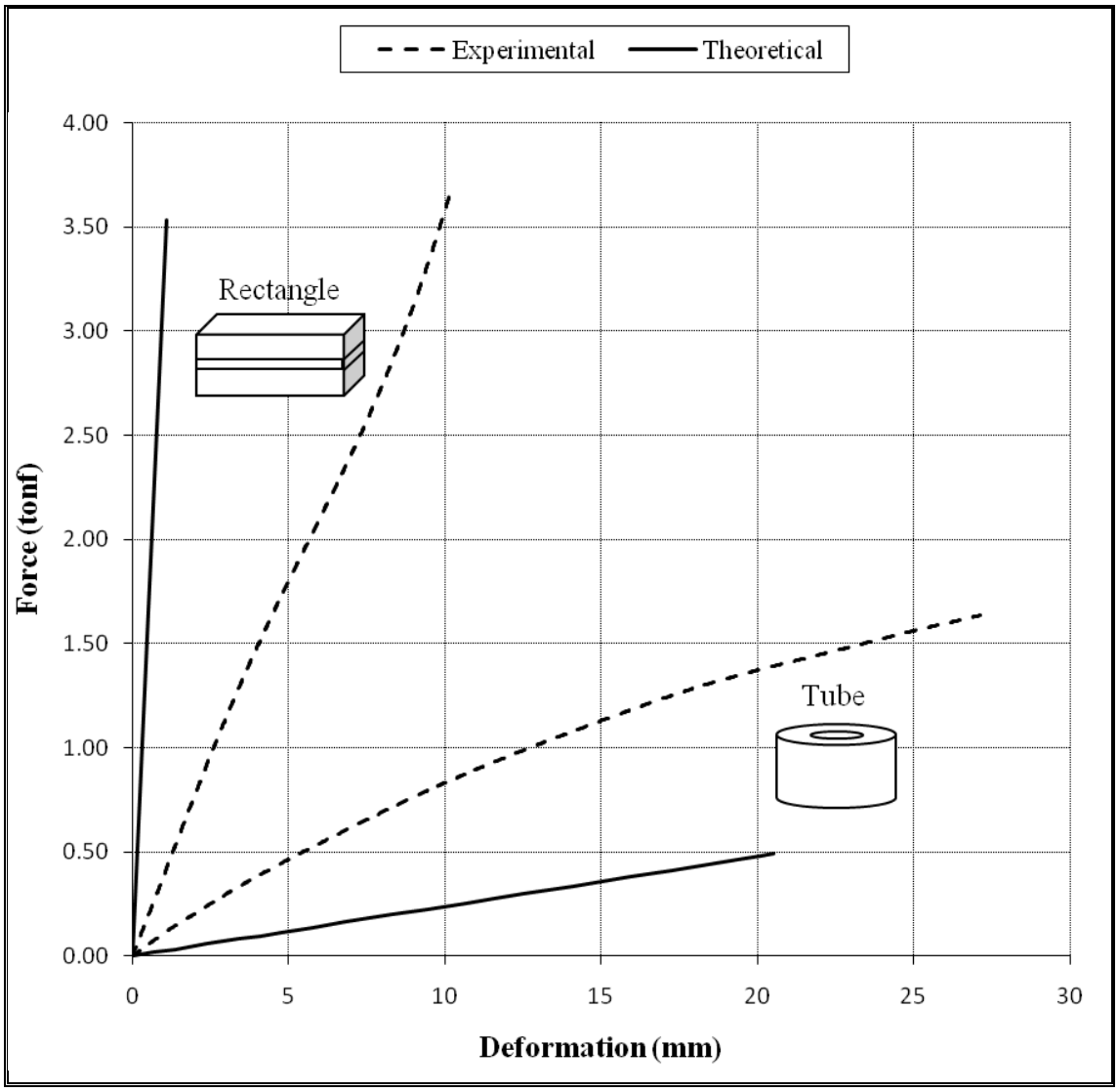

Figure 7-5: Comparison of theory with experimental values of the force-deformation curve

It is apparent that theory is not able to predict a reasonable force-deformation curve for the tested rubber springs. The tubular shaped spring has a higher stiffness than predicted and the rectangular one has a lower stiffness. A much more detailed

analysis is needed in order to predict rubber behavior. Note that the equations shown in this chapter are used to design seismic isolators where there is a lot more steel between the rubber bearings, explaining the bad fitting with the experimental results.

7.3 Finite Element Models

For a proper prediction of the force-deformation curves, finite element models are necessary. All the different shapes of the rubber springs were modeled in the finite element software ANSYS (ANSYS Inc, 2011).

In order to obtain an adequate response, rubber is modeled as a 3rd order Yeoh hyperelastic material (Boyce & Arruda, 2000). Note that the software estimates a uniaxial, a biaxial and a shear experiment for the LHDS rubber composite depending on the input values used in the 3rd order Yeoh model. Figure 7-6 shows the finite element models made. Note that only one quarter of each rubber specimen is modeled.

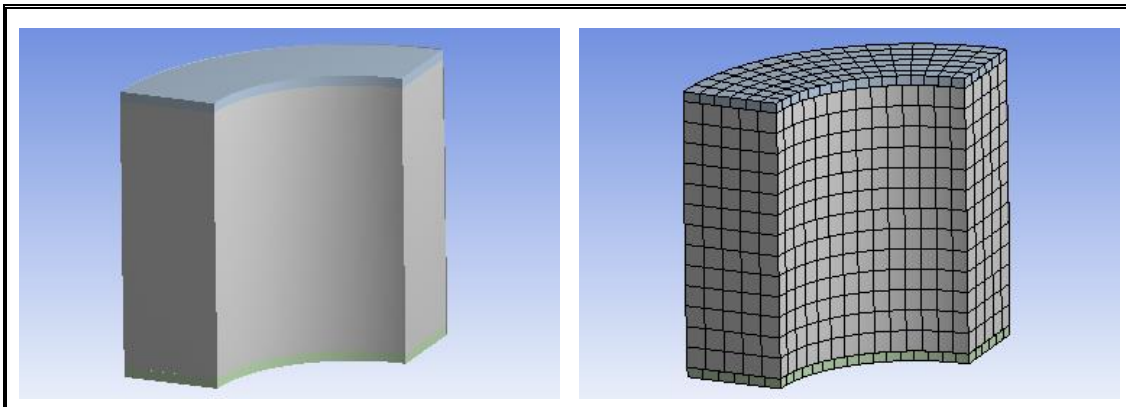

(a) Tubular model (b) Mesh

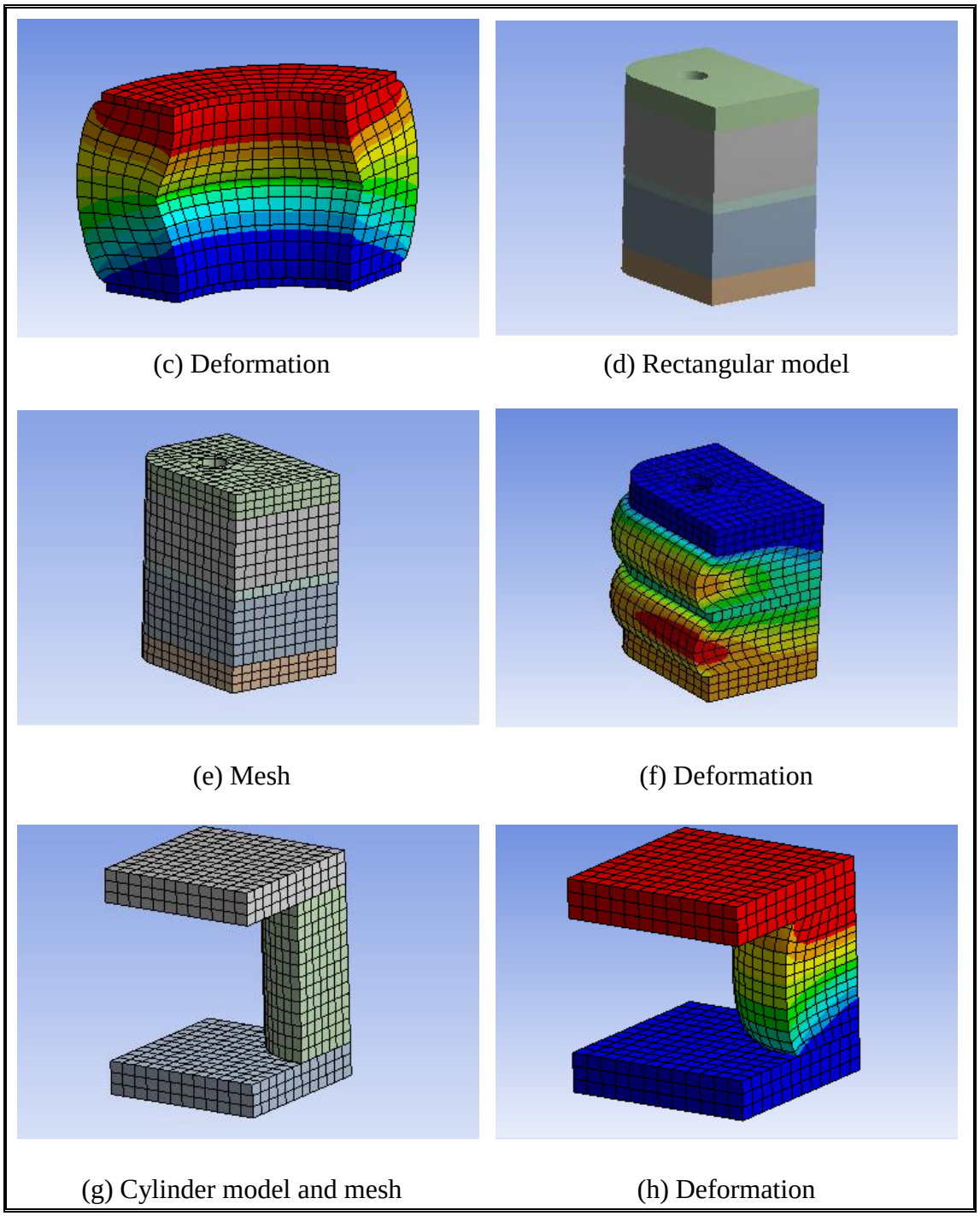

Figure 7-6: Finite element models for different shapes of rubber composite LHDS

Shown in Figure 7-7 is the comparison between the finite element models and the experimental results. Note that in this case the finite element models are very close

to reality. This takes on importance as the common seismic isolators could be modeled using this procedure. An accurate estimation of the real performance of the device would be obtained rapidly.

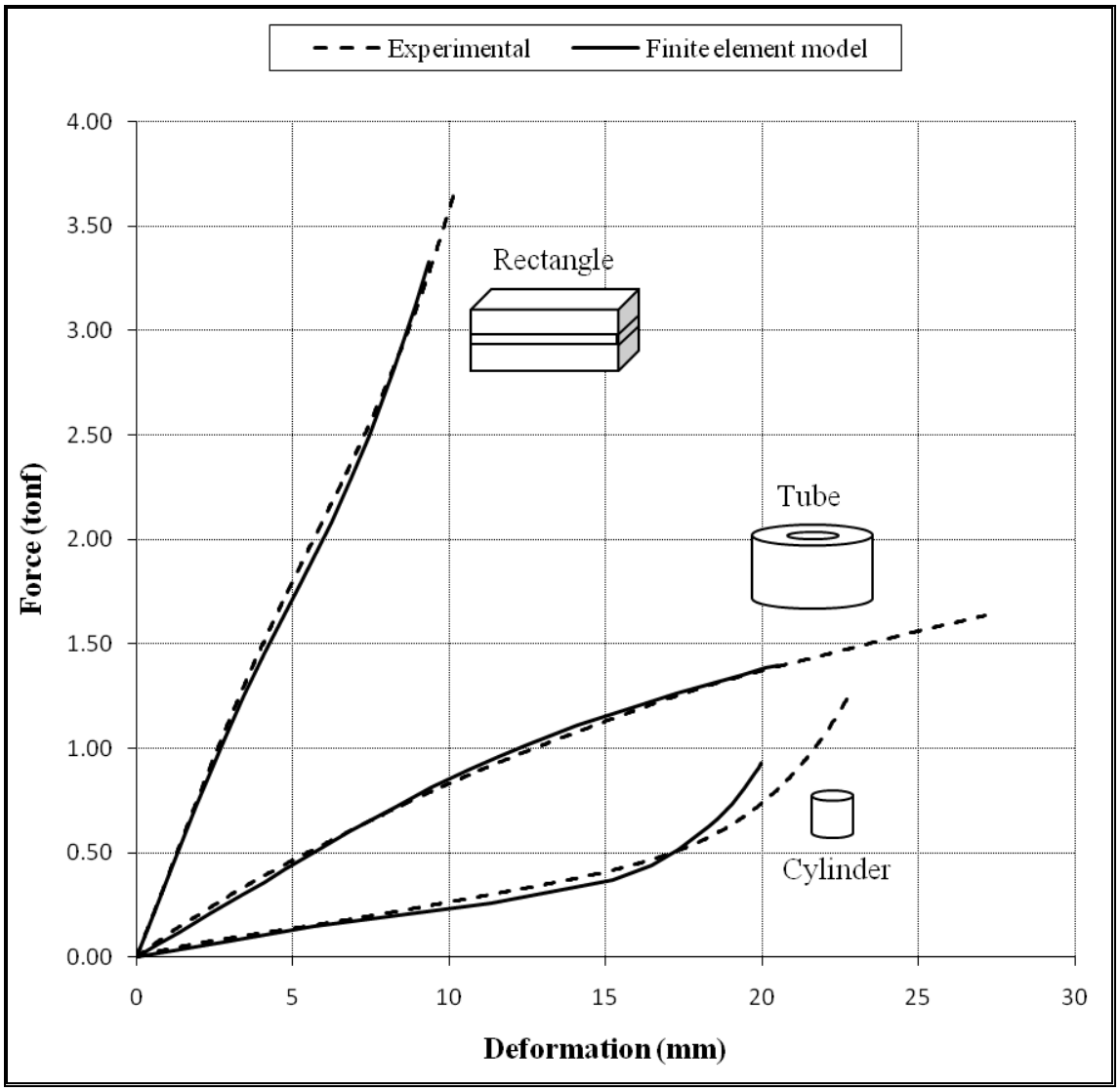

Figure 7-7: Comparison of the finite element models with the experimental values of the force-deformation curve

7.4 Behavior of the SCFD with Rubber

Since rubber has a nonlinear behavior, the final device using these elements will have a different force-deformation curve than the one shown in Chapter 2 of this research. Figure 7-8 shows a schematic hysteretic curve for a SCFD with both longitudinal and transverse rubber springs.

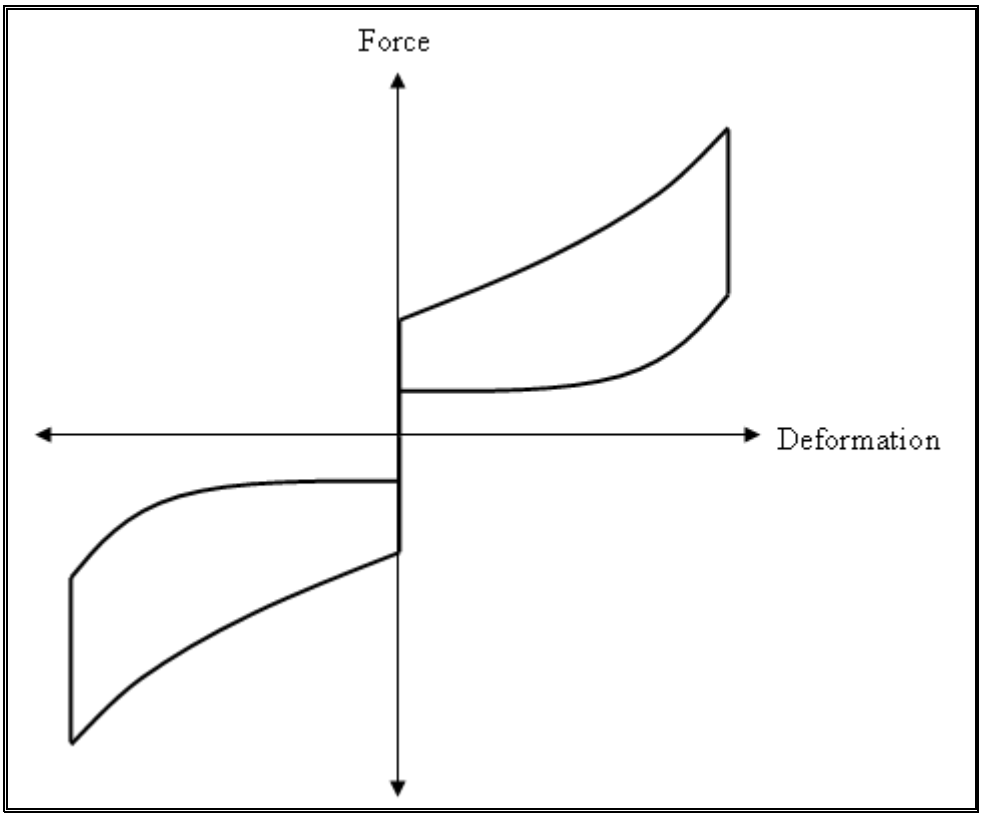

Figure 7-8: Hysteretic behavior of the SCFD with rubber springs

Caution must be taken when designing such device since the stiffness of the unloading curve will be close to zero when it reaches its initial configuration. On the other hand, if the strain of the rubber is high, the loading stiffness of the hysteretic curve will increase rapidly.

8 SPRING EXPERIMENTS

For the final prototype, compression springs were used in both elastic elements of the device: the longitudinal spring and the transverse springs. These springs were designed for a stiffness given by formula (8.1) (Wahl, 1963):

$$K = \frac{Gd^4}{8D^3 n} \tag{8.1}$$

Where K is the stiffness of the spring, G is the shear modulus, d is the wire diameter, D is the mean coil diameter and n is the number of active coils. Both springs were also designed not to exceed the maximum stress given by formula (8.2) (Timoshenko, 1956):

$$\tau_{\max} = \frac{8PD}{\pi d^3}\left(\frac{4C-1}{4C-4} + \frac{0.615}{C}\right) \tag{8.2}$$

Where τ_{max} is the maximum stress of the spring, P is the maximum load applied and C is the spring index which is the ratio of the mean coil diameter to wire diameter (D/d).
The springs were tested in simple compression to verify the final stiffness. The following sections show the results for both springs.

8.1 Longitudinal Spring

The longitudinal spring was tested for a sine wave with amplitude 4cm and frequency 0.1Hz. Figure 8-1 shows actual photographs of the longitudinal spring and the experiments performed.

Figure 8-1: Longitudinal spring testing

Figure 8-2 shows the force-deformation curve for a simple compression test. The obtained stiffness of the longitudinal spring is 0.62tonf/cm. Note that the final value of the stiffness is almost the same as the designed one.

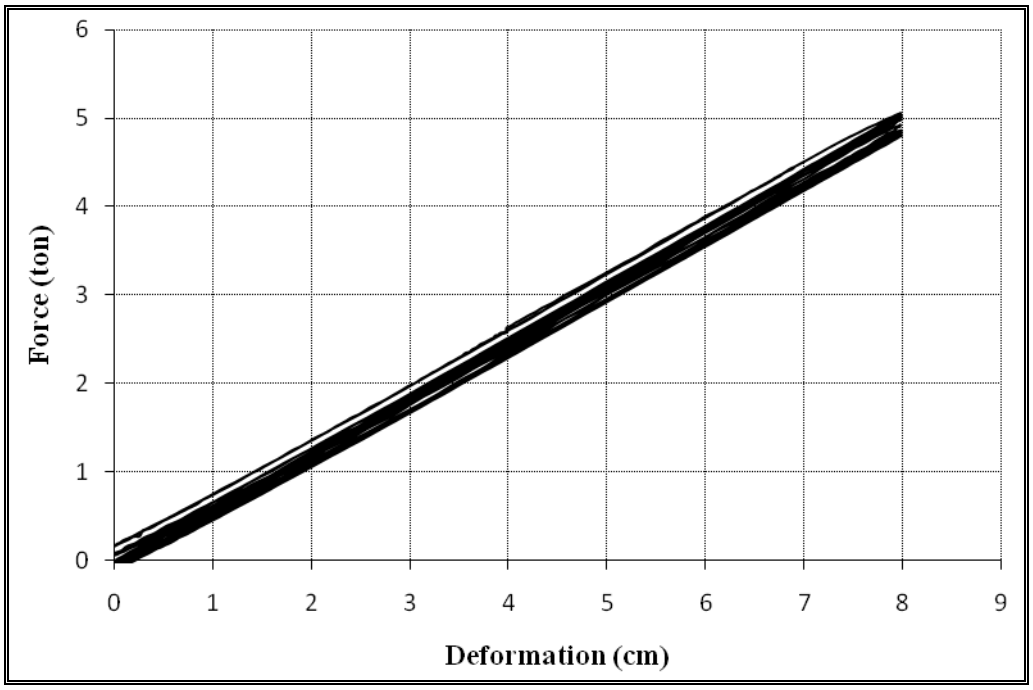

Figure 8-2: Force-deformation curve for the longitudinal spring

8.2 Transverse Spring

For the final prototype, one transverse spring consists in five compression springs in parallel. The five springs were tested in their final configuration. The input for this experiment was a sine wave with amplitude 0.2cm and frequency 0.1Hz. Figure 8-3 shows actual photographs of the transverse spring and the experiments performed.

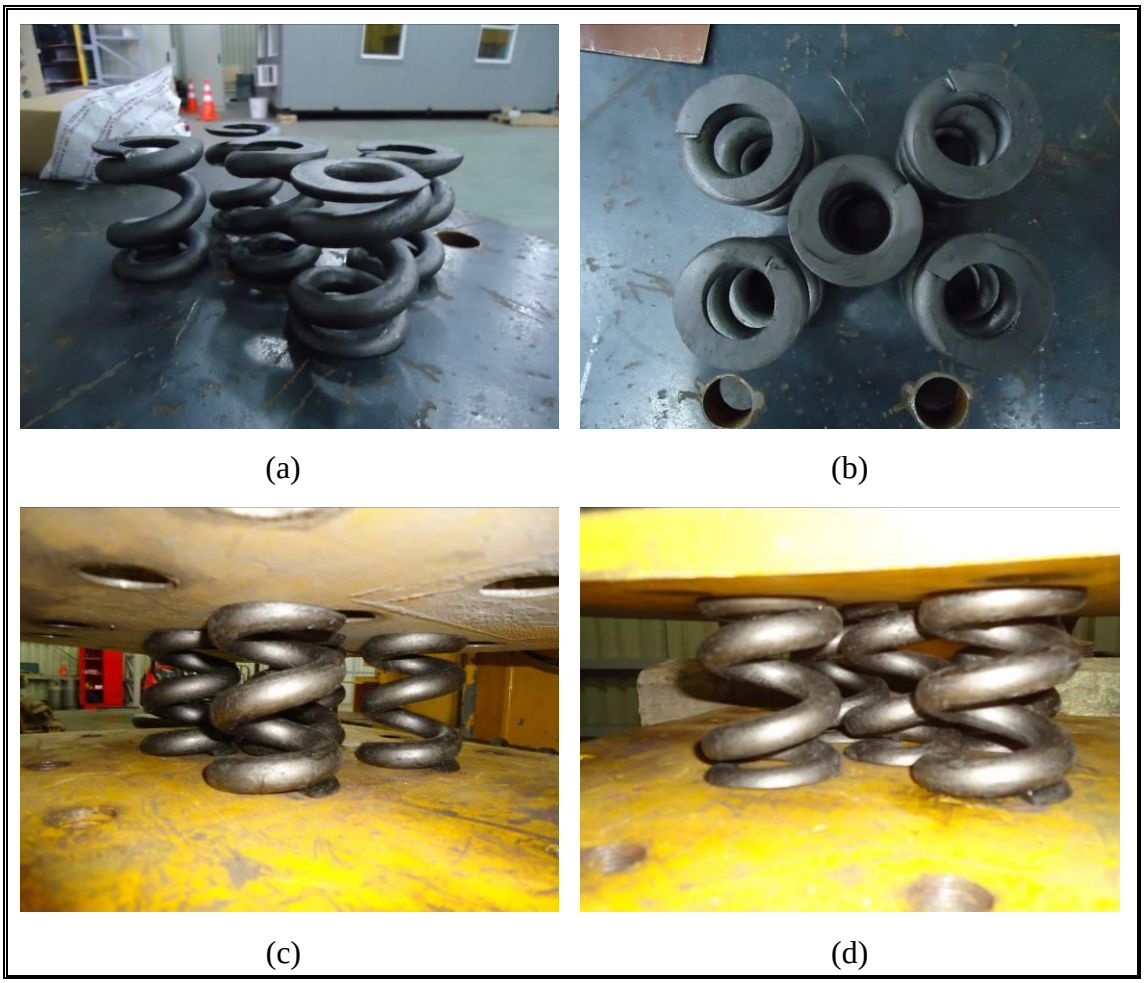

Figure 8-3: Transverse spring testing

Figure 8-4 shows the force-deformation curve for a simple compression test. The obtained stiffness of the transverse spring is 9.8tonf/cm.

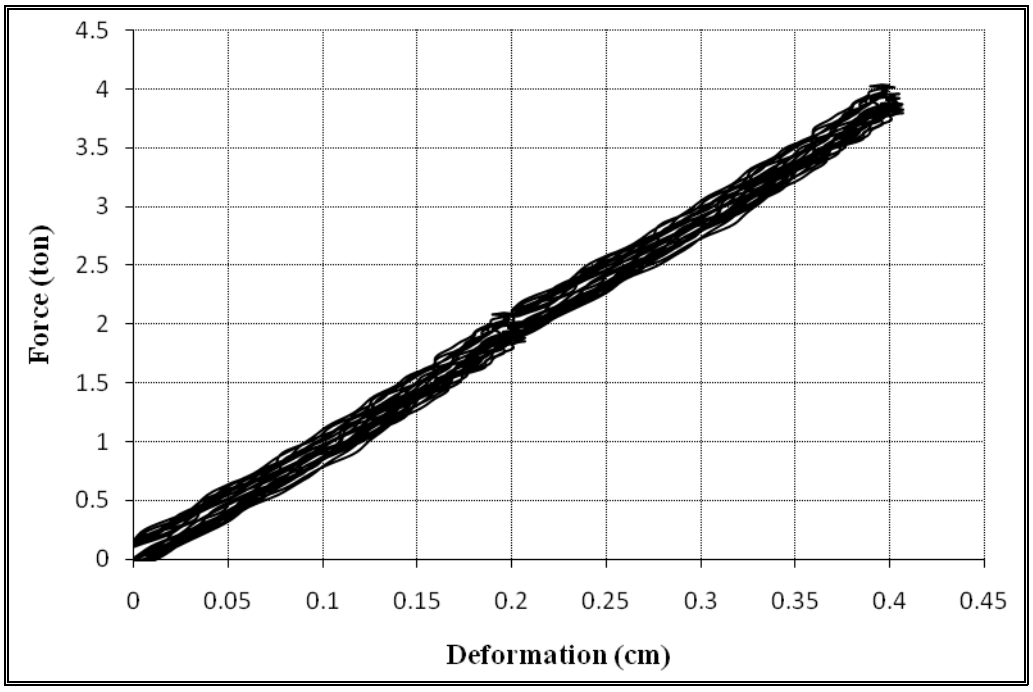

Figure 8-4: Force-deformation curve for the transverse spring

9 FINAL PROTOTYPE

The final selected design properties for the real scale SCFD are presented in Table 9-1. Note that the preliminary design of steel was made with the available literature (Shigley & Mischke, 2001). The damper has a nominal capacity of 12tonf and its design was based on the information presented herein. As expected, one of the most challenging aspects of its design and construction was to achieve a safe self-centering behavior, dissipating as much energy as possible with the available parameters involved in the design. Figure 9-1 shows a picture of the final prototype tested in laboratory.

Table 9-1: Design parameters for the SCFD prototype

Design parameter	Value
Angle of the slanted walls, α	3 [°]
Friction coefficient, μ	0.53
Longitudinal spring stiffness, K_R	0.62 [tonf/cm]
Transverse springs stiffness, K_G	9.8 [tonf/cm]
Pre-deformation of longitudinal spring, Δ_0	3.9 [cm]
Pre-deformation of transverse springs, Δ_{0G}	0.17 [cm]
Number of sliding surfaces per friction wedge, n_s	2

A set of 12 proof-of-concept harmonic tests were performed on the SCFD prototype with different amplitudes at a constant frequency of 0.1Hz. The experimental and theoretical force-deformation relationships obtained for a stroke of ±6cm are shown in Figure 9-2. It is apparent that theory matches the real behavior of the device as both experimental and theoretical curves are very similar. The simple equilibrium equations shown in chapter 2 of this thesis are sufficient to predict the behavior of the SCFD, being a huge difference with far more complicated dampers.

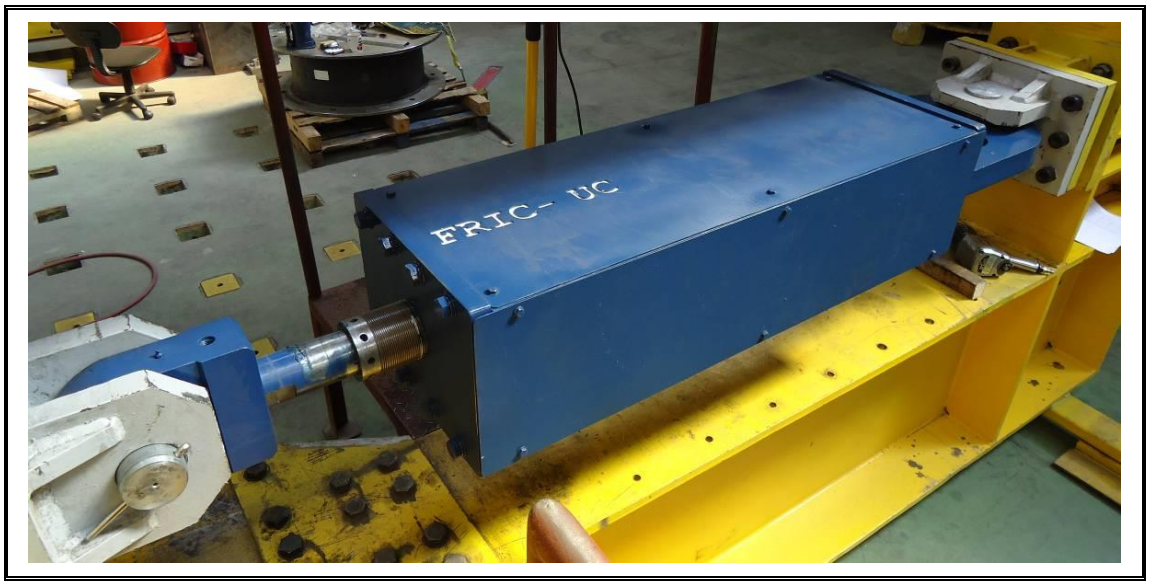

Figure 9-1: Picture of the final SCFD prototype

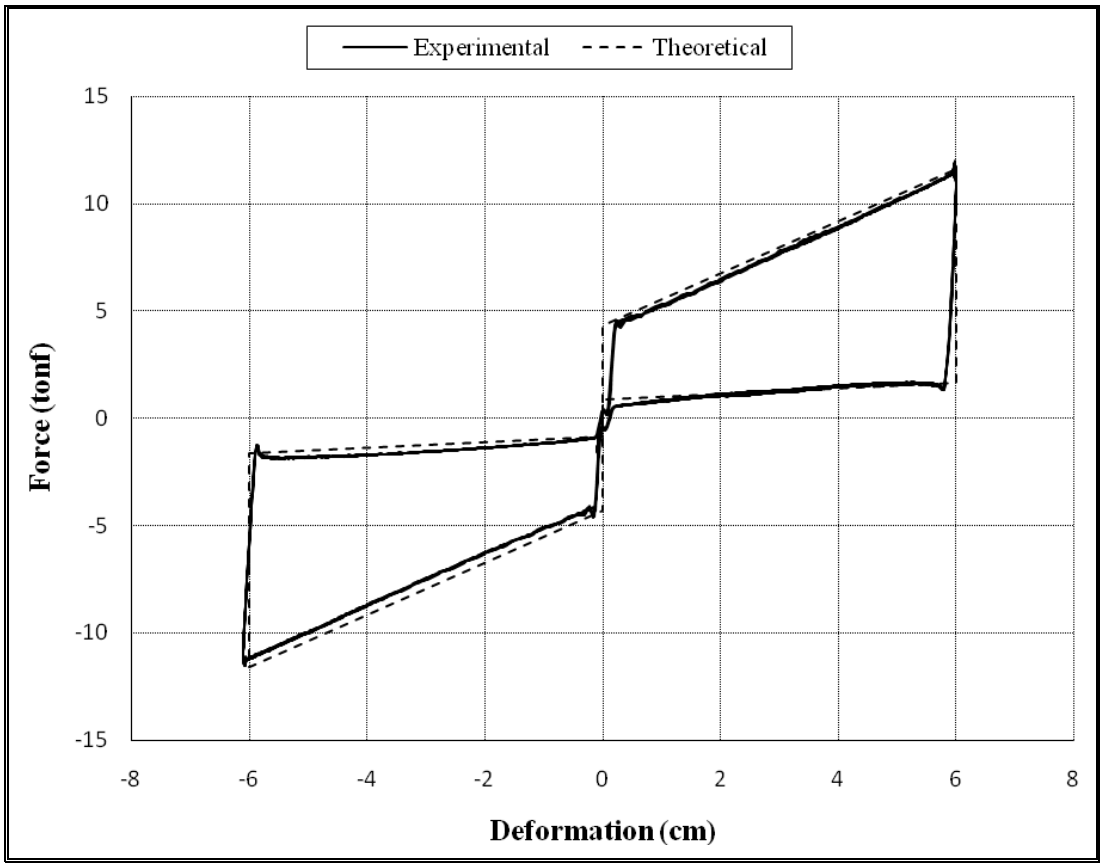

Figure 9-2: Experimental and theoretical force-deformation curves for a stroke of ±6cm

Note that the great stability shown in the test above is due to the fact that is experiment number seven and the sliding surfaces has accommodated to their final friction coefficient. Figure 9-3 shows the first six tests performed and their resulting force-deformation curves. It is very important that a final commercial device is tested in laboratory about fifty cycles in order to reach the stability shown.

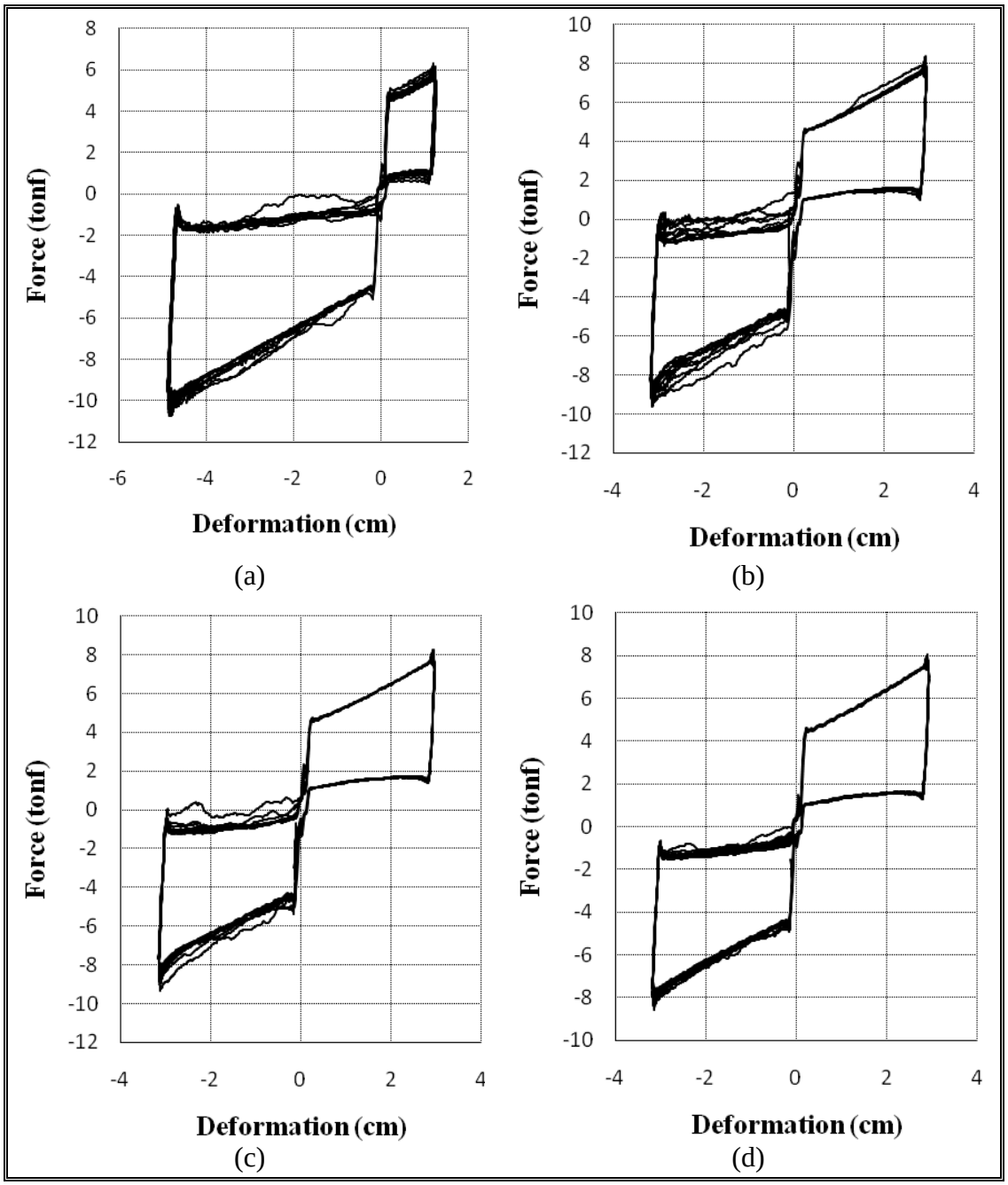

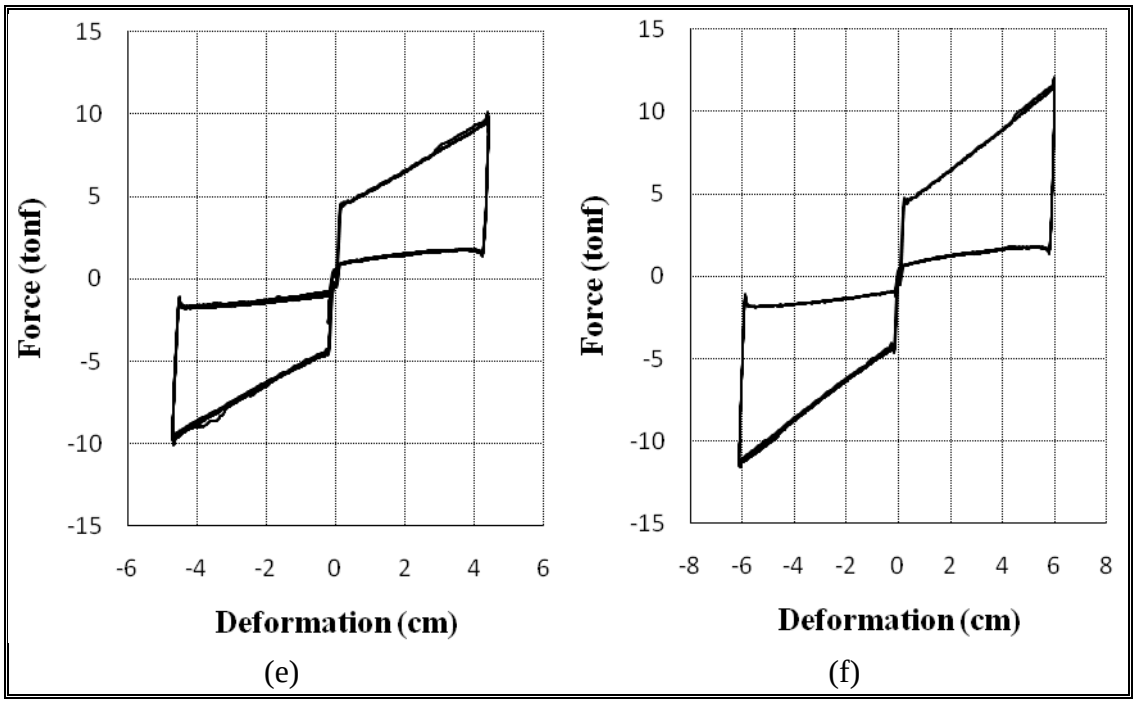

Figure 9-3: First six tests on the SCFD prototype

In addition to the initial configuration parameters shown in Table 9-1, two different variations were tested in laboratory. To achieve this, the pre-load was modified to the values shown in Table 9-2, leaving the other parameters constant.

Table 9-2: Pre-load values for additional tests

Design parameter	Original value	Variation N° 1	Variation N° 2
Pre-deformation of longitudinal spring, Δ_0	3.9 [cm]	4.9 [cm]	5.9
Pre-deformation of transverse springs in wedge number 1, Δ_{0G1}	0.17 [cm]	0.22 [cm]	0.22 [cm]
Pre-deformation of transverse springs in wedge number 2, Δ_{0G2}	0.17 [cm]	0.17 [cm]	0.22 [cm]

Experimental and theoretical results for variation number one are shown in Figure 9-4, while for variation number two are shown in Figure 9-5.

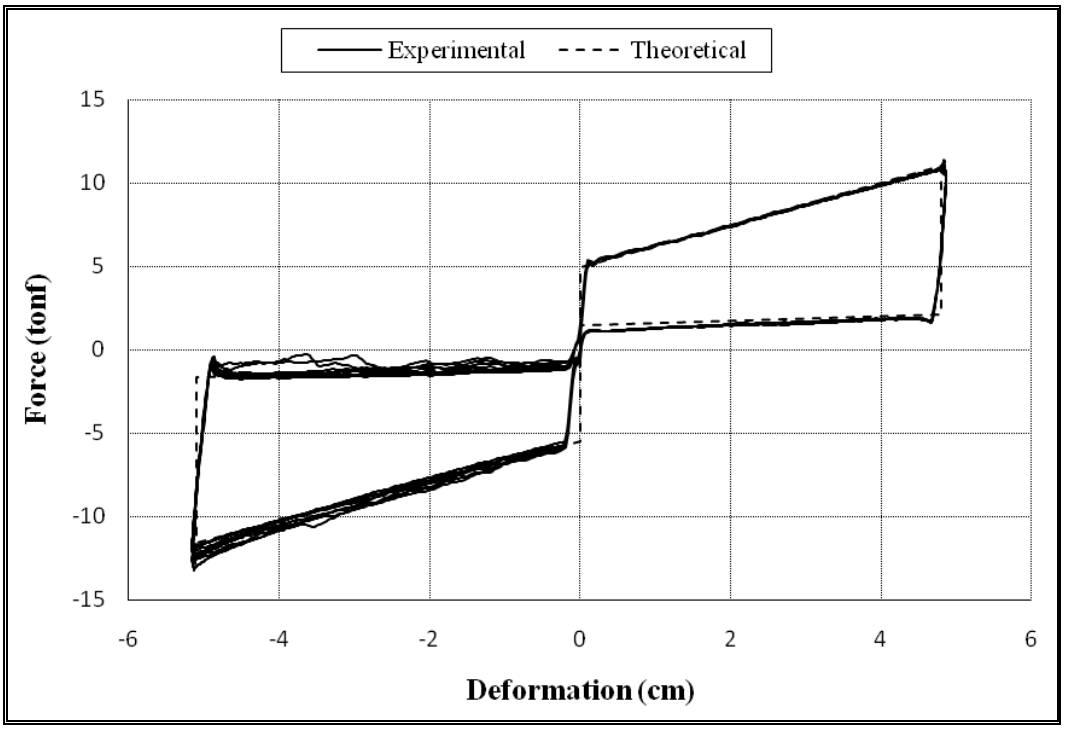

Figure 9-4: Experimental and theoretical force-deformation curves for variation N°1

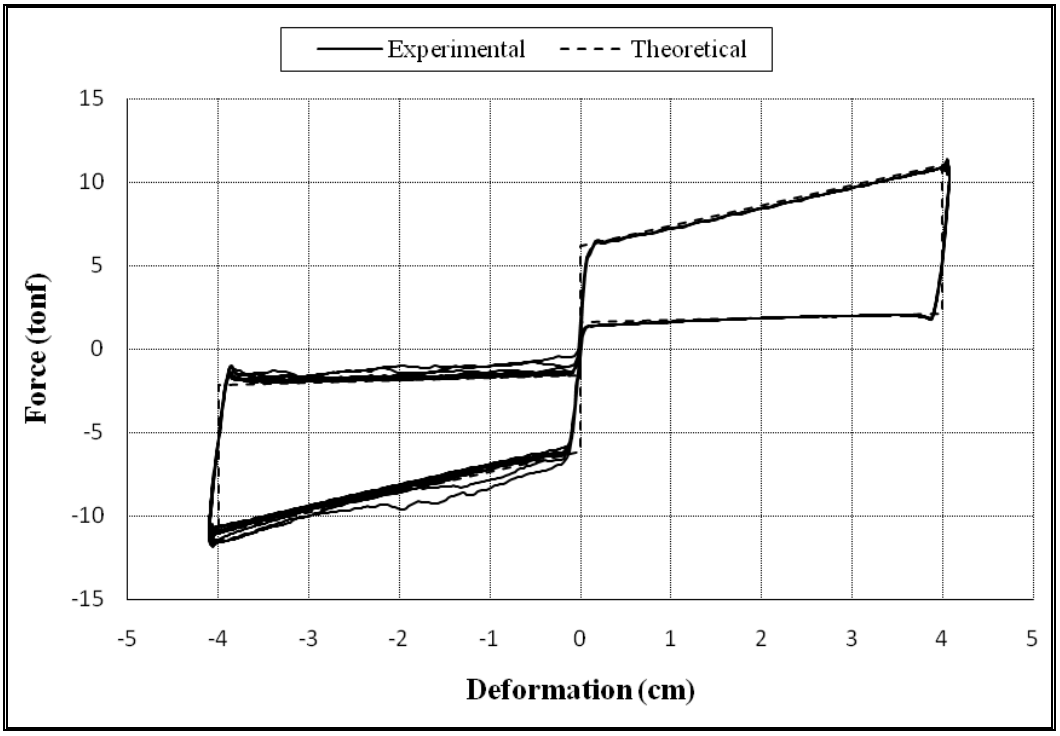

Figure 9-5: Experimental and theoretical force-deformation curves for variation N°2

Note that even changing the initial parameters, the hysteretic curve can be estimated accurately. For every test made to the SCFD prototype see Appendix A. Note that temperature was not an issue as it varies between 12°C and 15°C in every experiment.

Although a 15tonf damper was successfully tested, dampers with higher capacities (from 50tonf to 100tonf) can be designed using appropriate values for the parameters involved in the SCFD behavior.

10 CONCLUSIONS

This thesis proposes and studies a new energy dissipation device: the Self-Centering Frictional Damper. It has been shown that the SCFD provides several hysteretic behaviors, such as: triangular, flag-shaped and rectangular configurations. This device has a very convenient mechanical behavior since it can be self-centering (it returns to its original position once the loading has finished), the resistance of the damper is increased as the deformation increases and the resulting hysteretic curve is very stable. Note that all of the theory presented herein is based with experimental laboratory tests.

One of the biggest advantages of the SCFD in relation with other energy dissipation devices is that the real behavior of the device can be predicted accurately using simple equilibrium equations. The latter comes from the mechanical elements in the final device, which have a well known and studied behavior. These equations were tested successfully with the experimental data of a 12tonf large-scale damper.

As this device is available in very different configurations, it is appropriate to use it in buildings that need high capacity dampers or in specific applications such as nuclear power stations. The use of the SCFD is recommended also to raise damping in truss structures.

It was possible to predict the behavior of rubber in simple compression tests using finite element models. This takes on importance as the equations used in the design of seismic isolators are not capable to predict what would happen if there is a considerable amount of rubber. Important seismic isolators or any rubber element can be designed using these finite element models in order to predict its behavior accurately.

To fully understand the proposed device, further investigation is required. It is necessary to analyze structures with the SCFD included (Bhaskararao & Jangid, 2006), its linearization for preliminary design purposes and the testing of even larger-scale dampers. Another path of research should be conducted in the distribution of the SCFD

within each structure for optimal energy dissipation, structures with SCFD subjected to strong ground shaking and the possible application of this device in tune mass dampers. Since there are many different energy dissipating devices and each structure is unique, the advantages and disadvantages of using a particular type of device should be studied in each case.

REFERENCES

Aiken, I.D. (1996). Passive Energy Dissipation – Hardware and Applications. En I. Aiken (Ed), *Los Angeles County and SEAOSC Symposium on passive energy dissipation systems for new and existing buildings*. Los Angeles, USA: SEAOC.

Aiken, I.D., Nims, D.K., Whittaker, A.S. & Kelly, J.M. (1993). Testing of passive energy dissipation systems. *Earthquake Spectra*, 9(3), 335-370.

ANSYS, Inc (2011). ANSYS (11). Pittsburgh, Pennsylvania, USA.

Bhaskararao, A.V. & Jangid, R.S. (2006). Seismic analysis of structures connected with friction dampers. *Engineering Structures*, 28(5), 690-703.

Boyce, M.C., Arruda E.M. (2000). Constitutive Models in Rubber Elasticity: A Review. *Rubber Chemistry and Technology*, 73(3), 504-523.

Christopoulos, C. (2004). Frequency Response of flag-shaped single degree of freedom hysteretic systems. *Journal of Engineering Mechanics*, 130(8), 894-903.

Inaudi, J.A., Nims, D.K. & Kelly, J.M. (1993). *On the analysis of structures with energy dissipating restraints* (Report No. UCB/EERC-93/13). Earthquake Engineering Research Center, University of California at Berkeley.

Naeim, F. & Kelly, J.M. (1999). *Design of Seismic Isolated Structures*. New York, USA: John Wiley & Sons, Inc.

Nims, D.K, Richter, P.J. & Bachmann, R.E. (1993). The use of the Energy Dissipating Restraint for Seismic Hazard Mitigation. *Earthquake Spectra*, 9(3), 467-489.

Rabinowicz, E. (1995). *Friction and Wear of Materials*. (2nd edition) New York, USA: John Wiley & Sons, Inc.

Savaskan, T., & Bican, O. (2010). Dry sliding friction and wear properties of Al-25Zn-3Cu-Si alloy. *Tribology International*, 43(8), 1346-1352.

Shigley, J.E. & Mischke, C.R. (2001). *Mechanical Engineering Design*. (6th edition) New York, USA: McGraw-Hill Book Company.

Singh, J.B., Cai, W. & Bellon, P. (2007). Dry sliding of Cu-15 wt% Ni-8 wt% Sn bronze: Wear behavior and microstructures. *Wear*, 263(6), 830-841.

Timoshenko, S.P. (1956). *Strength of Materials, Part I, Elementary Theory and Problems*. (3rd edition) New York, USA: D. Van Nostrand Company.

Wahl, A.M. (1963). *Mechanical Springs*. (2nd edition) New York, USA: McGraw-Hill Book Company.

Westenenk, B. & de la Llera, J. C. (2011). Self-Centering Frictional Damper. *Engineering Structures* (To be published).

Xing, H.L. & Makinouchi, A. (2002). Finite Element Analysis of a Sandwich Friction Experiment Model of Rocks. *Pure and Applied Geophysics*, 159(9), 1985-2009.

Zoltan, N., Karoly V., Laszlo, M. & Klaus, F. (1999). Numerical and Finite Element Contact Temperature Analysis of Steel-Bronze Real Surfaces in Dry Sliding Contact. *Tribology Transactions*, 42(3), 453-462.

A P P E N D I C E S

APPENDIX A: PROTOTYPE EXPERIMENTS

As mentioned earlier, this Appendix shows all tests done to the SCFD real-scale damper. Table A-1 shows the details of every experiment. Note that all tests were done with a sine wave input at constant frequency of 0.1Hz.

Table A-1: Details of every experiment performed to the SCFD prototype

ID	Amplitude [mm]	Maximum Displacement [mm]	Minimum Displacement [mm]	N° of cycles	Configuration
1	30	12	-48	10	Original
2	30	30	-30	10	Original
3	30	30	-30	10	Original
4	30	30	-30	30	Original
5	45	45	-45	30	Original
6	60	60	-60	10	Original
7	60	60	-60	30	Original
8	35	25	-45	10	Variation N°1
9	35	35	-35	10	Variation N°1
10	50	50	-50	10	Variation N°1
11	35	35	-35	10	Variation N°2
12	40	40	-40	10	Variation N°2

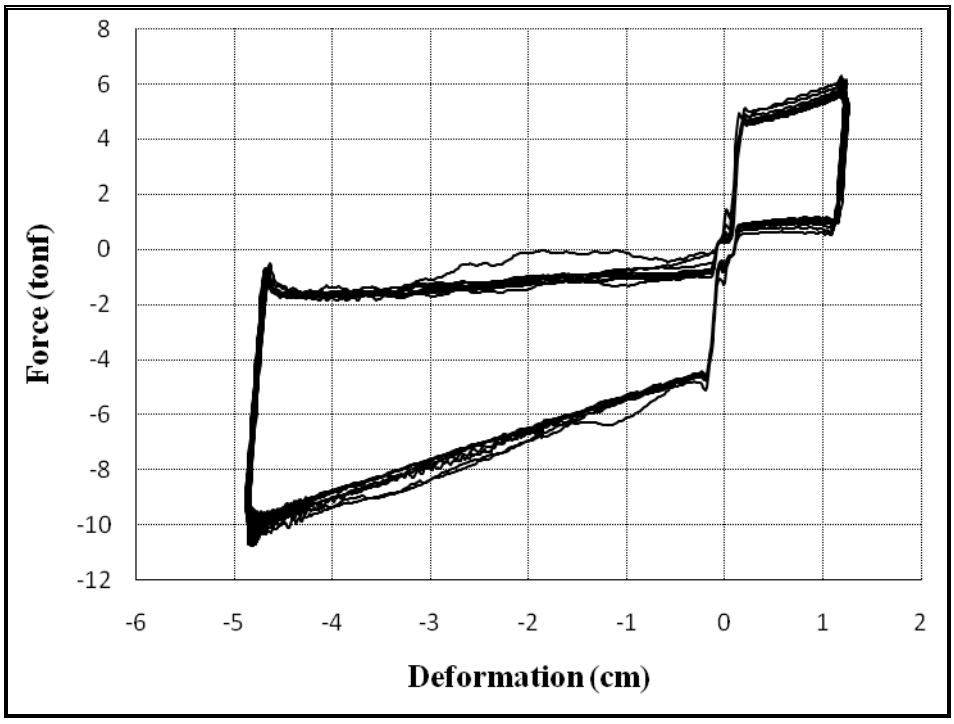

Figure A-1: Experiment number 1

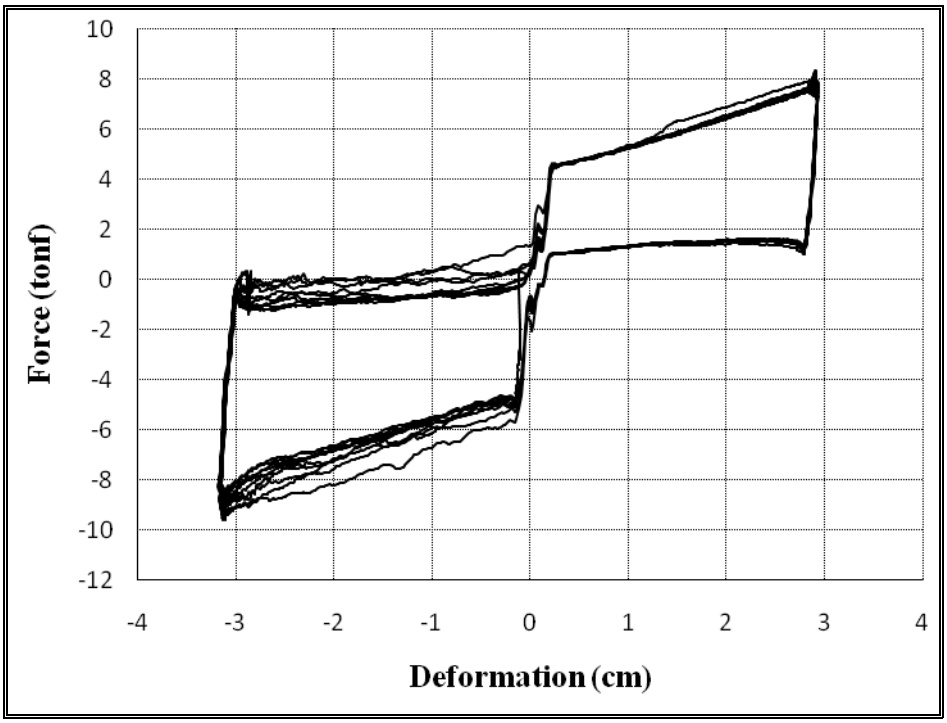

Figure A-2: Experiment number 2

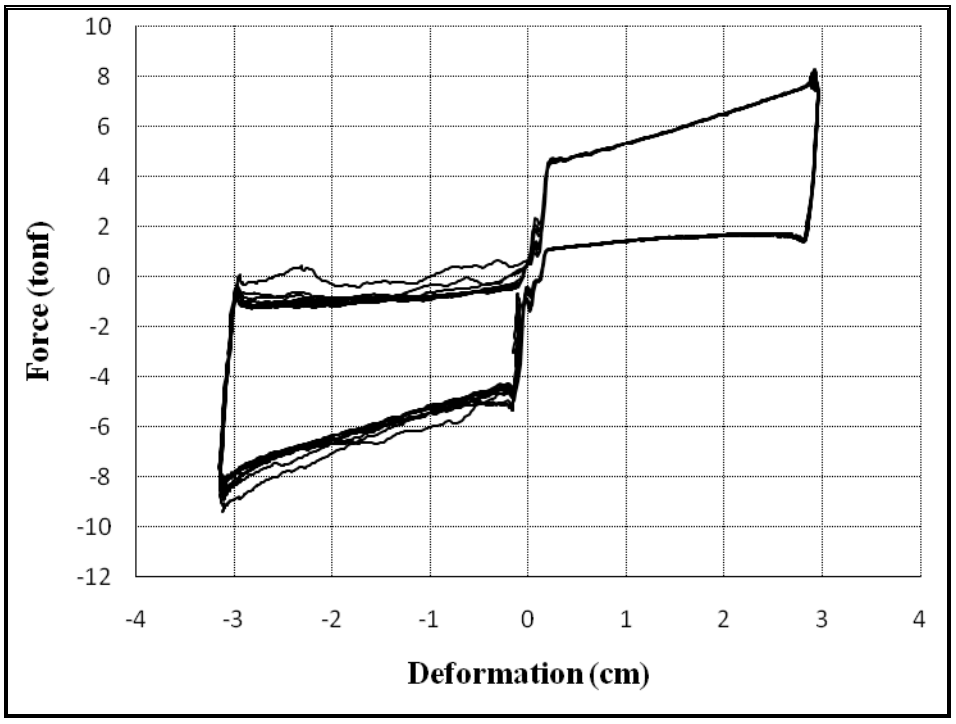

Figure A-3: Experiment number 3

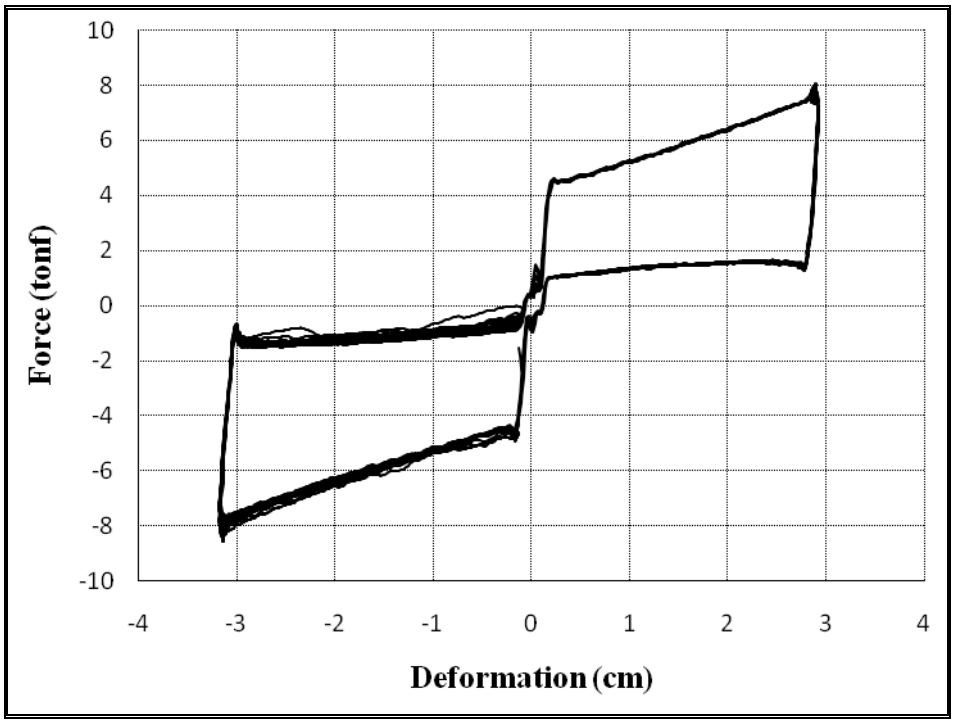

Figure A-4: Experiment number 4

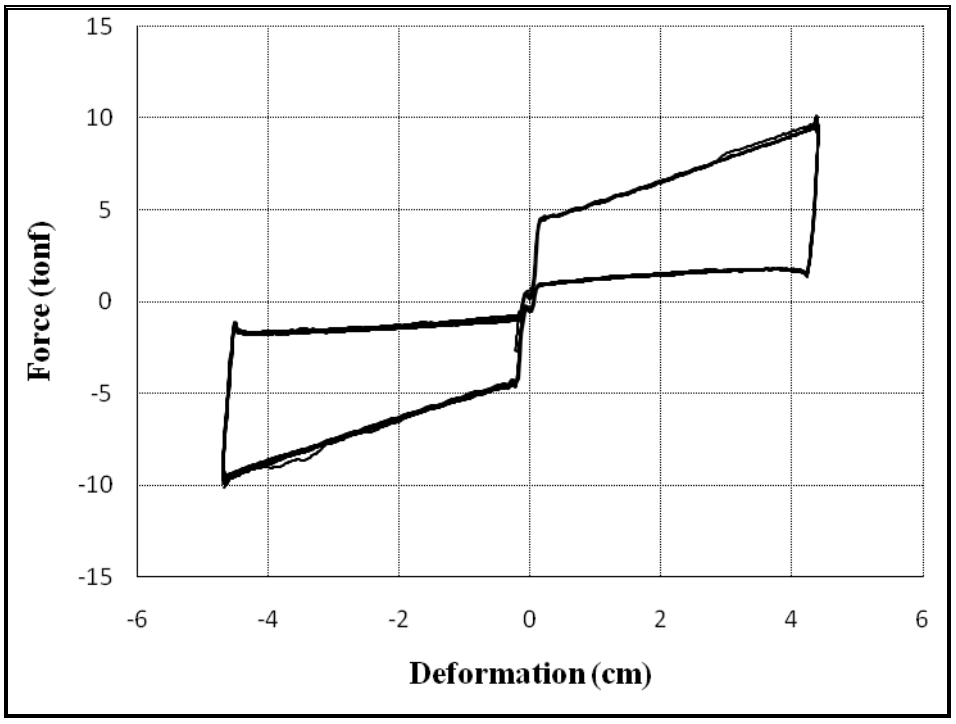

Figure A-5: Experiment number 5

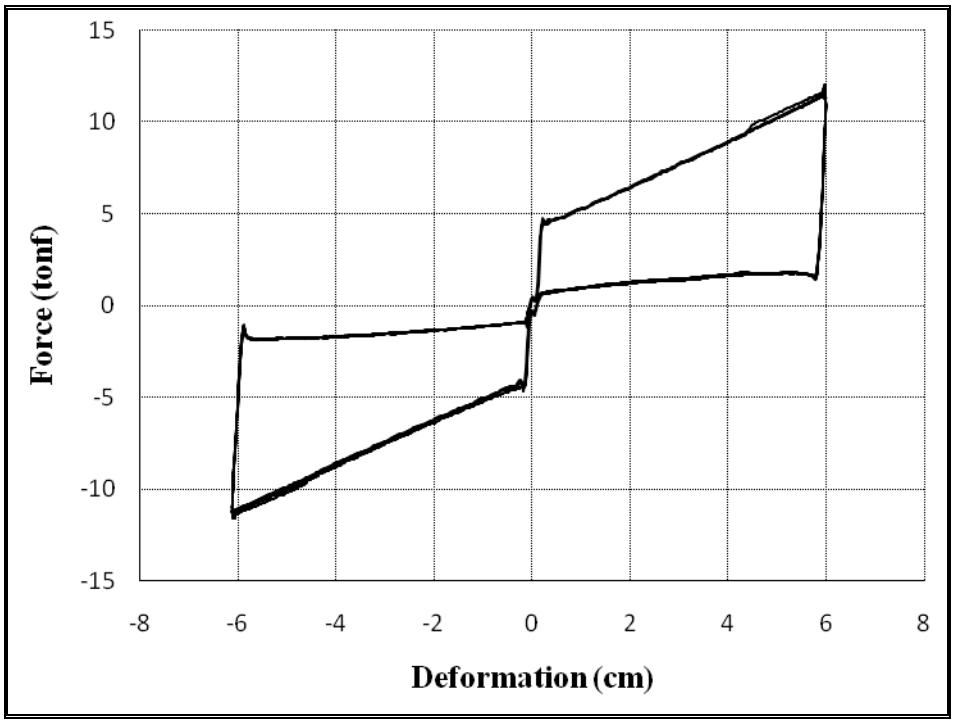

Figure A-6: Experiment number 6

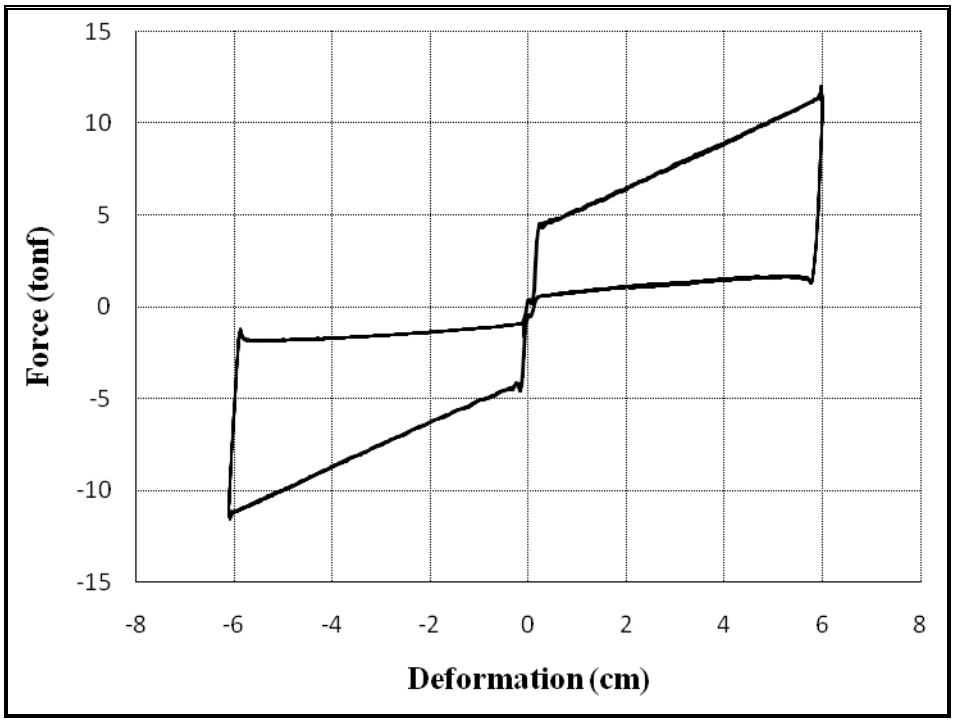

Figure A-7: Experiment number 7

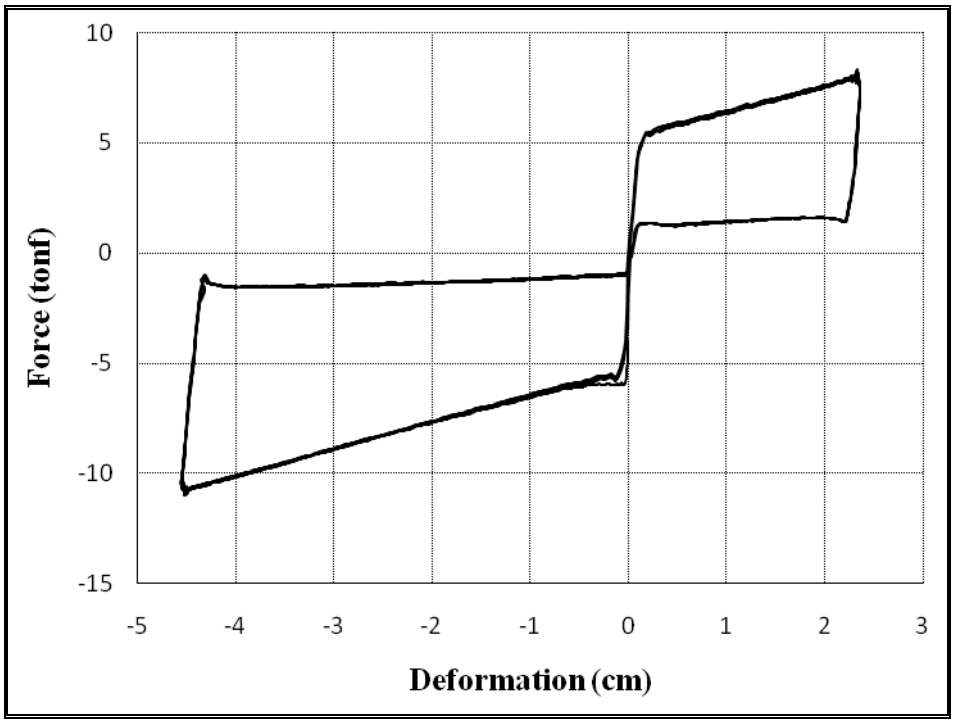

Figure A-8: Experiment number 8

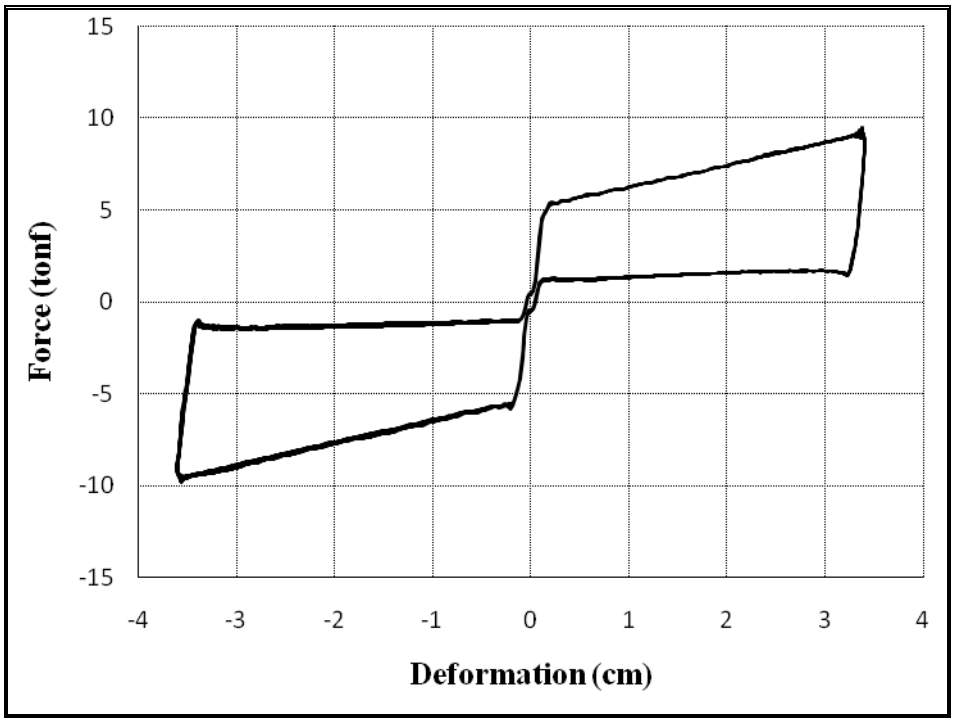

Figure A-9: Experiment number 9

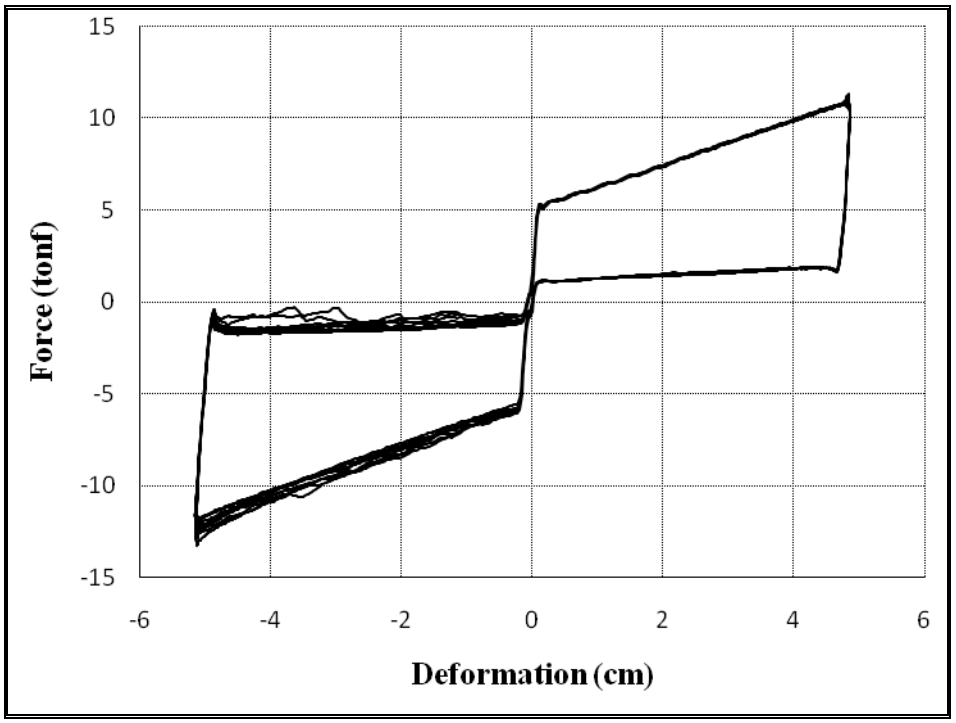

Figure A-10: Experiment number 10

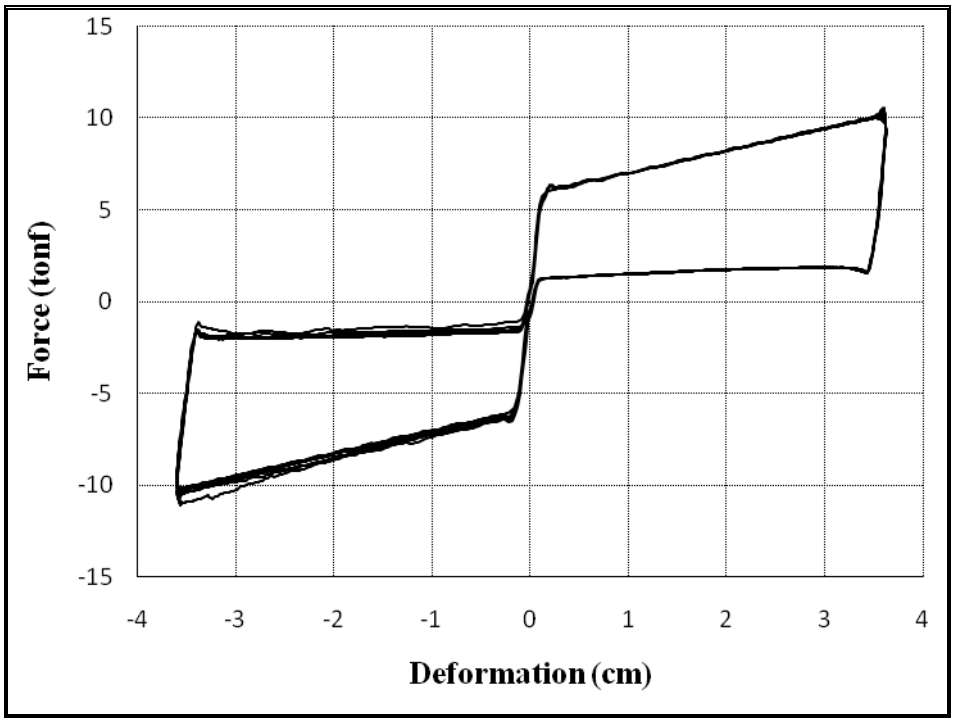

Figure A-11: Experiment number 11

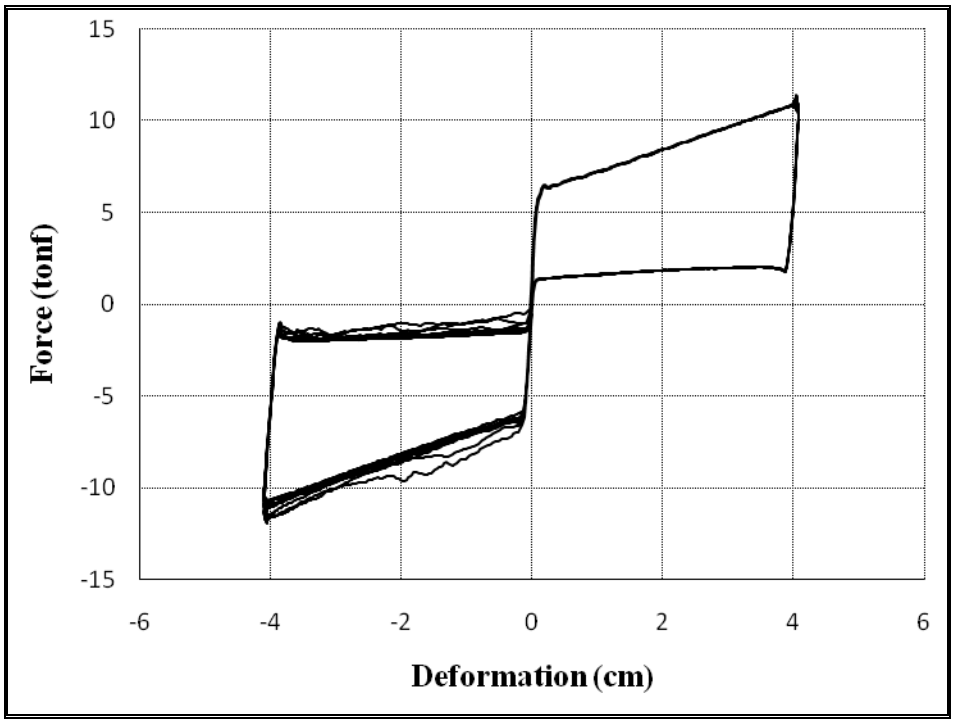

Figure A-12: Experiment number 12